5-8-2020

RESISTIVE SWITCHING CHARACTERISTICS OF NANOSTRUCTURED AND SOLUTION-PROCESSED COMPLEX OXIDE ASSEMBLIES

Zimu Zhou
University of Massachusetts Amherst

RESISTIVE SWITCHING CHARACTERISTICS OF NANOSTRUCTURED AND SOLUTION-PROCESSED COMPLEX OXIDE ASSEMBLIES

A Dissertation Presented

by

ZIMU ZHOU

Submitted to the Graduate School of the
University of Massachusetts Amherst in partial fulfillment
of the requirements for the degree of

DOCTOR OF PHILOSOPHY

MAY 2020

Mechanical and Industrial Engineering

RESISTIVE SWITCHING CHARACTERISTICS OF NANOSTRUCTURED AND SOLUTION-PROCESSED COMPLEX OXIDE ASSEMBLIES

A Dissertation Presented

by

Zimu Zhou

Approved as to style and content by:

_____
Stephen S. Nonnenmann, Chair

_____
Yubing Sun, Member

_____
Ashwin Ramasubramaniam, Member

_____
Jessica Schiffman, Member

_____
Sundar Krishnamurty, Department Head
Mechanical and Industrial Engineering

DEDICATION

To my family

ACKNOWLEDGMENTS

My deepest gratitude must be given to my advisor Prof. Stephen Nonnenmann, who has been encouraging, thoughtful and patient throughout my studies. The discussions we had during my time were invaluable to my research and my own development. I would also like to thank my committee members, Prof. Ashwin Ramasubramaniam, Prof. Yubing Sun and Prof. Jessica Schiffman for the encouragement, suggestions and ideas to my dissertation and presentation.

I want to thank my former lab mates, Dr. Jiaying Wang, for the time and efforts preparing my samples. Dr. Jiaxin Zhu, who taught me so many experiments in the early days. I would also thank Jacob Davis, Selena Cho, Serzat Safaltin and Jieun Park. All of you were great source of support and friendship.

I would also like to thank my collaborators. Prof. Jonathan De Roo and Pedro Dominguez for prepared and characterized many samples in my projects. Prof. Alfred Crosby was especially generous in allowing the use of his laboratory instrument. Prof. Kevin Kittilstved, Muhammad Abdullah, Xiangxi Meng and Nick Hight-Huf provided in-depth data analysis to my research. I would also thank Dr. Alexander Ribbe for all the support in UMass AFM facilities. I also appreciate Dr. Uzodinma Okoroanyanwu, Tim Walsh and Drew Griffin for the support and insights during my job search.

Special thanks to my rock climbing partners Rachel Aronow, Cristian Rodriguez, Kim Du, Marcia Rojas, Sam Bill, David Meier and Dylan Barber. Thanks for helping me to get through my research projects and bouldering projects.

In the last, I thank my parents, my grandparents, my aunt family and my girlfriend, for all the support during my six-year Ph.D. study. Their love keeps me alive here 7386.66 miles away from home.

ABSTRACT

RESISTIVE SWITCHING CHARACTERISTICS OF NANOSTRUCTURED AND SOLUTION-PROCESSED COMPLEX OXIDE ASSEMBLIES

MAY 2020

ZIMU ZHOU

B.S., SHANGHAI DIANJI UNIVERSITY

Ph.D., UNIVERSITY OF MASSACHUSETTS AMHERST

Advisor: Professor Stephen S. Nonnenmann

Miniaturization of conventional nonvolatile (NVM) memory devices is rapidly approaching the physical limitations of the constituent materials. An emerging random access memory (RAM), nanoscale resistive RAM (RRAM), has the potential to replace conventional nonvolatile memory and could foster novel type of computing due to its fast switching speed, high scalability, and low power consumption. RRAM, or memristors, represent a class of two terminal devices comprising an insulating layer, such as a metal oxide, sandwiched between two terminal electrodes that exhibits two or more distinct resistance states that depend on the history of the applied bias. While the sudden resistance reduction into a conductive state in metal oxide insulators has been known for almost 50 years, the fundamental resistive switching mechanism is a complex phenomenon that is still long-debated, complex process. Further improvements to existing memristor performance require a complete understanding of memristive properties under various operation conditions. Additional technical issues also remain, such as the

development of facile, low-cost fabrication methods as an alternative to expensive, ultra-high vacuum (UHV) deposition methods.

This collection of work explores resistive switching within metal oxide-based memristive material assemblies by analyzing the fundamental physical insulating material properties. Chapter 3 aims to translate the utility and simplicity of the highly ordered anodic aluminum oxide (AAO) template structure to complex, yet more functional (memristive) materials. Functional oxides possessing ordered, scalable nanoporous arrays and nanocapacitor arrays over a large area is of interest to both the fields of next-generation electronics and energy storing/harvesting devices. Here their switching performance will be evaluated using conductive atomic force microscopy (C-AFM). Chapter 4 demonstrates a convective self-assembly fabrication method that effectively enables the synthesis of a low-cost solution processed memristor comprising binary oxide and perovskite ABO3 nanocrystals of varying diameter. Chapter 5 systematically compares the influence of inter-nanoparticle distance on the threshold switching SET voltage of hafnium oxide (HfO_2) memristors. Utilizing shorter phosphonic acid ligands with higher binding affinity on the nanocrystal surface enabled a record-low SET voltage to be achieved. Chapter 6 extends the scope to the fine tuning of solution processed memristors with two types of perovskites nanocrystals. The primary advantage of nanocrystal memristors is the ability to draw from additional degrees of freedom by tuning the constituent nanocrystal material properties. Recent advancement of solution phase techniques enables a high degree of controllability over the nanocrystal size and structure. Thus, this

work found in this dissertation aims to understand and decouple the effects of the geometric size and substitutional nanocrystal parameters on resistive switching.

TABLE OF CONTENTS

Page

LIST OF TABLES

LIST OF FIGURES

Figure Page

CHAPTER 1

INTRODUCTION AND BACKGROUND

1.1 Motivation and Background

In 1959, Richard Feynman gave the famous lecture " There's Plenty of Room at the Bottom: An Invitation to Enter a New Field of Physics" at the annual meeting of American Physical Society (APS).[1] He proposed manipulating and controlling matter "on a small scale" – atomic scale. Although the talk did not draw too much attention in 1960s and 1970s, researchers considered its significance in catalyzing the development of nanotechnology as a nascent field in 1980s and 1990s. As we are approaching the physical limit of Moore's Law,[2] emerging memories show great promise on next-generation non-volatile memory (NVM) devices.

Modern computer and portable electronic device processing capability is heavily reliant on memories. The well-known computer memory hierarchy is mainly comprising of three memory components: cache, main memory and storage memory.[3] For over three decades, the mainstream memory technologies are flash, dynamic random-access memory (DRAM) and static random-access memory (SRAM).[4] The working principles behind these memory technologies are all based on charge storage mechanism. With the rapid development of high-density and low-power-consumption memories, conventional charge-storage memory technologies quickly approach the limit of device miniaturization, when device lateral size shrinks down to 10 nm and below

because of the difficulty of retaining enough electrons in one single cell.[5] The inevitable leaking of electric charge will result in performance degradation and system reliability. In this context, intense researches have been focusing on emerging memories with low operating voltage (<1 V), long retention time (>10 years), fast read/write speed (< ns) and most importantly, exceptional scalability (<10 nm).[6]

Fortunately, there are many materials that exhibit robust hysteresis response to external electrical stimulation such as resistance, polarization and magnetization. Several types of emerging memories based on different working principles have been proposed to address this bottleneck. Examples are ferroelectric RAM (FRAM)[7,8], magnetic RAM (MRAM)[9,10], phase-change RAM (PRAM)[11,12], resistance RAM (ReRAM or RRAM)[13,14], molecular switching memories/computing[15,16] and DNA memories.[17] Nevertheless, among them, FRAM, MRAM, PRAM and RRAM are typically considered as the emerging memories due to the current development and industrial acceptance.

FRAM memory, well-known its extremely high endurance and low power-consumption, stores the signal '0' and '1' by switching ferroelectric polarization between two distinguishable states.[18] MRAM switches the direction of magnetic moment, is of great interests in more extreme working conditions such as military use and aerospace applications.[9] Though both FRAM and MRAM have been on the market for more than 10 years, they only share a small portion in industry due to the difficulty of down scaling.[5] PRAM, sometimes referred as PCRAM (Phase-Change RAM), is typically made of chalcogenide materials. Data storage is based on thermally induced material phase change between crystalline

and amorphous[19], which causes resistance and reflectivity change of the material.[20] RRAM, also known as memristors, got its name since it is a resistor which “remembers” the amount of current that last passed through by exhibiting different resistance states. The concept was first proposed by Chua in 1971 as the fourth basic circuit element alongside capacitor, resistor and inductor since the behavior of memristor cannot be described my any other combinations of already known circuits elements.[21,22] With demonstrated lower programming voltage, faster read/write speed and remarkable scalability, RRAM is expected to replace existing NOR flash storage[6] or even NAND (NOT-AND) flash storage[23]. Memristor cells typically possess a metal-insulator-metal (MIM) structure comprising an insulating oxide sandwiched between two metal electrodes (top and bottom electrodes) with two or more distinct resistance states as the binary numbers of 0 and 1, constituting a conventional two-terminal structure devices with tunable electrical resistance upon external bias.[24] This reversible and nonvolatile resistance switching process between high resistance state (HRS) and low resistance state (LRS) is known as resistive switching (RS).

1.2 Remaining Challenges and Goals

Recent advancement in nanotechnology has enabled the current RRAM device scalability down to nanometer regime in last two decades. However, several challenges still remain to be addressed for the future high-performance devices:

1. Conventional top-down and ultra-high vacuum (UHV) deposition methods can achieve atomic level control fabrication but suffer from low

overall productivity. Due to the expensive fabrication equipment and relatively small working area, these high-cost approaches have limited potentials in the battle of next-generation memory devices[25]. Cost-efficient and facile fabrication methods are necessary in order to revolutionize the market.

2. The development of manufacturing method of integrating memory devices and circuits onto flexible and soft substrate is urgently required for wearable or printable electronic devices.[26] The study of NVM devices stretchability are still largely remained blank as most conventional MIM structure device materials are made of brittle ceramics. To solve this issue, the device with robust mechanical property and sufficient flexibility is required.
3. Although our technology has already achieved material atomic level manipulation, the precise nanometer resolution reproduction over a large area – mesoscale materials, is still a demanding process. The use of a template-based and self-ordered porous structure, anodic aluminum oxide (AAO), is an ideal master material for translating its own ordered nanostructure to those multifunctional materials which are difficult to pattern by traditional methods.

1.3 Dissertation Outline

Chapter 1 introduces the overall background, motivation and the remained challenges of the RRAM device. Chapter 2 presents a literature review of resistive

switching in detail, including classification of resistive switching and conductive filament formation mechanism. The most recent progress of RRAM devices, including the ultra-low energy consumption, fast-switching, high endurance and long retention devices are also reviewed. The discussion includes a thorough background knowledge of basic scanning probe microscopy (SPM) and modified variants such as conductive atomic force microscopy (C-AFM). The chapter also covers the current challenges and research motivations of future RRAM devices in the last.

Chapter 3 reviews the current progress of different approaches to synthesize ordered porous multi-component complex materials over a large scale. Starting with a brief background and survey with anodic aluminum oxide (AAO), one of the most used nanoporous templates, the chapter extends the scope to the direct anodization of more functional transition-metal binary oxides templates. The focus then shifts to the recent developments of porous complex functional materials templates, such as carbides, nitrides and perovskites (ABO_3) oxides fabrication utilizing AAO as master template, which would be extremely difficult to pattern over a large scale by conventional lithographic techniques. Highly ordered resistive switching HfO_2 nanocapacitors and TiO_2 nanoporous arrays are synthesized utilizing template assisted method as examples.

Starting from Chapter 4, studies involving solution-processed memristors comprising quasi-0D metal oxide nanoparticles are introduced. Chapter 4 introduces the fabrication of quasi-0D nanoparticles and solution-processed memristor. Two excellent previous studies regarding solution-processed memristor from our group have also been summarized. These pioneering studies

inspire my research motivations to further investigate low-cost but high-performance memristor devices.

Chapter 5 continues the storyline on solution-processed memristor, focusing on reducing RRAM device resistive switching operating voltage by making shorter ligand nanoparticle assemblies in order to decrease device overall energy consumption. A record-low switching voltage of solution-processed memristor has been achieved utilizing HfO_2 nanoparticles capped with 2-ethylhexyl phosphonic acid. The relationship between switching voltage and ligand length is also confirmed.

Chapter 6 is a comprehensive study of the nanoparticle size effect and substitutional effect on RRAM device switching voltage. By comparing the different sizes $BaZrO_3$ and $SrZrO_3$ nanoparticles capped with same phosphonic acid ligand, the trend between resistive switching voltage and nanoparticle size has been observed. By comparing the same size $BaZrO_3$ and $SrZrO_3$ nanoparticles, the effect of perovskite oxides substitutional effect on resistive switching is revealed. Through a series of systematic comparison experiments, we propose materials parameters including nanoparticle size, surface defects and geometric packing density, which are neglected in many studies but exhibit significant effect on the resistive switching performance of nanocrystal assemblies.

CHAPTER 2

MEMRISTOR FUNDAMENTALS

2.1 Basics of Resistive Switching

Resistive switching (RS) is a reversable nonvolatile phenomenon which changes resistance between a high resistance state (HRS) and low resistance state (LRS) based on the history of the applied external bias or current pulsing. This effect allows the fabrication of a new type of random access memory (RAM) device -- resistance random access memory (ReRAM or RRAM)[13], a promising candidate of next-generation electronic memory device competing with other new materials including ferroelectric random access memory (FeRAM)[27], magnetoresistive RAM (MRAM)[9] and phase-change RAM (PRAM)[11]. In resistive switching, the as-prepared memory cell usually needs to be activated by applying high voltage/current as initialization step (electroforming), which leads to the dielectric soft breakdown and results in a large decrease of the resistance. This electrochemical process creates a conductive path which ultimately connects top and bottom electrode. Subsequently, a reversible and controllable change in resistance between low resistance (LRS/ON state) and high resistance (HRS/OFF state) can be achieved by applying electric field that exceeds a threshold value ($V_{threshold}$). The resistance switching from HRS to LRS is defined as 'set process' and switching from LRS to HRS is 'reset process'. Thus, one can define four different resistance states of one memristor cell: 1). as-fabricated state; 2). as-electroformed state; 3). HRS and 4). LRS. In general, the as-fabricated state has a higher

resistance comparing to HRS[28] while as-electroformed state is comparable to LRS[29]. The operating voltage of a memristor is usually denoted as V_{SET} and V_{RESET}. Another term used to quantitively determine the performance of a memristor is the ON/OFF ratio defined as R_{OFF}/R_{ON}.

2.2 Classification of Resistive Switching

On the basis of I-V characteristics, resistive switching behavior can be classified into two categories: unipolar switching (URS), bipolar switching (BRS), threshold switching (TS) and complementary switching (CRS).[30–33] Unipolar switching only depends on the amplitude of in the input (voltage/current) and has been found in many binary transitional oxides such as NiO[34,35], ZnO[36], HfO_2[37] and TiO_2[38]. Bipolar switching shows directional resistive switching depending on polarity and amplitude.[39] This type of resistive switching can also be observed in HfO_2[37,40], TiO_2[41,42] and perovskite oxides such as $BaTiO_3$ (BTO)[43,44], $SrZrO_3$ (SZO)[45,46] and $BaZrO_3$ (BZO)[47]. Unlike unipolar and bipolar switching, threshold switching is a reversible volatile process where upon the application of an applied bias generates current flow and a significant amount of internal Joule heating[48,49]. In fact, it is not uncommon that two or even three types of resistive switching behaviors coexist in one type of material. This is due to the conductive filament formation and rupture is largely determined by Joule heating induced by the electrical current.[35,41,50] Complementary resistive switching is a relatively new concept first proposed by Eike Linn and Rainer Waser in 2010.[31] A typical CRS cell is comprising of two anti-serial connected BRS

memory cells. By merging two resistive cells into one structure, sneak path problem is greatly resolved and hence the device power consumption is drastically reduced. In 2012, single resistive cell CRS based on tantalum oxide was reported by Yang *et al.*, which is a promising candidate for large-scale crossbar resistive arrays[51].

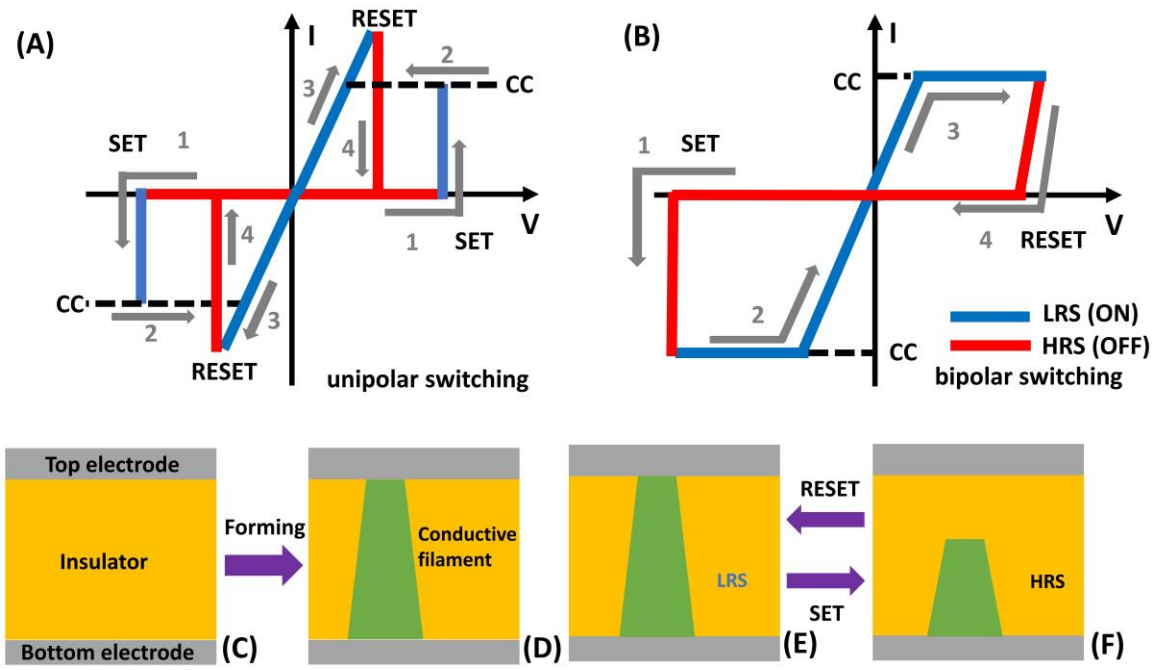

Figure 2-1 (A) Typical unipolar resistive switching and (B) bipolar resistive switching. (C) Schematics of virgin state memristor (D). As-formed state(E). LRS and (F). HRS

2.3 Resistive Switching Mechanisms

The exact origin of resistive switching behavior is a long-debated issue and it depends on electrode material, insulator material and operating methods. Most resistive switching behavior can be categorized into anion migration, cation migration and thermochemical reaction[52].

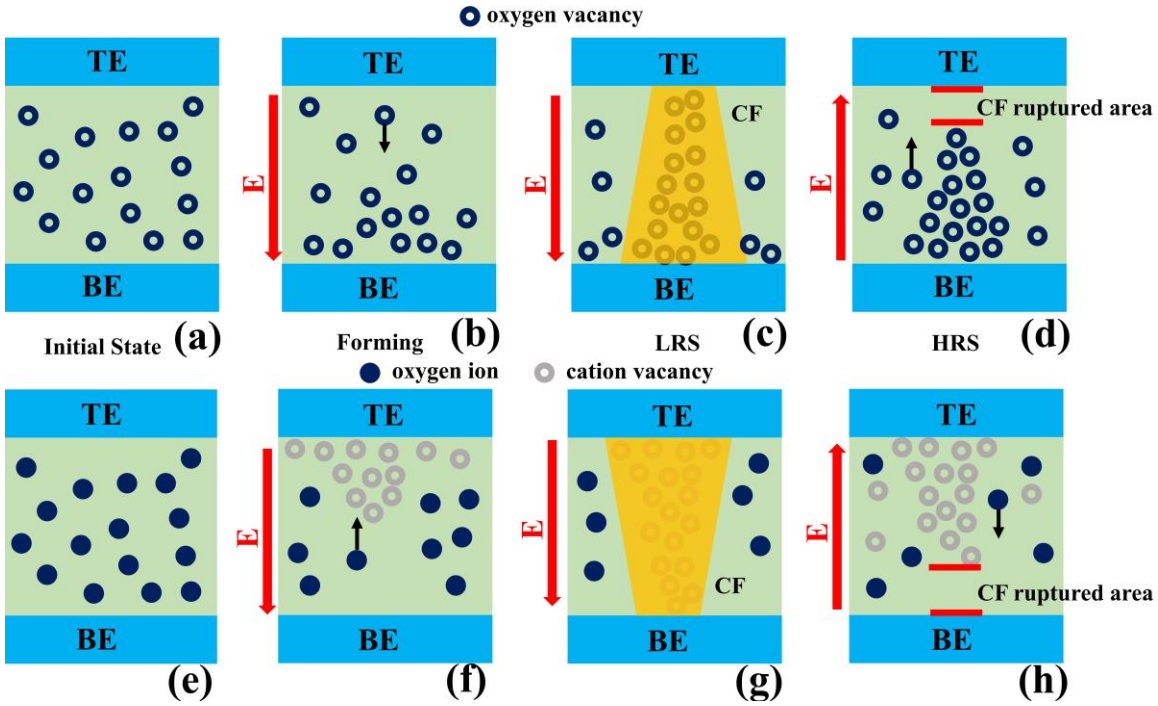

Figure 2-2 (a)-(d) Charged ion behaviors in n-type storage materials; (e)-(h) charged ion behaviors in p-type storage materials.

In anion migration type resistive switching, the charged non-stoichiometric ions (e.g. oxygen vacancies or oxygen ions) will migrate inside of the insulator as driven by external voltage. Therefore, there will be a local valence variation at the insulator/electrode interface due to the accumulation and redistribution of charged ions.[53] In n-type storage materials, the insulator already has excessive positive charged oxygen vacancies (V_O), as illustrated in Figure 3a. The positively charged oxygen vacancies will move along the electrical field direction and accumulate at the bottom cathode/insulator interface (Figure 3b). The conductive filament is subsequently formed since the accumulated oxygen vacancies are extending to the top electrode (Figure 3c). Therefore, the formed cone shape conductive filament has the thinnest spot near top electrode. Most of the Joule heating will be generated at the thinnest part and conductive filament will rupture

near the top electrode under reverse voltage (Figure 3d).[54] On the contrary, in p-type storage materials, the filament rupture region is on the opposite electrode. The more prevalent negatively charged oxygen ions (Figure 3e) will migrate and accumulate to the anode/insulator interface and thus generating cation vacancies nearby (Figure 3f). The accumulated cation vacancies are hole carriers in p-type semiconductors served as top electrode extension reaching to the bottom electrode (Figure 3g). Therefore, the conductive filament is breaking at the vicinity of bottom electrode under the reversed electrical field (Figure 3h). Anion-type memristors always result in a valance change within the storage materials and are categorized as valance change memories (VCM).[55] This type of resistive switching behavior is usually observed in non-stoichiometric metal oxides such as HfO_x[56], TaO_x[57,58], $BaTiO_{3-x}$[59] and nitrides such as NiN[60].

Another category is cation-migration memristors, often referred as electrochemical metallization memory (ECM). In ECM cells, one side of the electrode is usually an electrochemically active metal such as Ag[61] and Cu[62]. The other electrode is electrochemically inert such as Pt and W. The redox and electrochemical dissolution process take place under high electrical stress. The produced cation ions such as Ag^+ and Cu^{2+} migrate along electrical field direction to the cathode acting as conductive bridge and form conductive filament, which short circuits top and bottom electrode switching device from HRS to LRS. Thus, ECM memory is also referred as conductive bridging RAMs (CBRAMs)[63]. Conductive filament is ruptured because of the Joule heating induced by negative bias. Intensive researches have been carried out to investigate cation-migration resistive switching, including the use of Ag[64], Al[65], Ti[66], Zn[67] and so on.

Thermochemical based RRAM often exhibits unipolar and threshold switching behavior. In non-polar switching, the RESET process is not due to the retraction of migrated charged ions. The Joule heating can greatly increase the temperature in the conductive filament necking area and thus rupture the filament. Because Joule heating is induced by current, which is independent to voltage polarity, thermochemical reactions usually take place in non-polar switching.[13] Alternatively, unipolar and threshold switching can be triggered in bipolar switching RRAM cells by introducing higher Joule heating in the process. There are three common ways to control Joule heat in resistive switching process: i). Current compliance.[50,68] For example, Razi *et al.* observed transition from bipolar switching to threshold switching behavior in Ag/BTO/Ag by increasing the current compliance to 10^{-4} A in a 142 nm thin film structure.[68] ii). Ambient temperature. The thermal bi-stability of the conductive filament and also be observed by conducting I-V cycles in both low and high temperature.[35] iii). Metal electrode thickness. In addition, unipolar and threshold switching can also be induced by varying electrode thickness and hence controls the Joule heat dissipation.[34]

2.4 RRAM Device Performance and Challenges

The critical parameters to evaluate the performance of a RRAM device are endurance, stability, read/write speed, retention time and energy consumption.[69] Lee *et at.* reported a TaO_x based asymmetric passive switching device with extremely high endurance and stability up to 10^{12} cycles.[32] Sub-

nanosecond resistive switching was achieved by voltage cycling at 20 GHz on tantalum oxide memristor.[70] Gao group demonstrated Ag/P3HT:PCBM/ITO device has minimal storage degradation up to 9 months in room temperature and over 10 years by extrapolating the experimental data.[64] Ultra-low energy consumption RRAM with less than 0.1 pJ per bit and more than 5×10^7 cycles endurance has also been realized in Hf/HfO_x RRAM device.[71] All of these amazing records were achieved within recent 10 years and each one of the characteristic is far superior than current FLASH memories. However, integrating all exciting aspects into one single system is still a challenge.

Theoretically speaking, RRAM devices have excellent scalability since the minimum device active area is defined as one single conductive filament (CF). Depending on different resistive switching mechanisms, the area of one single CF is often a few atomic units.[72] However, instead of forming one main filament, CF-based resistive switching tends to form multiple branched filaments.[67,73] The thinner and weaker filaments introduce intense operational parameters variations such as operating/switching voltages, ON/OFF ratio and hence cause further device performance issues such as retention and endurance problems.[74] In CF-based resistive switching, the formation and rupture of CF does not depend on both electrodes. This phenomenon is verified by conducting I-V curves on same type of devices with different electrode sizes.[75] Studies focusing on conductive filament real-time observation have been carried out utilizing transmission electron microscopy (TEM) and conductive atomic force microscopy (C-AFM).[76–78]

2.5 Atomic Force Microscopy (AFM) Characterization

As the miniaturization of devices goes down to nanoscale range, atomic force microscopy is the optimal option for memristor local characterization. An atomic force microscope (AFM) consists of a piezoelectric actuator, a micro-machined probe with an extremely sharp tip (1~30 nm) at the end, a laser, a position sensitive, four-quadrant photodiode, and a feedback loop control system, as illustrated in Figure 4a.[79] There are three common surface imaging modes: contact mode, tapping mode and non-contact mode. The general AFM working principle is to first align the laser pointing on the back side of the cantilever, so the laser signal is reflecting to the photodiode as input. During scanning, cantilever deflection (contact mode) or cantilever oscillation amplitude (tapping mode and non-contact mode) is set to a fixed setpoint depending on tip-sample interaction. The AFM probe deflection or oscillation amplitude will change as the probe scans the sample and encounters height variations on sample surface and hence leads laser point movement on photodiode due to the laser beam deflection on cantilever. The AFM feedback loop will constantly adjust the piezoelectric actuator height to keep the setpoint constant. The movement of the actuator is then recorded as sample microstructure dimension data. The phase and amplitude image in tapping and non-contact mode provides extra sample property information such as mechanical property and viscoelasticity.[80]

Because of the multi-functional AFM probe, AFM provides additional capabilities over conventional electron microscopy techniques such as scanning electron microscopy (SEM) and transmission electron microscopy (TEM). For

example, magnetic force microscopy (MFM) is based on AFM technique scanning with a magnetized probe measuring sample magnetic field gradient.[81] Because of the ultra-shape tip and accurate force modulation, AFM is also largely used for ultra-thin sample nanoindentation for sample mechanical testing.[82,83] AFM also has a broad variations for electric property measurement with metalized probe including surface potential (Kelvin-Probe Force Microscopy)[84,85], electrostatic force microscopy (EFM)[86,87], piezo force microscopy (PFM)[88,89] and conductive atomic force microscopy (C-AFM).[90–92]

Conductive-AFM (C-AFM) uses a conductive AFM probe (metal coated or N-doped silicon) as a movable electrode. In Asylum Research ORCA™ C-AFM system, AFM samples stage serves as bottom electrode and applies bias while conducive probe is held grounded. In C-AFM mode, AFM operates in contact mode while biasing sample from bottom electrode. The current flows through conductive probe and then passes into amplifier as current signal output as the tip scans on sample. The surface topography and current mapping is thereby recorded simultaneously. The dual gain module uses two separate standard module and is capable of measuring current from ~ 1pA to 10μA. The major advantage of C-AFM over conventional probe station is its application in many nano-scale electronics due to its sharp conductive tip and accurate force.[93] For example, Walker *et al.* firstly demonstrated and measured the electrical conductivity of an 10 nm Archaeal protein nanowire by placing the probe with 1 nN force after calibration.[92] As the technology advances, C-AFM is becoming one of the major characterization tools for RRAM nano-scale devices.[94]

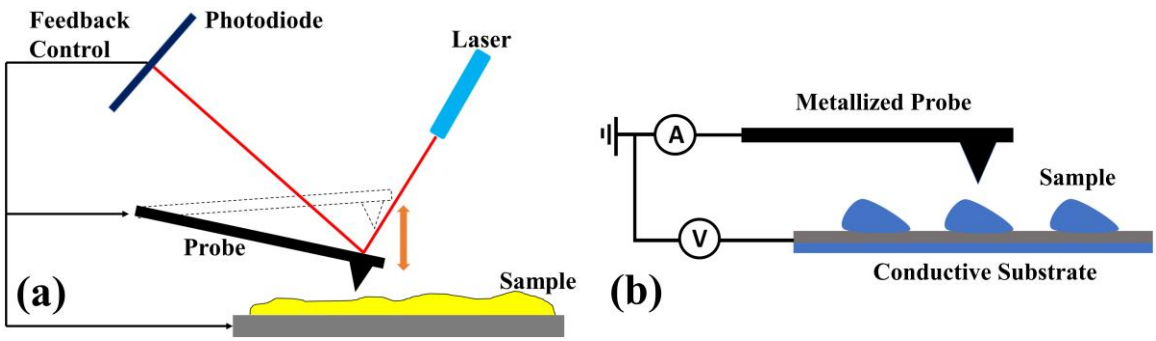

Figure 2-3 (a) Schematics of AFM. (b) Conductive-AFM illustration. In Asylum Research AFM system, sample bias is applied from bottom electrode and conductive probe is held grounded.

2.6 Summary

This section covered the working principles and recent progress of RRAM devices. Virtually all recent studies utilize costly and time-consuming conventional ultra-high vacuum (UHV) deposition and lithographic patterning methods. A more cost-effective and efficient fabrication approach necessary for RRAM to standout in the competition of emerging memory. In addition, the rapid development of wearable and printable electronics market demands a flexible but robust device which would be difficult to processed by traditional top-down fabrication methods. Two different low-cost and facile methods for fabricating unique complex oxide nanostructures that exhibit promising functionality, including resistive switching will be demonstrated in subsequent chapters: 1). Nanoporous arrays using a modified top-down approach inspired by the production of anodic aluminum oxide (AAO); and 2) nanoscale assemblies comprising solution-processed binary oxide and perovskite oxide nanocrystals using a blade-assisted convective assembly approach.

CHAPTER 3

PRODUCING NANOPOROUS ARRAYS WITH FUNCTIONAL COMPLEX OXIDES

3.1 Introduction

The use of template-based synthetic processes has rapidly grown over the last two decades due to their relative simplicity compared to expensive lithographic approaches and effectiveness in producing scalable 1-D and 0-D nanostructure arrays. Porous membranes such as anodized metal oxide templates[95–97], mesoporous carbon[98], zeolites[99], polymer templates[100,101] and nanochannel arrays on glass[102] have been employed in biomedical, optoelectronic, and sensing applications. The majority of templates fabricated comprise binary metal oxides due to their high thermal stability, mechanical compliance, relative abundance, and facile fabrication method. Since the alumina self-organized mechanism was first reported by Keller more than 60 years ago, anodic aluminum oxide (AAO) received immediate interest as a means to synthesize nanoscale structures and devices[103,104]. During a single-step anodization, the pores develop randomly on the oxide surface, limiting their use as a template. The electrochemical oxidation of transition metals, including hafnium (Hf)[95,105], tantalum (Ta)[106–109] and titanium (Ti)[110–112], also produce a porous thin film structure on their surface. Older studies that achieved ordered nanostructures required time/cost intensive methods such as focused ion beam (FIB) milling, scanning probe scraping, or hard SiC/Si_3N_4 molding to produce a

pre-pattern step on the surface[113–115]. In the mid-1990s, Masuda and Fukuda overcame this challenge by pioneering a two-step anodization process in an acidic electrolyte that produced an aluminum oxide thin film which possessed a uniform nanoporous internal structure[104]. Unlike conventional lithographic processes, this inexpensive method enables scalable formation of a periodic pore network over a relatively large area by adjusting parameters such as applied voltage, temperature, and electrolyte selection.

Here we review the latest advances in nanoporous templates that extend beyond anodic aluminum oxide templates to include nanostructured complex materials derivatives. This review begins with a brief survey of anodic aluminum oxide (AAO), the most commonly used nanoporous template for 1D and 2D nanomaterials fabrication. The scope of nanoporous templates is then extended to include transition metal oxides and alloy oxides. These metallic-derived templates use the same AAO anodization technique but possess more inherent functionality than a wide-gap insulator such as alumina. In the final portion of the review the focus shifts to highlighting recent developments of complex compound porous templates requiring the use of AAO reverse templates, a nanoporous template that mirrors the porous network of AAO yet comprise multicomponent, functional materials such as carbides, nitrides, and perovskite (ABO_3) oxides.

3.2 Anodic Aluminum Oxide (AAO) Fabrication and Its Applications

High purity aluminum (>99.99%) is first annealed in inert atmosphere at 500°C to release internal mechanical stress. The aluminum foil is degreased in

organic solution and then polished to obtain a clean and defect-free surface ready for first anodization. Anodizing voltage, type of electrolyte and temperature are the key factors affecting AAO membrane feature, such as pore diameter (D_{pore}), interpore distance (D_{int}) and oxide layer thickness. Amongst three most used electrolytes, sulfuric acid shows best results in terms of pore structure and distribution, oxalic acid yields pores with moderate size and regularity, phosphoric acid gives largest but least uniform pores.[116] After the first anodization, the aluminum is exposed in the mixture of chromic and phosphoric acid solution at 50°C. This chemical etching step selectively removes oxide layer without damaging aluminum substrate, leaves an ordered and textured surface for second anodization.

To successfully form AAO, the second anodization is usually carried out under the same condition as the previous step. In some special cases, mostly for ultrathin AAO membrane fabrication, the second anodization condition varies in time or operating temperature to obtain membrane in desired thickness. Nielsch et al. reported 10% porosity is the optimum condition for self-ordering porous alumina structure due to the 1.2 volume expansion rom aluminum to alumina.[117] In order to increase porosity, immersing template in 5 wt % phosphoric acid at room temperature is a common post anodization process which further enlarges pore size without changing interpore distance. [118–120] Also, some other groups demonstrated a novel method to precisely reduce pore size by atomic layer deposition (ALD), which is well-known for uniformity and thickness control. [121–123] By coating Al_2O_3 on the template surface, pore diameter can be narrowed down to 5 nm without bringing impurities to the sample.[124]

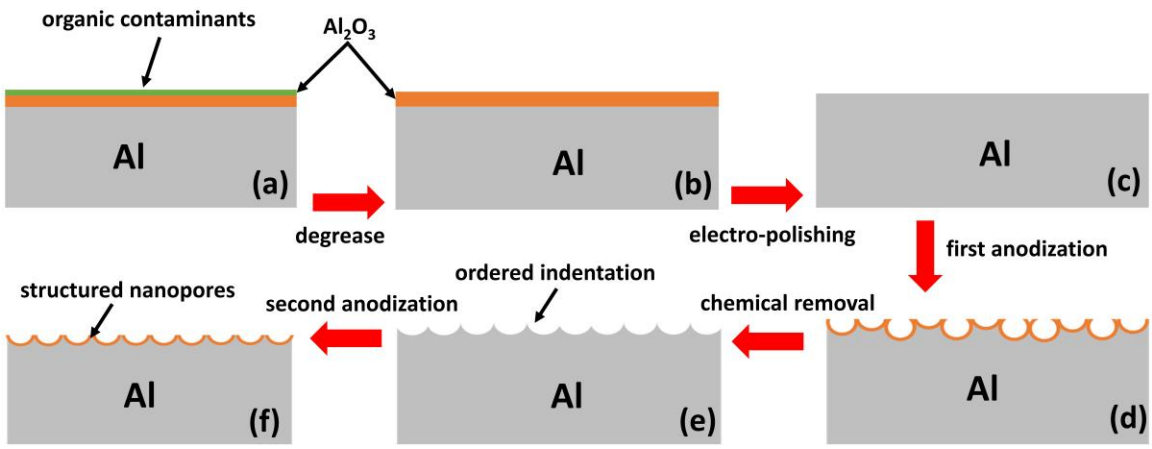

Figure 3-1 (A) commercially available high purity aluminum foil. (b) Removing organic contaminants by degreasing. (c) Removing surface aluminum oxide by electro-polishing. (d) First anodization forms irregular nanoporous structure. (e) Chemically dissolve unordered Al_2O_3 leaves ordered indentation on aluminum foil. (f) Second anodization generates highly ordered AAO nanostructure.

The AAO fabrication process enables tailoring of pore diameter (D_{pore}), interpore distance (D_{int}) and oxide layer thickness by controlling parameters such as the anodizing voltage, temperature, and electrolyte type. For a two-step anodization, the high purity aluminum undergoes an initial anodization step followed by a chemical etching step (typically with chromic/phosphoric acid) that selectively removes the newly formed, yet irregularly patterned aluminum oxide layer without damaging the aluminum substrate, resulting in an ordered and textured surface available for a second anodization. This textured surface creates accurate pore growth positions during the second anodization since pore nucleation preferentially occurs at surface defects. The second anodization is usually carried out under the same condition as the first step. The duration of this second anodization process will control the final thickness of the AAO membrane. The AAO geometric structure is also adjustable by post-anodization processing.

Immersing the template in dilute phosphoric acid at room temperature enlarges the AAO pore size without changing the interpore distance.[118–120] Conversely, conformal Al_2O_3 coatings through atomic layer deposition (ALD), a method with high uniformity and thickness control,[121–123] is capable of narrowing the pore diameter down to 5 nm.[124] For more details concerning conventional AAO fabrication technique and its direct applications in nanomaterials, we suggest reading some excellent review articles on AAO fundamental principles, techniques and applications.[113,125–128]

3.2.1 AAO Template Assisted Fabrication of Nanodots Arrays

Aluminum anodization is a cost-effective, highly-controllable, and easily scalable process that produces an ordered array of vertical channels that have been used extensively for the fabrication and synthesis of nanostructures and devices ranging from 0-D (nanodots, nanoislands) to 1-D (nanowires, nanotubes). Ultrathin AAO templates, defined as those possessing an aspect ratio (pore depth to pore diameter ratio) of less than 10, can be separated from its host aluminum substrate and transferred to second, arbitrary (functional) substrate when reinforced with a polymer coating such as poly (methyl methacrylate) (PMMA) or polystyrene (PS) that assists with mechanical compliance.

AAO-directed fabrication of ordered 40 nm Au nanodot arrays on a silicon substrate were among the first templated synthetic studies conducted in the late 1990s.[129] This method circumvented the need for costly electron beam lithography, which typically suffers for low throughput due to its prolonged

exposure time. Other metals, such as Au, Ni, Co, and Fe, have also been deposited on a variety of substrates using this approach.[130,131] Recent studies that employed ultra-low aspect ratio membranes (1:2) have extended this approach to achieve nanoisland diameters down to 16 nm.[132] High-density nanoisland arrays have also be extensively studied as an ideal architecture for functional oxides, which exhibit remarkably different properties than conventional bulk materials.

Ultrathin AAO template is a suitable candidate for aggressive fabrication condition since Al_2O_3 is a high temperature and chemical resistant material. This unique advantage enables the coexistence of ferroelectricity and resistive switching behavior on one individually addressable nanocapacitor. Liu group fabricated 60 nm epitaxial BiFeO3 nanodots on Nb-$SrTiO_3$ substrate using high temperature pulsed laser deposition (PLD) through ultrathin AAO template.[133] Interfacial based resistive switching performance can be greatly enhanced by surface charge redistribution induced by ferroelectric switching.[134] The pioneering work of Lee et al. reported on the ultrathin, template-directed fabrication of a versatile metal/oxide/metal (M-O-M) (Pt/PZT/Pt) nanoisland nanocapacitor structure deposited on MgO single crystal substrate .[135] The isolated pattern localized the electric field distribution, minimized the effective cross-talk between structures, and enabled each nanocapacitor to be individually addressable , thus the array exhibited an extremely high storage density (176 Gb $inch^{-2}$).[135] Template-directed fabrication of nanocapacitors comprising functional materials such as HfO_2 and Ag_2S (not shown), have been used to form nanoscale memristive cells, which show controllable resistive switching (RS) properties suitable for

nonvolatile memory applications.[121] The combination of highly tunable, scalable templates and thin film deposition creates large arrays of M-O-M nanocapacitors, thus becoming one of the most precise and convenient methods in nanomaterials test structure fabrication. Other studies deposited cobalt ferrite oxide (CFO) nanodots epitaxially through ultrathin, template-directed pulsed layer deposition (PLD). By tuning the anodization conditions, the magnetic behavior of nanodots (60-300 nm diameter and 60-500 nm interpore distance) were observed via magnetic force microscopy (MFM), with clusters comprising smaller diameter nanodots exhibiting dipole-dipole interactions of opposite phase and larger diameter nanodots possessing opposing phases within a single structure.[136]

Our group also successfully fabricated individually addressable functional metal oxides functional nanodot arrays using ultra-thin AAO template assisted method. Figure 3-2 (a) shows the M-I-M nanodots arrays fabrication process. A piece of polystyrene (PS) reinforced ultrathin AAO membrane (100 – 200 nm, TopMembrane, Shenzhen China) is first transferred to a metalized substrate with PS side facing up. PS is subsequently dissolved by immersing the sample in acetone for 30 minutes. Metal oxide material is deposited by either RF sputtering or atomic layer deposition (ALD). Nanocapacitor top metal electrodes can be a metalized probe (typically Pt) or one additional step of metal deposition to yield ordered arrays of nanocapacitor arrays (Figures 3-2(b) and (c)). Figures 3-2 (d) and (e) show the C-AFM I-V spectroscopy response of 20 nm and 100 nm diameter nanocapacitors, respectively. The structures display countereightwise bipolar switching, characteristic of filamentary - type mechanisms. Comparison of 100 nm

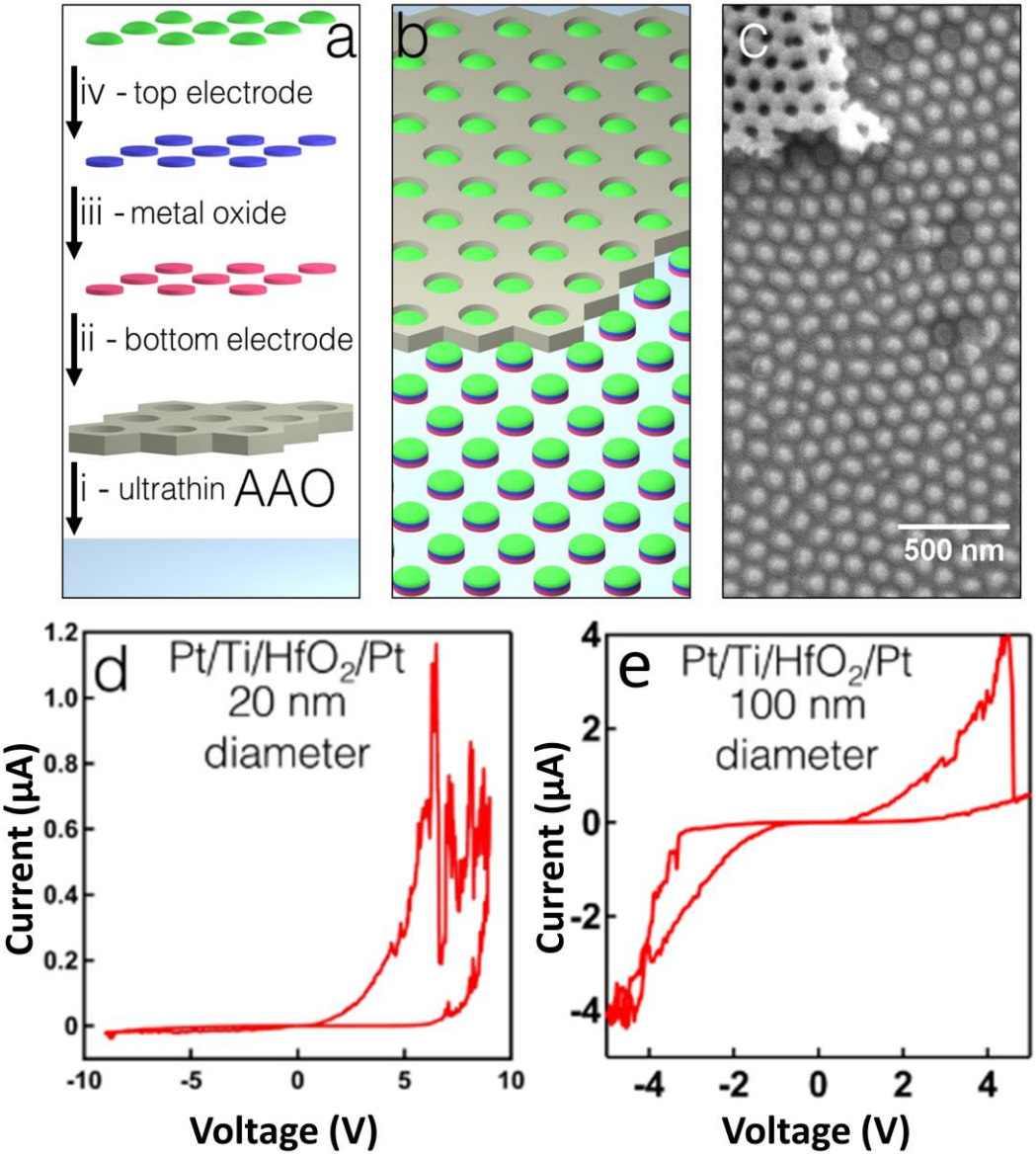

Figure 3-2 (a) and (b), schematics of AAO templated assisted nanocapacitor fabrication. (c) SEM image of Pt/HfO_2/Pt nanocapacitor with partially removed AAO template. (d) and (e), local I-V response of 20 nm and 100 nm HfO_2 nanocapacitor respectively

and 20 nm diameter HfO_2 nanocapacitors show that smaller nanocapacitors become more rectifying and exhibit a greater degree of asymmetry.

3.2.2 AAO Template Assisted Fabrication 1-D Nanostructures

One dimensional nanostructure such as nanorods, nanowires, and nanotubes demonstrate enormous potential in the fields of magnetic, electronic, and optoelectronic devices. Nanorods possess an aspect ratio of less than 10, while nanowires are defined by an extremely high aspect ratio, usually exceeding 1000. The high degree of controllability of AAO dimensions, including accurate control of nanowire length and diameter, motivates the use of AAO-template-assisted approaches such as electrodeposition and sol-gel as attractive alternatives to multistep lithographic methods.

Examples include high density nickel (Ni) nanowires arrays , which exhibited an increase in magnetic coercivity with decreasing Ni nanowire diameter and subsequently improved magnetic hardness.[137] Each nanowire was capable of being switched independently, thus producing a recording density up to 155 $Mbit/mm^2$ for Ni nanowire array, significantly higher than the density within currently available hard drives (5.74 $Mbit/mm^2$).[127] One-dimensional nanostructures inherently possess high surface-to-volume ratios, motivating their use as next generation power source electrodes and microbatteries. Freestanding aluminum nanorod electrode arrays were produced by template-directed electrodeposition,[138] which were subsequently coated with a thin layer of titanium dioxide (TiO_2) via atomic layer deposition (ALD), which resulted in an increase of the overall capacity by an order of magnitude and the stability for over 50 charge-discharge cycles.[139]

AAO templates also assist the synthesis of low melting point metals, semiconductors, and functional polymers nanowires by vacuum melting and solution wetting[140–145] Due to its inherently porous nature and

biocompatibility, AAO is also widely applied in biochemical fields such as drug delivery, tissue engineering and biocapsules.[146–149]

3.3 Transitional Metal Oxides and Alloy Templates

The enhanced surface area of template-fabricated 0-D and 1-D nanostructures motivates their use in gas sensing,[110,150] photovoltaic,[151] and water splitting[108,109,152,153] applications, among others. Over the past 20 years attempts to extend template fabrication beyond Al_2O_3 to construct nanoporous networks in other functional (binary) metal oxides have progressed rapidly. Since the discovery of self-organized pores within TiO_2 in 1999,[154] advanced anodization methods have been applied to a wide variety of transition metals. Unlike AAO, which comprises a continuous porous network, anodic titanium oxide (ATO) templates consists of individual nanotubes produced by a one-step anodization process (Figure 3-2a).[97] Annealing the amorphous, as-grown ATO template converts it into its crystalline anatase form, which possesses

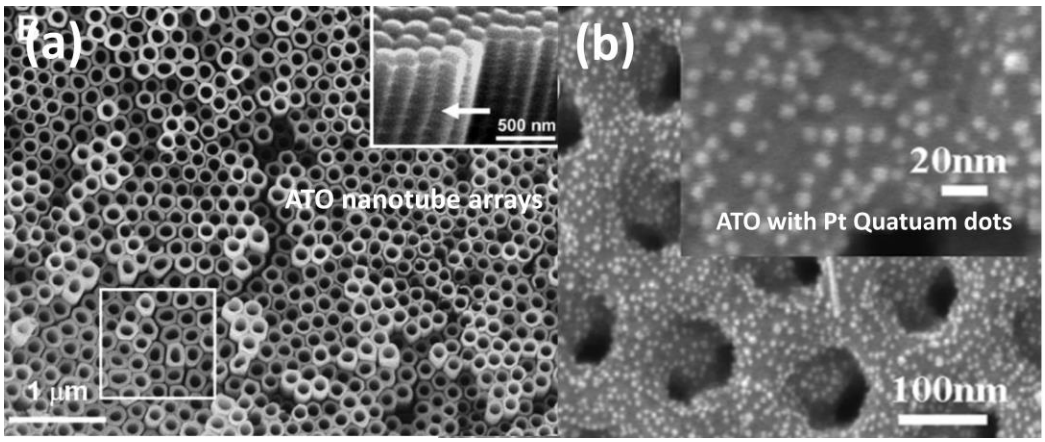

Figure 3-3 (a). Typical ATO nanotube arrays from Ref 3, 2008 Wiley-VCH; (b). Pd quantum dots deposited on ATO arrays from Ref 64, 2012 American Chemical Society.

a higher charge carrier mobility.[155] ATO nanotubes possess a large surface area and a short diffusion pathway, and thus attracts considerable interest as anodes in dye-sensitized solar cells (DSSCs), which have been extensively studied as an energy harvester due to their excellent light to electricity conversion efficiency.[111,112,156–158] The photocatalytic activity can be further enhanced through the deposition of noble metal nanoparticles over the nanotubular structure surface (Figure 3-2b).[159]

Due to the relative easiness to manipulate the oxygen concentration, TiO_2 is also a prototypical dielectric material for memristor research to reveal filament type resistive switching working mechanism due to the localized drift of oxygen vacancies.[160] In 2009, Hewlett-Packard a flexible solution processed Al-TiO_2-Al memristor achieved less than 10 V operating voltage (relatively low power for flexible and ON/OFF ratio greater than 10,000.[161] The spin-coated so gel method was the first attempt making flexible memristive device. Though TiO_2 based memristor does not have the best overall performance as compared to the newly-invented memristive structure, it is one of the first and most extensively studied memristive material.[162]

Tantalum pentoxide (Ta_2O_5) is a high-κ dielectric used in a wide range of applications such as dielectric layers for storage capacitors,[163] implant coatings,[106] as well as an efficient photocatalyst for water decomposition.[164] Anodization and annealing processes of high purity tantalum create a facile fabrication route for Ta_2O_5 semiconductor nanotube arrays. As one of the most stable transition metals, Ta-based Ta_2O_5 can withstand ultra-high temperatures without compromising its microstructure. Tantalum oxide drew much attention

recently in emerging memory field due to its extreme high endurance of cycles and uniform switching. It is reported that engineered Ta_2O_5/ Ta_2O_{5-x}/ TaO_X exhibit nearly unlimited endurance of 10^{11} cycles at 30 ns with highly uniform switching of bit error rate below 10^{-11}.[165] Kim et al. also reported a self-limited mechanism enhancing the uniformity of both SET and RESET resistance with Ta_2O_5/ TaO_X structure.[166] .[109]

Due to the nature of self-organization, nanoporous binary oxide templates result from competing chemical dissolution and electrochemical formation processes.[126] Use of a single type of metal limits the geometric degrees of freedom and thus yield a hierarchically ordered structure. As shown by the various examples above, materials functionality is greatly enhanced by the multi-scale features of the nanoporous template. Such an approach motivated exploration into the synthesis of multicomponent oxides by the anodization of alloys. The anodization of Group VB and IVB valve metal alloys has two main advantages: *1) Biocompatibility*. Transition metal alloys have been widely studied and used for implants due to their superior biocompatibility and corrosion resistance compared to their (individual) metallic constituents.[167–169] *2) Transition metal-like properties*. Anodization ideally maintains balance between chemical dissolution and oxide formation. The chemical properties of transition metals minimize two major problems hindering common alloy anodization: *i)* different dissolution rates of the constituent elements and *ii)* varying reaction rates in different alloy phases. This unique feature ensures the uniformity of self-organization during anodization of binary oxides.

Yasuda demonstrated excellent structural flexibility and controllability of alloy oxides nanotube by tuning the zirconium titanate (ZT) nanotube arrays morphology (Figure 3-3a).[170,171] Pure zirconia nanotubes processed by conventional methods possessed a nominal diameter of 50 nm and a length of 17 μm,[172] while pure titanium oxides nanotubes possessed a nominal diameter of 100 nm and a length of 2.5 μm.[111] When anodizing a 50:50 wt% Ti-Zr alloy in 1M $(NH_4)SO_4$ + 0.5 wt% NH_4F solution, the oxides matrix showed significantly higher controllability of the structure: the pore diameter ranged from 15 to 470 nm and the length up to 21 μm, depending on the anodization conditions. Anodization of the single-phase metal alloy $Ti_{29}Nb_{13}Ta_{4.6}Zr$ in a fluoride-based electrolyte produced a unique two-scale pore diameter (d = 32 nm; 55 nm) within a single oxide porous template (Figure 3-3b).[173] Auger electron spectroscopy (AES) determined that the tantalum oxide composition was increased in both 32 nm and 55 nm nanotubes in comparison with other metal oxides throughout the alloy oxides layer, which proves the higher chemical dissolution rate of the other metal oxides. This coincides with the fact that Ta_2O_5 has the highest chemical stability

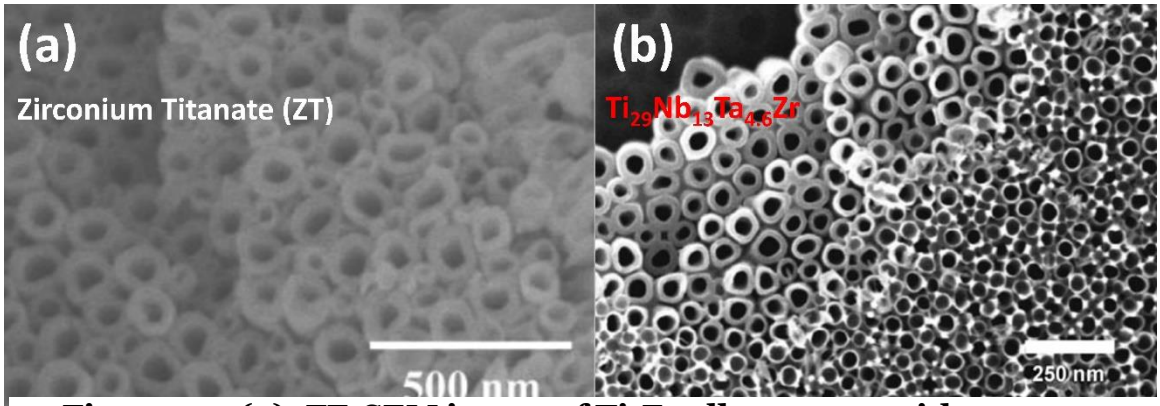

Figure 3-4 (a). FE-SEM image of Ti-Zr alloy arrays with ~ 90 nm diameter and ~ 30 nm wall thickness, reproduced with permission from Ref 76, 2007 Wiley-OCH; (b). Alloy nanotubes broken off at different height levels from Ref 79, 2006 Wiley-VCH.

among all other transitional metal oxides, which means it has the lowest chemical dissolution rate.[107] The results demonstrate even subtle changes in alloy chemical composition can induce large variations in oxide formation, thus motivating new anodization processing directions for multi-scale porous template fabrication.

3.4 Functional Reverse Template

The well-studied effects of anodization conditions on sample morphology and geometry enables fine tuning of pore size, pore density and channel length of oxide templates. Routine production of pore diameters ranging from 20 nm to 500 nm and aspect ratios from < 10 to 1000s yield a robust, versatile platform to explore size effects within nanoscale materials. The preceding sections highlighted three primary advantages of using oxides templates. 1) Template-directed nanostructure deposition: Due to their highly uniform, periodic porous structure, oxide templates enable top-down, size-controlled fabrication of electrochemically deposited or sputtered/evaporated metal and metal-oxide nanostructures. 2) Catalyst supports: Various catalytic processes are greatly enhanced due to the extremely large surface area provided by oxide templates. 3) Inexpensive, facile fabrication. Uniform nanoscale features are easily reproduced without using traditional expensive lithographic techniques. Applications utilizing AAO templates, however, are restricted by the limited, inherent functionality of alumina or other binary oxides.

From an application standpoint, developing 2D nanoporous arrays in complex oxides confer functional properties that extend beyond AAO templates to include ferroic behavior, defect-mediated memristive switching, and biocompatibility, among many others. Due to their chemical stability fabrication of 2D templates comprising complex oxides and noble metals must use conventional methods such as lithography and nanoimprinting. These expensive, time-consuming techniques severely hinder the development and application of functional oxide templates. Thus, 2D functional material template fabrication requires new template-assisted methods to create ordered, nanoporous arrays. The so-called 2D anti-dot nanostructure remains one underexplored, yet viable option towards achieving these nanoporous arrays. Three major anti-dot array fabrication methods exist: 1) direct deposition; 2) plasma etching; and 3) reverse replica fabrication.

3.4.1 Direct Deposition: Magnetic Storage Media

Direct deposition uses the engineered AAO template of a chosen geometry and dimensions as the substrate for conventional deposition methods such as sputtering, atomic layer deposition (ALD) and thermal evaporation.[174–176] Well-developed deposition techniques are able to control the deposition thickness on the Angstrom (Å) level and thus preserve the original morphology of AAO template.[122,177] Porous magnetic structures have been extensively studied in the last decade due to their potential as ultra-high density magnetic storage media and the rich, fundamental physics underlying their operation.[178–180] As

compared to individual nanodots, anti-dot arrays generally display two advantages: *i)* superparamagnetism does not exist nor hinder the data-storage unit size since the storage device is a continuous film;[181] and *ii)* coercivity and remanence can be controlled by varying anti-dot pore size.[182] However, most studies utilize inefficient traditional patterning approaches such as block co-polymer templating and lithography. Expensive fabrication equipment, small deposition areas, and relatively large feature sizes (200 nm to 400 nm) all limit use of these techniques in producing next-generation anti-dot device arrays.[179,180] AAO templates represent a viable alternative due to easily tunable pore diameters below 50 nm. AAO-produced magnetic 2D nanostructures have displayed a storage density of 1 Tb in^{-2},[183] motivating further miniaturizing of magnetic storage components and creating a competitive candidate system for future high-density magnetic data storage devices.

While vacuum deposition techniques can routinely produce complex oxides thin films with other functionalities such as resistive switching and ferroelectricity, deposition of ultra-thin films on AAO surfaces to produce anti-dot arrays have been mostly limited to magnetic metals as the deposited thin film cannot be separated from the AAO template. This renders alumina, an electrical insulator, as a poor substrate for developing modern metal-insulator-metal (MIM) structured nanocapacitors.

3.4.2 Dry Etching: Multiferroic Bismuth Ferrite Anti-Dot Arrays

Combining conventional AAO-directed fabrication with top-down ion etching methods allows the user to separate film fabrication from morphology modification, resulting in a more flexible operating parameter window while improving thin film quality. In this process a pre-engineered through-hole AAO serves as a nanostructured mask (Figure 3-4 a-i) as transferred on a desired substrate (Figure 3-4 a-ii) comprising a functional material, either a metal or metal oxide. Then ordered nanohole arrays are fabricated by conventional dry etching processes such as ion milling, reactive ion etching (RIE) and plasma etching (Figure 3-4 a-iii, iv) [126,130,184–194] Due to its high tolerance to oxygen etching AAO makes an ideal material for high aspect ratio etching masks. In 1999, the Masuda group first translated the highly ordered nanochannel structures of AAO into III-V semiconductors (GaAs and InP) by using reactive beam etching (RBE)[191] (Figure 3-4 b). Their group also used oxygen plasma etching to form ordered diamond sub-100 nm anti-dot arrays over 1 cm^2,[188] an area which would be extremely time-consuming to cover by traditional lithography methods (Figure 3-4 c). Nanoporous diamond thin films are promising candidates for future high performance nanocapacitors due to high charge per unit capacitance ratios that exceed those of graphitic carbons.[192]

Tian et al. extended this method to complex oxides field by synthesizing $BiFeO_3$ (BFO) anti-dot arrays.[186] Here thin layers of $SrRuO_3$ (SRO) and $BiFeO_3$ (BFO) were first grown epitaxially on $SrTiO_3$ (STO) by pulsed layer deposition (PLD), then an ultra-thin (aspect ratio < 8) AAO membrane was then transferred to the substrate as a morphology modification mask. Subsequently, the as-prepared sample was etched by an Ar^+ ion beam followed by mechanical removal

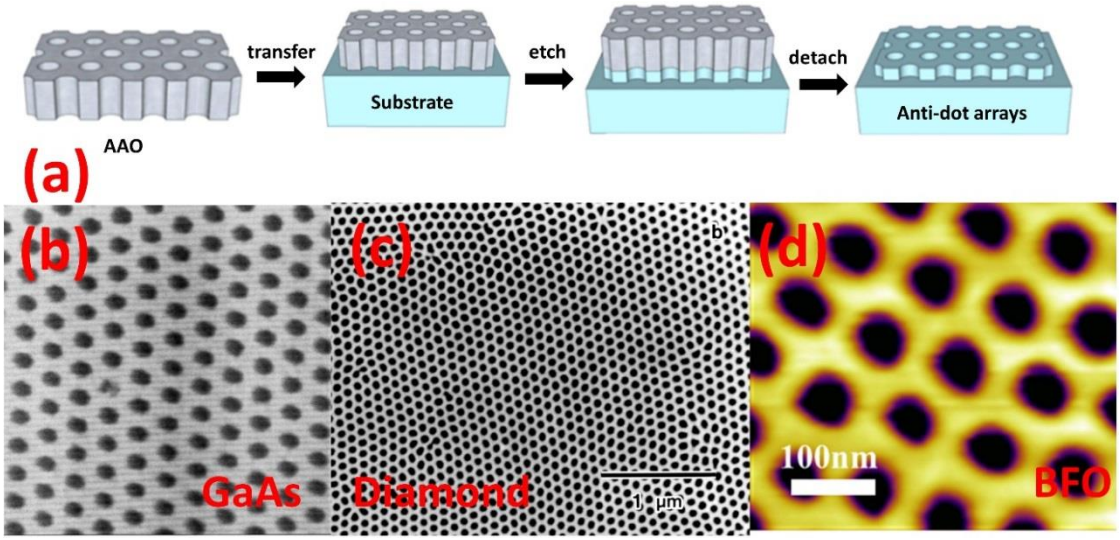

Figure 3-5 (a) schematics of etching method procedure. Reproduced with permission from Ref 30, 2014 American Chemical Society; (b) AFM image of GaAs nanoporous thin film with 60 nm diameter pores from Ref. 191, 1999 IOP Publishing; (c) SEM image of diamond anti-dot arrays from Ref. 188, 2000 Wiley-VCH; (d) Topography of anti-dot BFO arrays. Reproduced with permission from Ref 186, 2016 IOP Publishing.

of the AAO. Variation in the etch duration produced different ordered nanostructure morphologies: nanorings (5 mins), anti-dots (10 mins, Figure 3-4 d[186]), nanochains (20 mins), and nanodots (25 mins). This efficient, precise approach is also exploited in the fields of advanced optoelectronic devices,[193] photonic bandgap waveguides,[187] and anti-reflection coatings.[194] However, as AAO is also removed during the etching process, its pore size is continuously increasing while its thickness is decreasing, thus structural controllability is always

an issue. Overall proper balance between the AAO mask feature size, AAO thickness, and final feature size in the target oxide are all critical to successful anti-dot formation.

3.4.3 Negative Replica Method

A negative replica template is a secondary mold with a nanopillar surface structure that mirrors the original AAO tunnel structure. Polymer solutions with lower surface energy than aluminum oxide tend to spontaneously wet the inner surface of the AAO channels.[105] Thus, high performance polymers are frequently chosen as the secondary mold material since they can be directly injected into template channels to form a negative replica. The desired complex oxide, nitride, or carbide is subsequently deposited evenly on the negative mold surface which forms the duplicate of the original AAO master porous structure. The final template with structures identical to the AAO master is then obtained by selectively removing the secondary mold. Masuda formed functional replica membranes of Pt[104], Au[104], Ni[195], and CdS[195] by injecting PMMA as a sacrificial secondary mold. Nanoporous polymeric replicas can also be obtained by using metallic secondary molds (Figure 3-5).[196,197] The thickness of metallic replicas is limited by the ability to form polymer secondary replicas with high aspect ratios. To address this limitation one innovative study electrochemically deposited the mold materials to the side of AAO instead of infiltrating the secondary mold into the AAO channels, thus providing sufficient mechanical

support to keep the PMMA nanopillars upright. The resulting Ni reverse template achieved a high aspect ratio of 20.

The negative replica synthetic method is amenable to processing an array of commercially available high-performance polymers such as poly (ether- ether-ketone) (PEEK) and poly(tetrafluoroethylene) (PTFE), which are extremely difficult to modify using conventional methods.[126] Pellets of the selected polymer are placed on the top of AAO template and simply melted to infiltrate the AAO pores. As such, virtually all polymer solutions with lower surface energy than aluminum oxide can serve as a negative replica material using the template wetting method. After removing AAO, the polymeric negative replica with reverse AAO nanostructure (positive nanopillars) is subsequently used as a mold to fabricate anti-dot arrays with complex materials (Figure 3-7a). The only disadvantage of this method is that reverse template nanostructures will aggregate into bundles and lose their order (Figure 3-7 inset) when its aspect ratio exceeds 5, due to strong

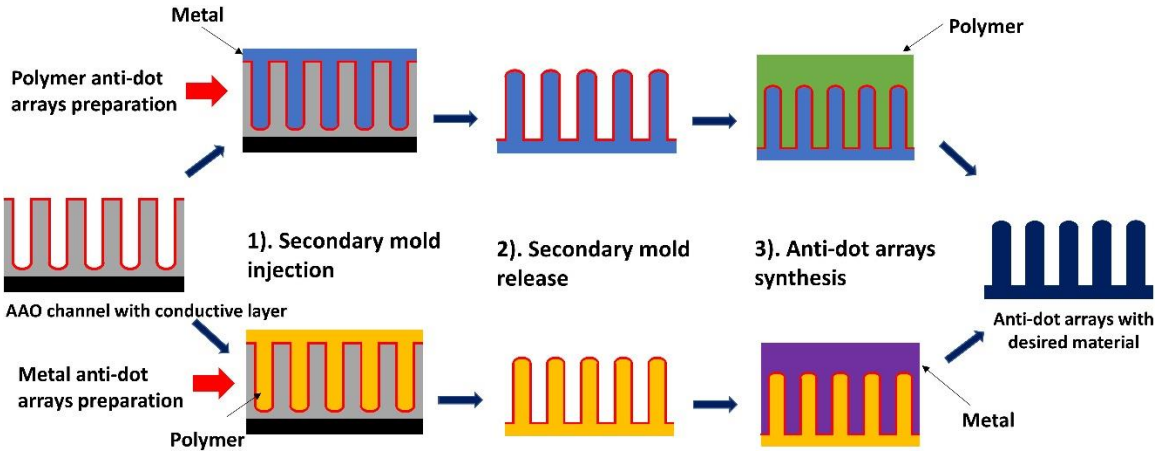

Figure 3-6 Schematics of anti-dot arrays fabrication. Starting material is AAO templates coated with a thin conductive layer. (1) Secondary mold injection. Metal secondary mold can be electro-chemically deposited into channels while polymer mold spontaneously covers the channels. (2) free standing secondary mold is obtained by selective etching of AAO template. (3) Polymer/metal antidot arrays are formed by wetting or electro-chemical deposition respectively.

capillary forces between nanopillars.[198] For example, Martin et al. melted PEEK (aspect ratio < 6) , a highly chemically stable polymer into the original, engineered AAO template at 390°C, then selectively dissolved the aluminum substrate and AAO in an acidic solution of $CuCl_2$ and NaOH 10 wt% respectively, without damaging PEEK nanorod.[198] The self-standing PEEK nanorod template was then taken as a mold for silicon nitride (SiN_x) deposition and thermally removed at 600°C. The resulting SiN_x template perfectly preserved the original AAO

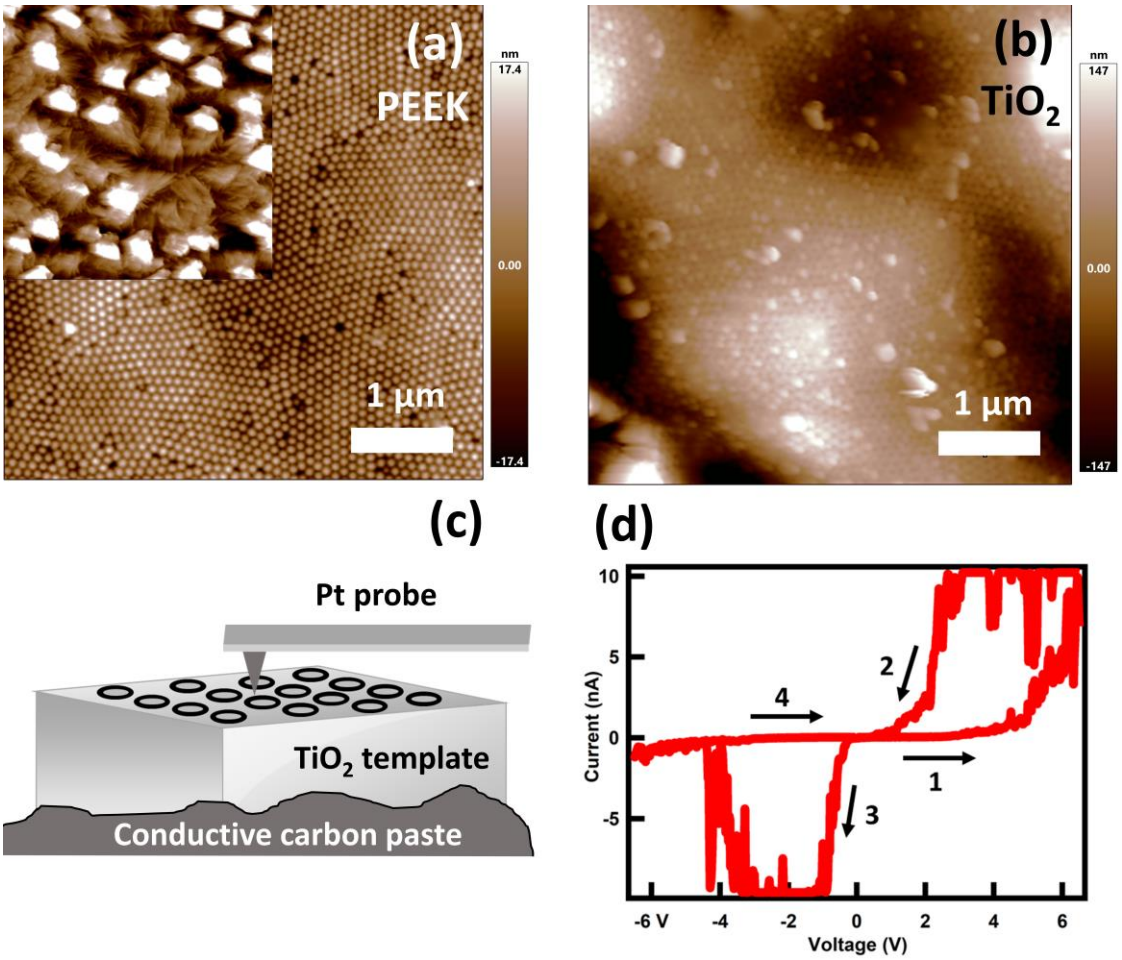

Figure 3-7 (a) AFM image of PEEK nanorod arrays and inset PEEK nanorods aggregate in bundles when aspect ratio exceeds 5; (b) AFM image of TiO_2 nanoporous template synthesized by negative replica method; (c) Schematics of C-AFM testing on TiO_2 anti-dot arrays; (d) Local I-V curve obtained on TiO_2 arrays displays bipolar resistive switching behavior.

template nanoporous network structure. The SiN_x template displayed many superior properties compared to the original AAO master template, including greater high temperature strength, abrasive resistance, and chemical inertness. Our group used the negative replica method to successfully fabricate a 70 nm pore size through-hole continuous TiO_2 anti-dot array, where TiO_2 was sputtered to PEEK nanorod arrays to form a nanoporous structure. The PEEK template was subsequently thermally removed to leave a free-standing TiO_2 anti-dot array (Figure 3-7b). The as deposited nanoporous TiO_2 anti-dot arrays were attached to high temperature resistant conductive carbon paste as substrate to retrain its structure during thermal annealing process (Figure 3-7c). The nanoporous TiO_2 anti-dot array shows bipolar resistive switching under conductive AFM (Figure 3-7d). This method demonstrates its ability to fabricate complex and functional anti-dot arrays and considering the advances of vacuum thin film deposition techniques (sputtering, ALD, PLD), extending the negative replica sequence to materials beyond binary oxides.

While the fabrication of the PEEK nanomold is costly and time-consuming, thermal removal of the final nanoporous template is destructive. To reduce the cost of the precursor wetting method, Martin et al. fabricated an ordered, 120 nm diameter nanopillar array of poly(tetrafluoroethylene) (PTFE) that extended over large (cm^2) areas.[199] The PTFE negative replica was subsequently immersed in a 10 wt.% solution of poly(vinyl alcohol) (PVA), a well-known biocompatible material, and then dried in vacuum to form anti-dot arrays. Since the nanomold is not damaged during the process, the PTFE nanomold could be directly separated from the anti-dot template using tweezers and reused for preparing additional

templates, thus increasing throughput and cost-efficiency. Preserving the original ordered nanoporous structure after removing the AAO master template, however, is still a challenging step in template-directed replica synthesis. Also, while most high-performance polymeric materials are chemically robust, their low thermal stability restricts the overall processing temperature window, which is a significant issue as most complex oxides require high, elevated temperatures to produce the desired (and often functional) phase. Thus, an additional post annealing step is required to functionalize the as-deposited film, which could also potentially damage the nanoporous network.

Another route towards non-destructive replication transferred the AAO nanoporous structure to a silica (SiO_2) template.[200] Here an amine-modified resin was injected into the AAO channels and exposed to UV light (350-400 nm) to form cross-linked polyacrylate nanofibers inside the pores. The nanofiber arrays were then gently separated from the AAO template by attaching to a piston and lifted with a force around 0.4 N at a rate of 0.1 mm/min. The resulting negative polyacrylate replica array was covered with a sol-gel to form porous silica template, which was finally detached from the nanofiber arrays using tweezers. The as-prepared nanofiber arrays perfectly replicated the AAO porous structure up to an aspect ratio of 10; higher aspect ratio structures (~ 30) showed the tendency to bend and agglomerate. This issue can potentially be solved by modifying the AAO template morphology or using higher-strength materials as the negative replica. This non-destructive method enables multiple duplicate templates from a single AAO template by recycling both the AAO template and its negative replica, which greatly reduces cost and labor of the entire process.

3.5 Closing Remarks

Due to the nature of self-organization in nanopore formation, direct anodization is unable to produce an ordered porous structure in complex materials such as carbides, nitrides, or perovskite oxides. With the help of modern fabrication techniques, self-ordered nanoporous templates have been utilized to bridge the gap between anodized templates and patterned complex materials. 20 nm and 100 nm diameter memristive HfO_2 nanocapacitors are synthesized with the help of ultrathin AAO template and exhibit size effect. This chapter also surveyed a selection of direct anodization of binary metal oxides templates and templated assisted fabrication of functional porous templates using methods ranging from ion etching to reverse template replication. As an example, TiO_2 nanoporous arrays are fabricated AAO negative replica method using PEEK as a mold. The obtained ATO template showed resistive switching behavior under C-AFM I-V measurements. Continued improvement in deposition techniques and lab facilities will spawn future synthetic routes towards facile fabrication of complex material templates with flexible dimensions to potentially serve as matrices for advanced nanocomposites to be filled with complementary materials pairings to produce enhanced electrical, electrochemical, ferroic, biological, and optoelectronic properties and functionality.

CHAPTER 4

SOLUTION-PROCESSED MEMRISTOR

4.1 Zero-Dimensional Nanocrystals and Functionalization

Resistive switching behavior has been observed in numerous materials including transitional metal oxides[40,41,201], nitrides[202] and complex metal oxides such as perovskites[88,203]. Most MIM memristors are 1D resistive switching materials such as binary oxide nanowires[204,205] ,individual perovskite nanotubes[206] and vertically aligned carbon nanotubes[207], or 2D thin films[208,209], which commonly evolve expensive top-down and UHV fabrication techniques. These conventional fabrication approaches have limited potentials on next-generation device due to its expensive fabrication equipment and relatively small deposition area[25]. A promising alternative is the zero-dimensional nanocrystal (NC) solution-processed technique. Zero-dimensional (0D) nanostructures attracted much attentions over the last decade in the field of resistive switching[210–212]. For example, studies demonstrated solution-processed 10 nm Ag_2Se nanoparticle RRAM[213] device shows bipolar switching characteristics with low power consumption (< 1.5 V) and high reliability (retention > 10^5 cycles). Simon et al. synthesized 80-150 nm TiO_2 nanoparticles showed both bipolar switching and complementary switching behavior[214]. Complementary resistive switching is a newly introduced state which exhibits high overall resistance which effectively suppresses leakage current[31]. While in

contrast, conventional atomic layer deposition (ALD) grown TiO_2 layer only shows standard bipolar switching behavior under the same condition. However, studies and applications addressing quasi-zero-dimensional nanostructure are still scarce, mainly due to difficulties of patterning ordered architectures during fabrication, which is a prerequisite in modern memory devices.

4.2 Synthesis of Nanocrystals

Metal oxides nanocrystals in this study are synthesized via a microwave-assisted solvothermal method, which is a popular chemical synthesis approach producing highly homogeneous and mono-dispersed nanoparticles. Solvothermal method usually grows single crystal nanocrystals under high temperature in organic solvents such as methanol[215], 1,4 butanol[216], toluene[217] within or on the surface of a substance.[218] The crystalline structure formation is performed in a sealed steel autoclave under supercritical pressure in order to achieve the temperature above solvent boiling point. Solvothermal approach enables the high controllability over nanoparticle shape, size, interparticle distance. An additional thermal treatment is necessary for the final product to ensure nanoparticle crystallinity.[219] Solvothermal method offers better overall crystalline quality as compared to widely used sol-gel method due to its amorphous nature.[217]

4.3 Fabrication of Solution-processed Memristor

Various fabrication techniques have been developed which allows solution-processed multi-component patterning including dip-pen nanolithography (DPN)[220–222], wet stamping[223] and spin coating[224]. However, these techniques have the drawbacks such as long deposition times, low controllability, or requiring complicated setups. Kim et al. proposed a facile and high-productive flow coating technique, which is a dynamic self-assembly method functionalizes nanoparticles by patterning monodisperse, highly crystalline inorganic zero-dimensional nanocrystals into ordered structures over large areas[225–228]. In the flow coating process, a razor blade is held at a fixed height (usually < 0.5 mm) above a rigid substrate, which is affixed and moved in a 'stop-and-go' motion by a programmable nanopositioner. The NC solution (usually a few μl) is subsequently injected between razor blade and substrate using a micropipette. The solution remains confined between razor blade and substrate due to capillary forces. Nanoribbon height and width dimensions are mainly determined by nanopositioner stopping time (t_d), moving distance d and substrate moving speed v. Flow coating technique exhibits excellent controllability over nanoparticle assemblies at nanometer scale heights, micrometer scale width and flexible scale in length (depending on blade length and solution amount), which is a perfect candidate for functionalizing zero-dimensional complex oxides nanoparticles.

4.4 Advantages of Solution-processed Memristor

Solution-processed RRAM device overcomes three major limitations that hindering the application of conventional vacuum-deposited devices: (1) Complicated fabrication process. All physical deposition methods require high vacuum and high temperature. Most modern vacuum deposition instruments also require clean room working environment. (2) Low productivity. Deposition rate is usually low due to the nature of vacuum deposition. (3) Inflexible. the brittle and rigid natures of ceramic films which greatly limit their application in next-generation devices where flexibility is required, such as wearable electronics.

Wang et al. firstly demonstrated the resistive switching behavior in nanoribbons comprising solution-processed strontium titanite nanocrystal (STONC) linked by oleic acid ligands, which exhibits up to 10^4 switching on/off ratio (HRS resistance/LRS resistance) and no obvious retention loss after 1000 cycles[227]. One key advantage of STONC nanoribbon is the structure can be release into liquid and redeposit to an arbitrary substrate without losing its original structure and functionality (Figure 5a). Figure 5b shows the local I-V testing on one bent STONC nanoribbon deposited on Pd/PET substrate. The calculated strain is 3% induced by placing a steel rod underneath the ribbon. The collected I-V curves preserve the identical response and curve fitting, indicating the same conduction mechanism in the process. The mechanical reliability of nanoribbon shows substantial promise in the application of future flexible and printable electronic elements[26].

4.5 The Impact of Ligands in Solution-processed Memristors

In addition, Wang *et al.* also investigated the effect of ligand on the memristive behavior by local conductive testing after annealing the nanoribbons at 500°C for 2 mins. As the annealing step removed the presence of ligands, the HRS conductive mechanism switched from trap-assisted tunneling (TAT) to the behavior of Fowler-Nordheim tunneling[229]. This interesting phenomenon confirms that ligands play an important role of reducing current, which might be a breakthrough for next-generation low power consumption memory devices. However, there are only a few studies realized and addressed this profound ligand-mediated interparticle effect which concluded carrier mobilities decrease with increasing ligand length[230,231].

Subsequently, another work has been done determining resistive switching character of nanoribbon comprising hafnia (HfO_2) nanocrystals with different organic capping layer, oleic acid (HfO_2-O), dodecanoic acid (HfO_2-D) and undecanoic acid (HfO_2-U)[226]. To better evaluate the impact of ligand length on switching behavior, the interparticle distances have been estimated based on covalent chain length: HfO_2-U (1.44 nm), HfO_2-D (1.57 nm) and HfO_2-O (2.2 nm). Figure 6 presents SET and RESET voltages for three HfO_2 systems. It clearly shows that SET voltages increase with ligand length. RESET voltages exhibit similar relationship but with less dependence on ligand length. Since the experimental condition such as AFM tip, nanocrystal type and size are kept the same, we posit that resistive switching operating voltage increases with ligand length.

4.6 Summary

In summary, I reviewed the recent studies functionalizing zero-dimensional nanocrystals utilizing solution-processed flow coating techniques to investigate the resistive switching properties. Most studies that have been done are limited to densely packed 1D and 2D nanostructures. Whereas the investigation of resistive switching mechanism between nanoparticles, particularly the effect of chemical ligands, is still in preliminary stage. Utilizing the cost-effective flow coating technique, previous studies demonstrated the possibilities of reveal the relationship between resistive switching operating voltage and chemical ligand length. However, only three types of ligands capped in one particular oxide has been thoroughly studied. In-depth studies such as nanoparticle surface area size effect and structural effects are still waiting to be explored.

CHAPTER 5

PHOSPHONIC ACID LIGANDS FOR NANOCRYSTAL SURFACE FUNCTIONALIZATION SOLUTION-PROCESSED MEMRISTORS

5.1 Introduction

Surface engineering of colloidal nanocrystals (NCs) is a prerequisite for advanced applications such as solar cells,[232,233] thermoelectrics,[234] field effect transistors,[235] smart windows,[236] superconductors,[237,238] catalysis,[239] and memristors.[226] Modern threshold memristive devices garner intense research interest due to their ability to emulate synaptic responses in neuromorphic computing and logic gate applications.[240] Threshold switching is a reversible volatile process where upon the application of an applied bias generates current flow and a significant amount of internal Joule heating,[54] which once above the metal-insulator-transition,[241,242] rapidly activates the device and maintains a low resistance state (LRS) until the voltage is removed and resets to an insulating high resistance state (HRS). Threshold logic memristors exhibit faster switching speeds, lower power consumption, higher scalability, and greater 3D stackability than standard complementary metal-oxide-semiconductor (CMOS) circuits, thus promoting further miniaturizing for next-generation neuromorphic computing components that extend beyond Moore's Law. [2,243] These nascent computing applications require large crossbar device arrays to operate, where threshold selector devices are used to suppress sneak currents between neighboring cells.[244]

5.2 Motivations

Memristors typically possess a metal-insulator-metal (MIM) structure comprising an insulating oxide sandwiched between two metal electrodes fabricated by top-down, ultra-high vacuum (UHV) thin film deposition processes. These conventional fabrication approaches are limited due to expensive fabrication equipment and small deposition areas.[25] A burgeoning alternative is the deposition of monodisperse, highly crystalline inorganic nanocrystals using solution-processed flow coating,[228] a facile and cost-effective approach which enables controlled formation of thin-film transistors and highly scalable nanostructure arrays for future flexible large-area electronics.[245] In addition, conductive atomic force microscopy (C-AFM) has the ability to locally interrogate electrical properties across length scales (a few nanometers to 100 μm) relevant to both individual NCs and the nanoribbon assemblies. We used c-AFM analysis to show that operating parameters such as set/reset voltage and LRS/HRS ratios of the nanoribbons inversely scale with the length of the ligand used to stabilize the NCs in solution.

Recent studies demonstrated tailorable resistive switching behavior within individual solution-processed comprising single-crystalline strontium titanate nanocubes (STONCs) upon transfer from the original hard substrate to metallized flexible polymeric substrate.[227] Subsequent studies showed that operating parameters such as set/reset voltage, and LRS/HRS ratios inversely scaled with increasing ligand length in solution-processed hafnium oxide (HfO_2)

nanoribbons.[226] Since lower set/reset voltage means lower data read/write voltage and hence leads to lower overall device energy consumption, shorter ligands are always desired. However, ligands shorter than dodecanoic acid result in unstable dispersions, thereby restraining the minimum set voltage that could be used to switch the ribbons of NCs.[225] In general, phosphonic acids are more expensive and less commercialized. We chose phosphonic acid over previously used carboxylic acid because phosphonic acid have a much higher binding affinity, which enables us to stabilize shorter ligands on nanocrystal surface. It is reported that long-range charge carrier mobility in nanocrystal systems is mainly nearest-neighbor hopping, which is inversely scales with capping ligand length.[230] Here we expand the investigation of ligand chemistry on memristive behavior to include the evolution of threshold properties of HfO_2 nanoribbons over a series of five phosphonic ligand capping layers. Use of 2-ethylhexyl phosphonic acid produces a high dispersible system and an ultrashort ligand length that results in a record-low operating voltage, thus exhibiting enormous promise for future flexible electronics due to reduced waste heat and lower energy consumption.

5.3 Experimental Methods

Here, we explored the functionalization of NCs with phosphonic acid derivatives **1–5** (Scheme 1) and their fabrication into memristor devices. We

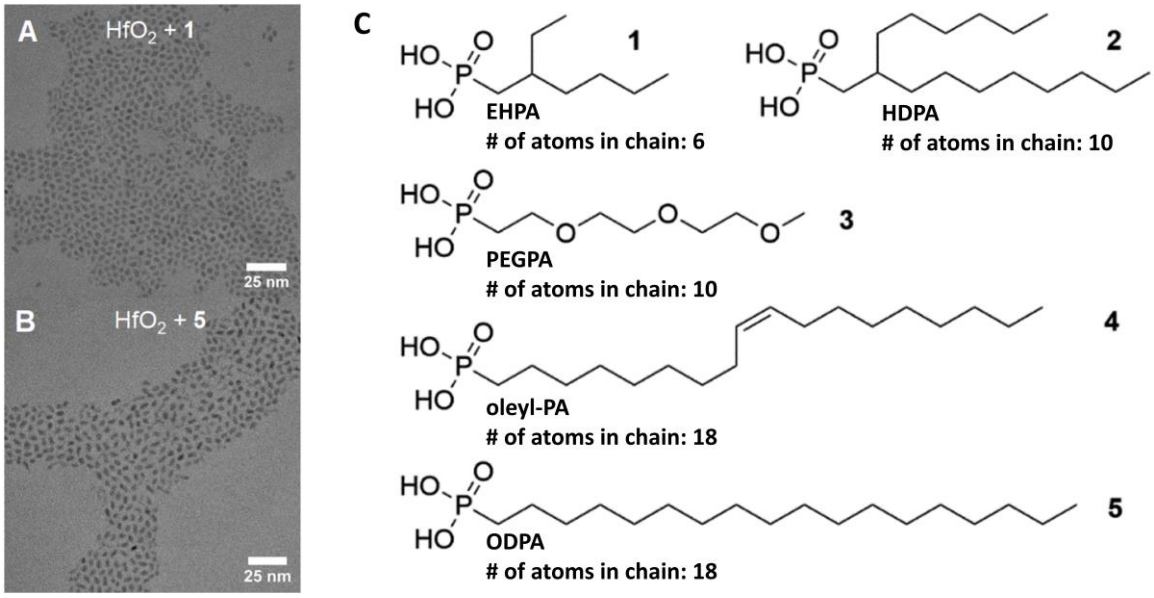

Figure 5-1 (A) TEM image of HfO2 NCs functionalized with 1. (B) TEM image of HfO2 NCs functionalized with 5. (C) Schematics of target phosphonic acid ligands.

selected novel, branched phosphonic acids (**1** and **2**), a versatile polyethylene glycol[246–248] derivative (**3**), yet unreported oleyl phosphonic acid (**4**), and a prototypical straight chain derivative (**5**). The convenient synthesis of these phosphonic acids is followed by surface functionalization methods that are facile, even for the branched substrates. Finally, using these ligands, we deposit HfO2 NCs into ribbons of NCs by a simple flow coating process and measure their local memristive current–voltage response with c-AFM.

All nanocrystal capped with five ligands fabrications, nuclear magnetic resonance spectroscopy (NMR), X-ray powder diffraction (XRD) and transmission electron microscopy (TEM) characterizations are accomplished by our collaborator in Columbia University, Ghent University, University of Basel. Ligands 1– 5 are utilized to prepare memristors based on hafnium oxide NCs. HfO2 NCs (d = 3.75 nm, Figure 7a and 7b) are synthesized in benzyl alcohol from

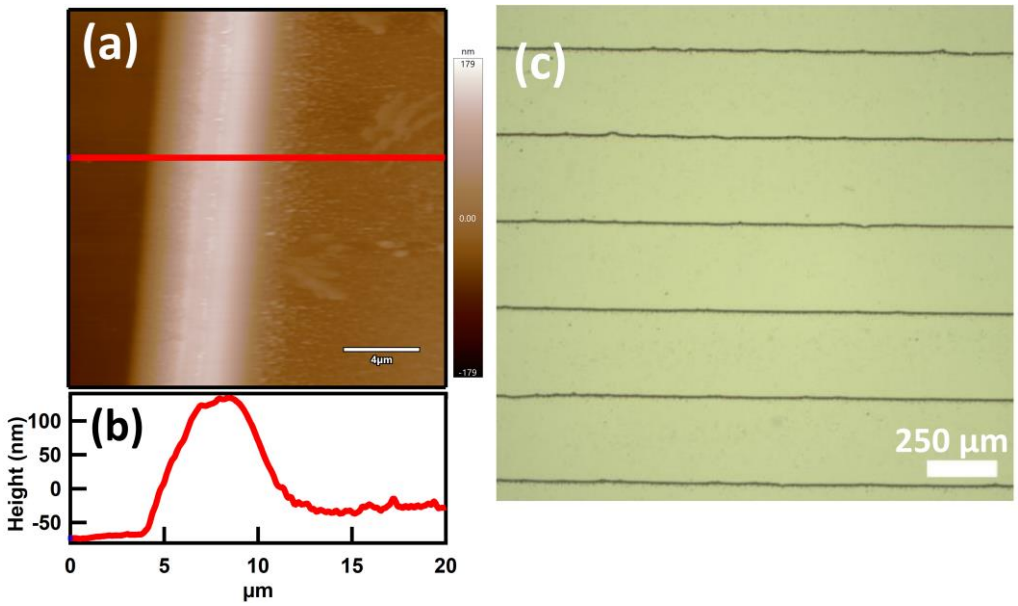

Figure 5-2 (a) AFM topographic image of HfO_2 nanoribbon. (b) AFM height profile image of HfO_2 nanoribbon. (c) Optical microscope image of HfO_2 nanoribbons.

hafnium (IV) tert-butoxide.[242] Flow coating technique was used to synthesize HfO_2 nanoribbons. A 15 mm razor blade edge was aligned parallel to the Ti/Pt-coated Si substrate at the height of 0.1-0.3 mm. 10 μL HfO_2 NC solution was injected between razor blade and substrate using a micropipette. The solution remains confined between razor blade and substrate due to capillary forces. The substrate movement was subsequently controlled by a programmable nanopositioner (Burleigh Inchworm controller 8200). The parameters in the study were as follows: solution concentration = 1mg/ml, stopping time t_d = 2000 ms, moving distance d = 200 μm and blade speed v= 1500 μm/s. HfO_2 nanoribbons were deposited on a silicon wafer (undoped ⟨100⟩, University Wafer Inc.) coated with 15 nm thick Pt thin film serves as bottom electrode. Prior to use, blades and substrates were washed in soap water, distilled water, isopropyl alcohol, toluene and blow-dried with filtered N_2 gas. Nanoribbons were made by same flow coating

technique with the height ranging from 100-200 nm and width of ~ 8 nm. All five types of nanoribbons with different ligands had similar geometric profile.

The local conductive measurement was performed on an AFM (Cypher ES ORCA, Asylum) at room temperature. A Pt tip (25Pt400B, Rocky mountain Nanotechnology) with the frequency of 10 kHz was used. The bottom electrode (Pt thin film) was pasted by silver paint (Ted Pella) to a conductive sample holder connected to AFM to form an electric circuit. The sample was biased from bottom electrode (up to ±10 V) by AFM while the tip was kept at 0 V during testing. All measurements started at 0 V and followed by a positive voltage sweep through the set process, back through and continue through the negative voltage region. I-V curves were collected at positions of equivalent thickness on each ribbon at a sample rate of 2 kHz.

5.4 Results and Analysis

40 individual I-V curves were collected over four separate, individual nanoribbons for each type of ligand. All five nanoribbons showed threshold switching behavior. It should be noticed that as we gained more insights on ligand structure, it became obvious that ligands are not extending out as a straight chain. Instead, the chains are reaching out zig zag with an angle around 109°. Therefore, given that the C-C bond distance is usually 140 pm, the best estimation of the chain length is:

$$\text{ligand length} \approx n \times \cos\left(\frac{180° - 109°}{2}\right) \times 140\ pm \qquad (1)$$

where n is the number of atoms in the longest chain. But it is still rather inaccurate to direct calculate ligand length according to the atom numbers. Thus, instead of estimating the ligand length, we proposed to use the number of carbons in the longest chain of the ligand.

As shown in Figure 9, we observed the expected trend where operating voltage scales with ligand size. Here, the set voltage varies from extremely high (4.4 ± 0.7 V) for ligands **4** and **5** to a -low (1.0 ± 0.3 V) for ligand **1**. It was previously demonstrated that the minimum threshold switching voltage of 1.2 ± 0.3 V using the mixture of dodecanoic acid and 10-undecenoic acid as ligands adsorbed on the HfO_2 NCs.[226] Although carboxylic acid have a reasonable high affinity for metal oxides[249,250], ligands shorter than dodecanoic acid results in unstable dispersions and thus hindering further reducing threshold switching voltage. The use of 2-ethylhexyl phosphonic acid ligand **1**, combining a high colloidal stability with a compact ligand shell, results in a record-low threshold switching voltage of 1.0 ± 0.3 V, which is promising for next-generation flexible and wearable electronic devices.

Note that ligand 3 violates the trend and displays higher set voltages than expected for its ligand length. This may be caused by the presence of the free ligand (which proved difficult to remove from the nanocrystals as described above) or by the nature of the polyethylene glycol chain. Note that the triangular cross-section of the nanoribbons creates a thickness-dependence in the memristive response. The thickest portion of the nanoribbons is difficult to electroform using the ±10 V bias supply of the microscope. Therefore, we performed all conductive probe

measurements in thinner areas of equivalent thickness (~80 nm) for each nanoribbon tested.

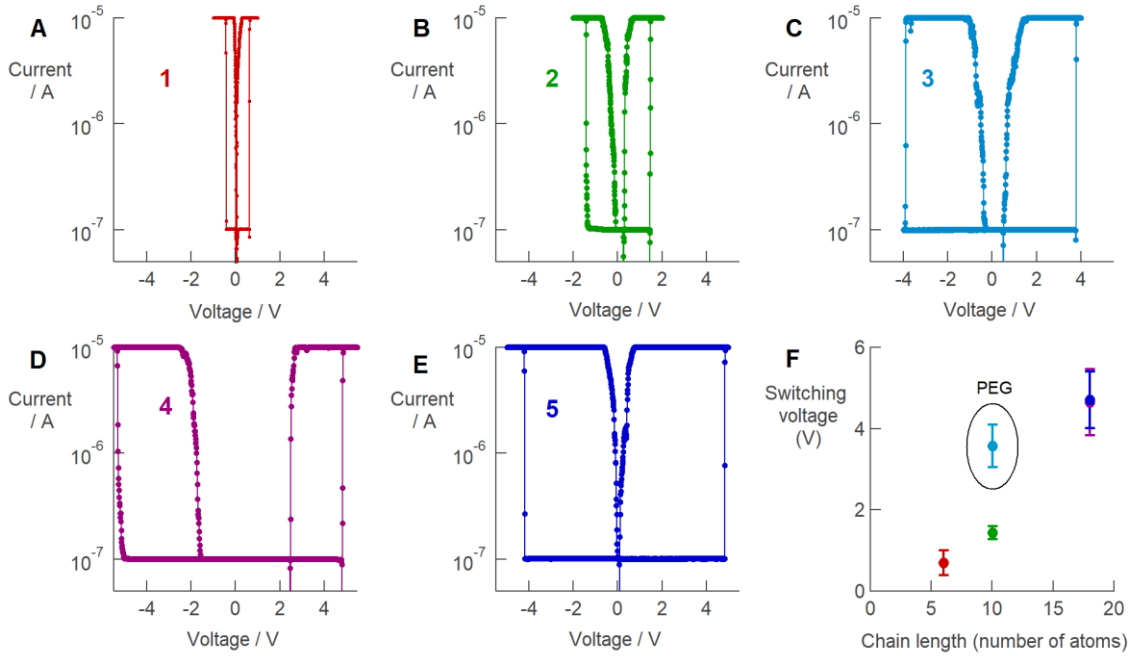

Figure 5-3 (A–E) I–V curve of the threshold switching ofHfO2 nanoribbons using 1–5, respectively, as ligand. (F) Switching voltage in function of the ligand chain length.

5.5 Local Resistive Switching Thickness Dependency

Since all nanoribbons have cylindrical profiles as shown in Figure 8a and 8b, it is important to clarify that different switching voltages are not the results of local I-V measurements height variations. Therefore, an independent study about resistive switching thickness dependency on HfO_2 nanoribbons has been carried out. I-V curve sweeps with the voltage amplitude of 4 V were done on three different locations on nanoribbon with relative thickness of 80 nm, 140 nm and 200 nm as shown in Figure 9a and 9b. At 80 nm location (Figure 9c), conductive

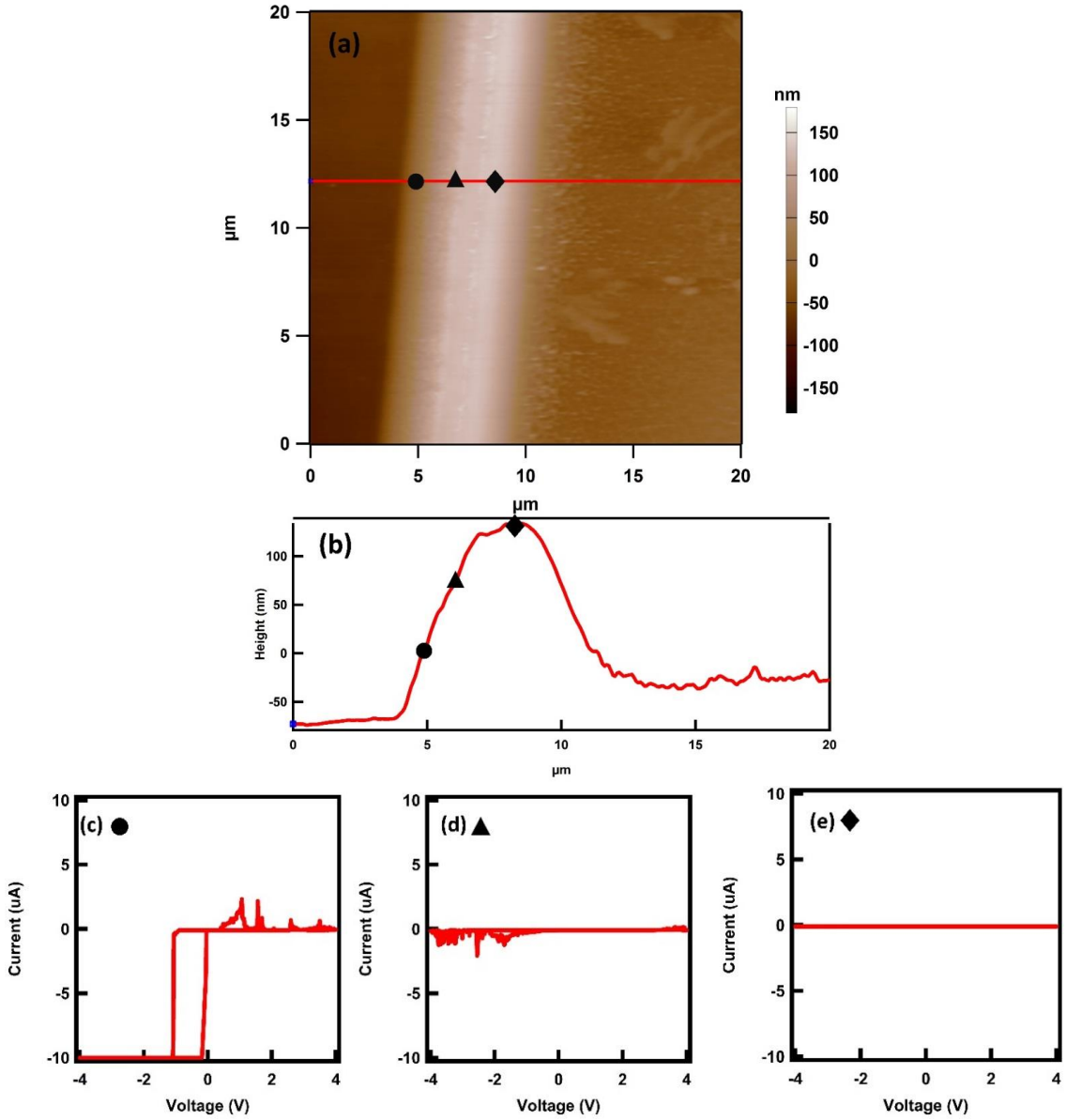

Figure 5-4 Thickness dependence study of HfO_2 with ligand 3. (a) 20 µm × 20 µm AFM scan of nanoribbon and (b) sectional height image along the red line. (●), (▲) and (◆) indicate three local c-AFM tests with thin (~80 nm), medium (~140 nm) and thick (~200 nm) thickness. (c)-(e) are the corresponding I-V responses of the first voltage sweeping (±4V). The electroforming step showed dependence on nanoribbon vertical thickness. Ref 9. SI also has similar study on HfO2 nanoribbon thickness dependent measurement.

filament was successfully formed as demonstrated by a sudden current increase around -1.1 V. At 140 nm location (Figure 9d), some current variations were

observed but clearly no strong conductive filament was constructed. At 200 nm location (Figure 9e), there was no current response at all as compared to the previous two measurements. This interesting phenomenon could be explained by the formation and rupture theory of conductive filament. During electrical forming stage, the newly created conductive filament must extend from one electrode to the opposite electrode. While in set/reset processes, conductive filament only ruptures at its thinnest area which is usually less than a few nm.[30,54] Therefore, there is strong thickness dependency in electro-forming step.

5.6 Summary

We developed a scalable synthesis of new phosphonic acid surfactant ligands. We subsequently showed their superiority in functionalizing nanocrystal surfaces. Using a flow coating technique, we fabricated nanoribbons comprising HfO_2 nanocrystals capped with five types of phosphonic acid ligands. Threshold switching operating voltages of five ligands were statistically determined by c-AFM. 2-ethylhexyl phosphonic acid leads to a record-low operating voltage in the resistive switching of HfO2 NC assemblies. We observed the nanoribbon operating voltages inversely scale with the length of the ligands. Since phosphonic acid has higher bind affinity, shorter ligand **1** is successfully obtained and leads to a record-low operating voltage among all resistive switching of HfO_2 nanocrystal assemblies. The results are consistent with the previous measurements on HfO_2 nanocrystals stabilized by carboxylic acid ligands, which validates the performance of the fabrication technique and characterization method. Considering their high binding

affinity, we expect the synthesized ligands to be heavily used to functionalize surfaces, even beyond the nanocrystal field.

CHAPTER 6

SOLUTION-PROCESSED MEMRISTIVE ASSEMBLIES COMPRISING POLYDISPERSE NANOCRYSTALS

6.1 Introduction

Resistive switching behavior has been observed in numerous materials including transitional metal oxides[40,41,201], nitrides[202] and complex metal oxides such as perovskites[88,203]. The majority of memristive systems, such as 2D thin films [208,209], 1D nanowires[204,205], nanotubes [207,251], and nanodots utilize expensive, UHV-based fabrication approaches that require long deposition times. Sol-gel spin-coated ZnO thin films[36] and hydrothermally prepared TiO_2 thin films[252] represent two examples of inexpensive, high-yield alternative fabrication processes reported in the last decade. More recently solution-processed fabrication of zero-dimensional nanocrystals (NC), have garnered significant research focus as materials in memristive or resistive switching applications [210–212]. Various fabrication techniques have previously been developed to enable solution-processed multi-component patterning, including dip-pen nanolithography[220–222], wet stamping[223], and spin coating[224]. These techniques, however, require complicated, time-consuming procedures and offer low controllability over material microstructures. Kim et al. proposed a facile and high-productive flow coating technique, which is a dynamic,

self-assembly method that patterns monodisperse, highly crystalline inorganic zero-dimensional nanocrystals into ordered assemblies over large areas[225–228].

We recently demonstrated a memristive and tailorable nanoribbon comprising single-crystalline strontium titanate nanocubes (STONC) capped with oleic acid ligands.[227] The as-fabricated nanoribbons were capable of being transferred to a second, arbitrary substrate with a different metallized surface as a result of the robust mechanical properties of the nanoribbon. Motivated by potential ligand chemistry effects, a follow-up study showed that operating parameters such as set/reset voltage, and LRS/HRS ratios inversely scaled with increasing ligand length in solution-processed hafnium oxide (HfO_2) nanoribbons.[226] Since lower set/reset voltage leads to lower overall device energy consumption, the observed trend suggested that shorter ligands were optimal. Subsequently, a phosphonic acid ligand library was developed to replace previously used carboxylic acids. Phosphonic acids possess a higher binding affinity which enables the functionalization of shorter ligands to decrease the interparticle core-core distance and increase the tunneling probability.[253][230] The use of 2-ethylhexyl phosphonic acid produces a high dispersible system and an ultrathin ligand shell that results in a record-low threshold voltage in a solution-processed memristor, thus exhibiting enormous promise for future flexible electronics due to reduced waste heat and lower energy consumption.

In this work, we extend our scope to include the study of resistive switching behavior in nanoribbons comprising mixtures of monodisperse and polydisperse barium zirconate ($BaZrO_3$; BZO) and strontium zirconate ($SrZrO_3$; SZO) perovskite nanocrystals capped with phosphonic acid ligands. The limited number

of studies of resistive switching behavior within BZO and SZO have been restricted to thin film systems.[254–256] Jo et al. observed the transformation from bipolar

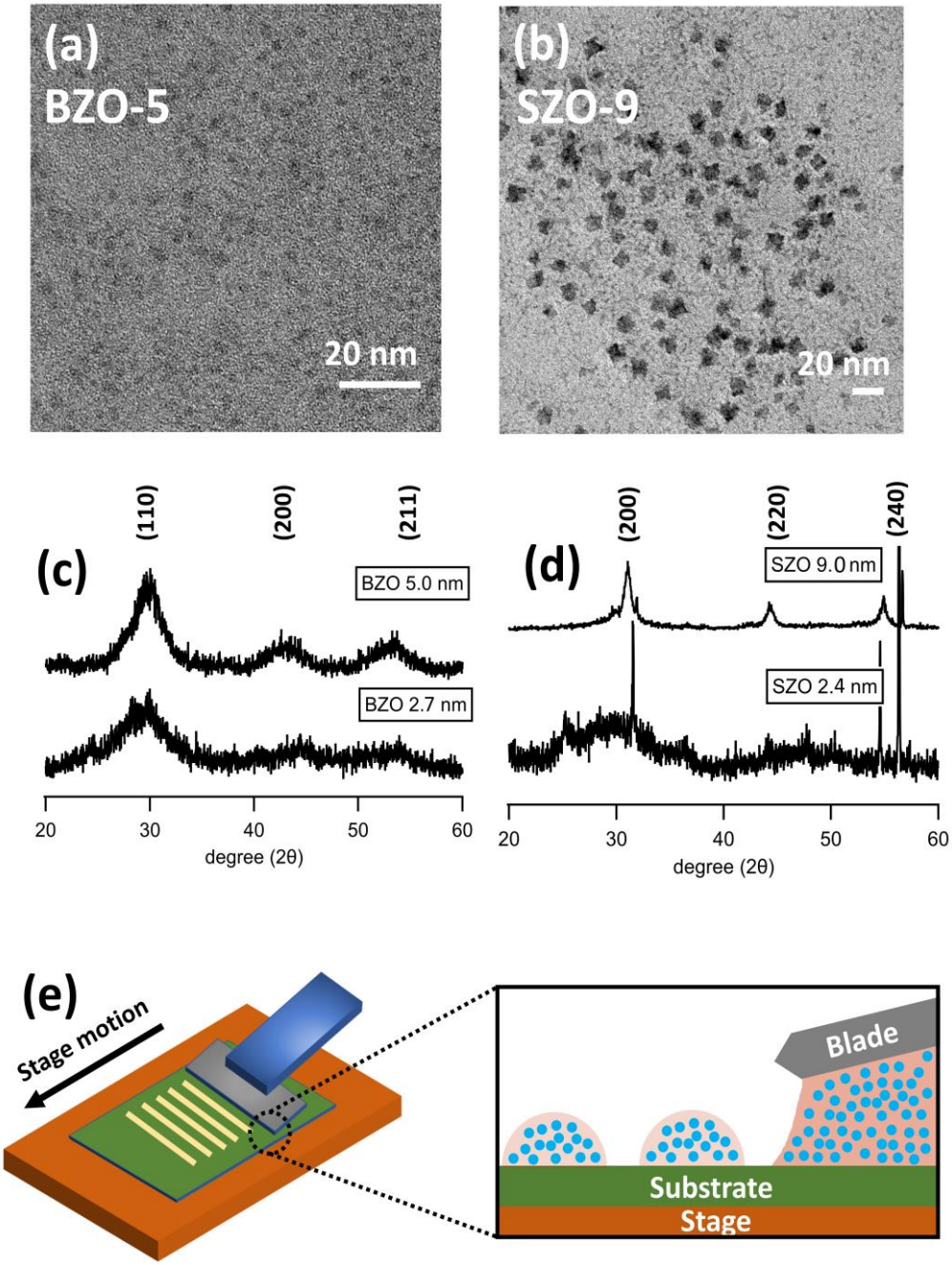

Figure 6-1 (a) and (b), TEM images of BZO-5 and SZO-9 nanocrystals. (c) and (d), XRD analysis of BZO and SZO nanocrystals. (e) Schematics of flow coat process.

to unipolar switching in a $SrRuO_3$/Cr:SZO/Pt stack induced by a high substrate temperature caused by Joule heating.[257] Both resistive switching behavior and

the switchable diode effect have also been reported in Ag/$BaZrO_3$/$SrRuO_3$ multilayers.[47] All reported BZO and SZO systems have been grown by vacuum deposition techniques. Here we use a low-cost flow coating method to assemble BZO and SZO nanoparticles into highly ordered nanoribbons. Moreover, we demonstrate the impact of nanoparticle size and polydispersity, as well as A-site substitutional effects on resistive switching operating voltages by studying assemblies comprising various diameters of BZO (2.7 nm and 5 nm) and SZO (2.4 nm and 9 nm) nanoparticles.

6.2 Experimental Methods

6.2.1 Sample Fabrication Methods

Barium isopoxide, strontium isopropoxide and zirconium isopopoxide (Alfa Aesar, > 98%): potassium hydroxide (Sigma Aldrich, ≥85%), ethanol (Acros Organics, 99.5%) , toluene (>99%, Acros Organics) and 2-[2-(2-Methoxyethoxy)ethoxy]acetic acid (Sigma Aldrich, technical) were used without further purification. (2-hexyldecyl) phosphonic acid (HDPA) was synthetized according to De Roo et al.[225]

Double metal oxide nanocrystals with composition $BaZrO_3$ (BZO) and SrZrO3 (SZO) were synthetized via a microwave-assisted solvothermal method. Custom bimetallic precursors are prepared from commercial individual isopopoxides metal sources via alcohol thermal exchange. The resulting materials are subjected to a thermal process in a CEM Discovery SP microwave (max. output

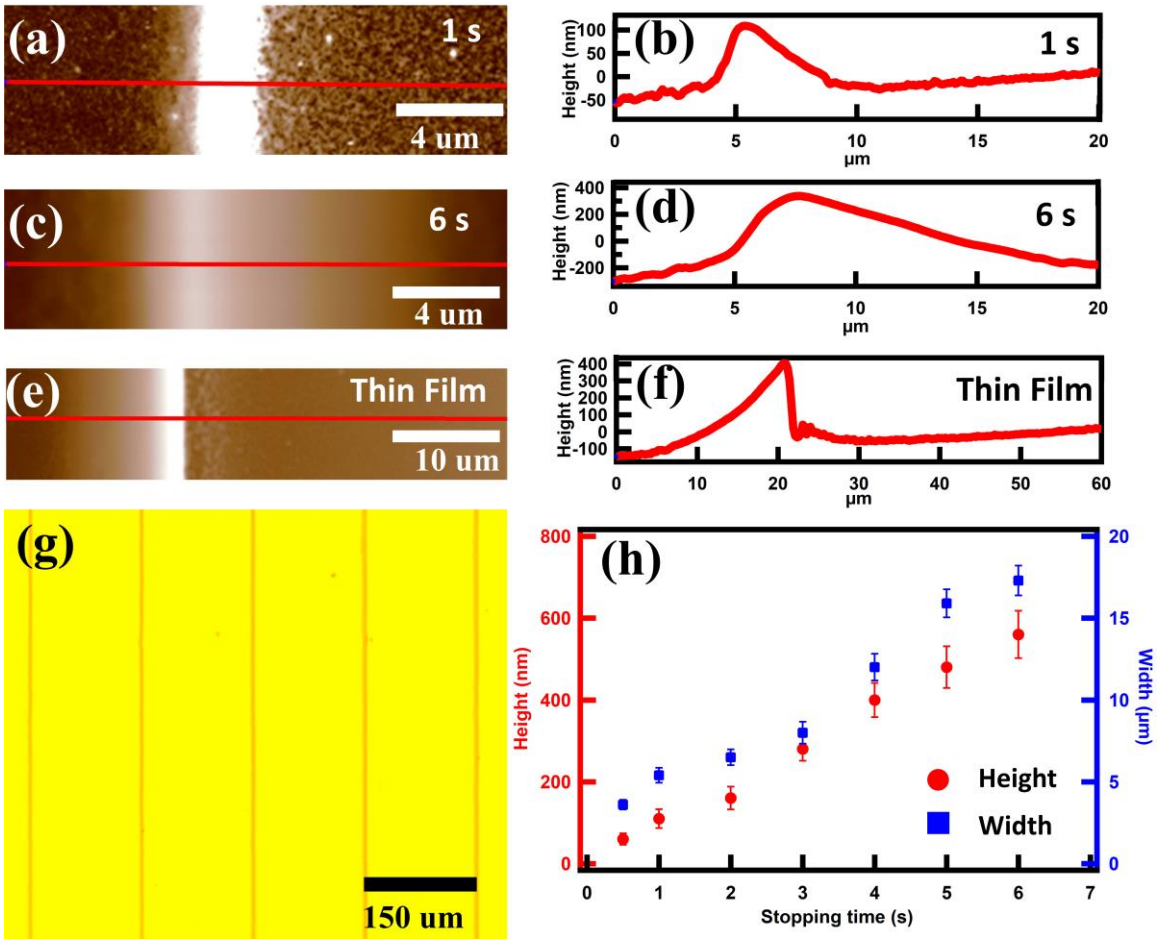

Figure 6-2 (a), (c) and (e), AFM topography and profile images for 1 s stopping time nanoribbon, 6 s stopping time nanoribbon and continuous thin film and (b), (d) and (f) corresponding AFM profile images. (g) Optical microscope image of BZO nanoribbons. (h) Height and width versus stopping time of flow coat process.

300 W) equipment. Samples are prepared by dissolving the bimetallic precursors (0.2 g, 0.30 mmol ($BaZrOR_6$) and 0.31 mmol ($SrZrOR_6$)) in a basic KOH ethanol solution (4 mL). The thermal process includes a plateau for 30 minutes. The main parameters optimized in order to obtain the desired final crystallite size are the base concentration and the set temperature. Recovered nanosuspensions are washed three times with acetone and centrifuged at 5000 rpm for 2 min. SZO nanopowders can then be stabilized directly in (2-hexyldecyl) phosphonic acid (HDPA) acid in toluene. An excess amount of ligand and the use of ultrasounds is

employed in order to ensure a good dispersibility. The excess can then be removed by successively precipitating the particles with acetone and redispersing the solid in toluene. BZO on the other hand, required a pre-stabilization in other family of ligands (acids) and then a ligand exchange. The BZO nanocrystals are stabilized in 2-[2-(2-Methoxyethoxy) ethoxy] acetic acid) with methanol as solvent. The exchange is performed by dropwise adding a solution of a HDPA-toluene solution, with the result of the precipitation of the particles. The solid is recovered by centrifugation and redispersed in toluene. Further purification is done until no MEEAA 1H-NMR peaks are observed. Figure 6-1 (a) and (b) present TEM images of 5 nm BZO and 9 nm SZO nanocrystals.

The XRD pattern of BZO and SZO nanocrystals are shown in Figure 6-1 (c) and (d). All the peaks indexed are in line with cubic phase $BaZrO_3$ and $SrZrO_3$ reported in Ref. 258 and 259. [258,259]Sample substrate was silicon wafer (University Wafer, <100>, 500 um thickness) coated with 5 nm Ti and 35 nm Pt by thermal evaporator (CHA SE-600) to serve as sample bottom electrode. The flow-coating process was conducted in a homemade setup that consists of a razor blade and substrate which was attached to a computer-controlled nanopositioner (Burleigh Inchworm controller 8200). During fabrication 3~5 μL of the nanoparticle containing solution was injected in between the blade and the substrate and was confined due to capillary forces. The nanopositioner is programed to move in a 'stop-and-go' motion, where the stopping time (t_d), step size (d), and substrate moving velocity (v) dictate the overall nanoribbon microstructure as shown in Figure 6-1 (e). Nanopositioner motion can also be set with a slower moving speed and no stopping time to flow coat thin film structure.

The film thickness depends on the substrate moving velocity and the nanoparticle solution concentration. A pronounced, quasi-nanoribbon structure is formed at the edge of thin film due to the initial solution injection in between the blade and substrate.

Table 6-1 Threshold switching operating voltages of BZO and SZO nanocrystal assemblies.

Threshold Switching	
Material	**Threshold Voltage (V)**
BZO-2.7	1.39 ± 0.19
BZO-2.7/BZO-5	1.37 ± 0.22
SZO-2.4	1.53 ± 0.16
SZO-2.4/SZO-9	1.71 ± 0.16
SZO-9	4.18 ± 1.03
BZO-2.7/SZO-2.4	0.90 ± 0.32

Table 6-2 Bipolar switching SET and RESET voltages of BZO and SZO nanocrystal assemblies.

Bipolar Switching		
Material	**SET Voltage (V)**	**RESET Voltage (V)**
BZO-5	1.64 ± 0.17	-1.72 ± 0.22
BZO-5/SZO-9	2.85 ± 0.40	-1.68 ± 0.45
BZO-5/SZO-2.4	-1.31 ± 0.23	1.48 ± 0.40
BZO-2.7/SZO-9	-2.19 ± 0.34	2.99 ± 0.71

6.2.2 Sample Characterization Methods

Solid state techniques used to characterize the obtained powders include: Powder X-Ray diffraction (PXRD, Thermo Scientific ARL XTra diffractometer 40 kV 40 mA) using Cu Kα radiation (0.15418 nm) for crystal structure identification,

via comparison with ICSD standards, and Transmission Electron Microscopy (TEM, JEOL JEM-2000FS operated at 200 kV with Cs corrector) for morphology and size distribution assessment. Solution techniques were used for the characterization of the solutions, which include Dynamic Light Scattering (DLS, Marlvern Nano ZS) with backscatter detection of 173° for solovodynamic diameter and Nuclear Magnetic Resonance (NMR, Bruker 300MHz Avance I Ultrashield)

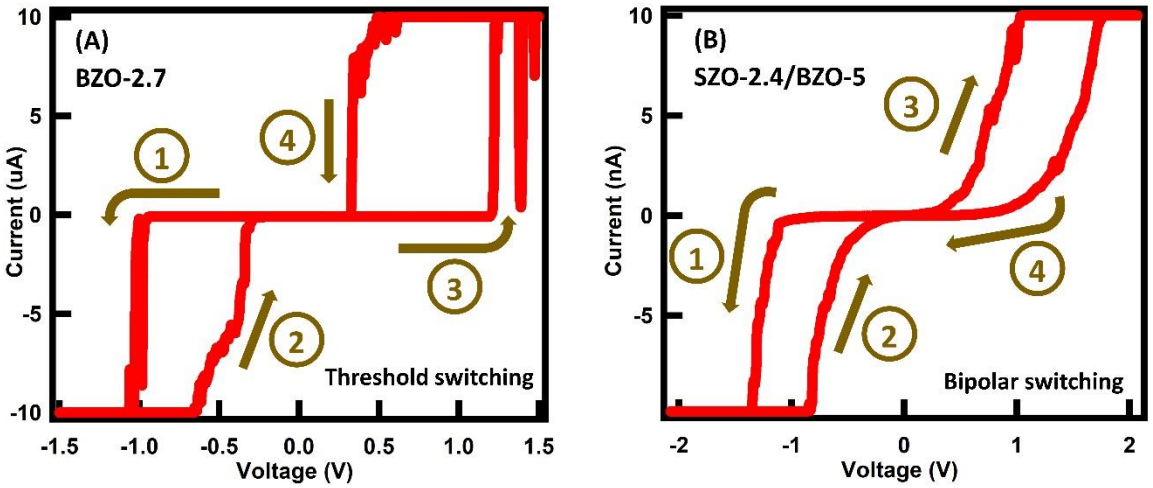

Figure 6-3 (A) Threshold switching behavior of 2.7 nm BZO nanocrystal assemblies. (B) Bipolar switching behavior of SZO-2.4 and BZO-5 mixture nanocrystal assemblies.

operating at 1H frequency of 500.13 MHz for solution purity check.

The local resistive switching response was measured at room temperature using Asylum Research Cypher ES ORCA™ conductive-AFM module. A conductive Rocky Mountain Nanotech 25Pt400B cantilever with an 8 N/m spring contact and a fundamental resonant frequency of 10 kHz was used to perform all topographic and conductive imaging. Conductive silver paste (TED PELLA, Inc.) fixed the sample bottom electrode to the conductive wired sample puck to form the C-AFM electrical circuit. The conductive cantilever is connected to an ORCA™ dual-gain transimpedance amplifier and held at ground while the sample is biased

from bottom electrode during electrical testing. Local resistive switching I-V curves were collected in current-voltage (I-V) spectroscopy point-mode. The bias applied to Pt substrate ranges from 1 V to 5 V depending on nanoribbon actual SET voltage at a frequency of 0.99 Hz. The cantilever deflection setpoint was held at 0.02 V to ensure sufficient tip-sample contact without mechanically inducing artificially high current values.[93]

6.3 Results and Analysis

Figure 6-2 (a) - (d) show AFM topography images of individual nanoribbon with nanopositioner stopping time of one second, six seconds and their corresponding AFM height profile images respectively. The one second stopping time produced a nanoribbon width of ~ 3.6 μm and 100 nm height; the six second stopping time produced a nanoribbon width of 16 μm and 500 nm height. To demonstrate the versatility of flow coating process, we fabricated a $BaZrO_3$ thin film using a single step size 5 mm with no stopping time (Figure 6-2 c). The average thickness of as-fabricated $BaZrO_3$ thin film is 117.9 nm ± 22.1 nm. While less uniform, the high productive fabrication process of nanoscale thin film with length and width in millimeter takes less than 10 seconds. The uniformity of nanocrystal assemblies can be further improved by utilizing finer blade and advanced nanopositioner system. Figure 6-2 (g) is the optical microscope image showing highly ordered arrays of individual nanoribbons deposited on Ti/Pt-coated silicon substrate utilizing the flow-coating technique. The nanoribbon dimensions are well-controlled by varying the substrate stopping time, as shown in Figure 6-2 (h).

Interestingly, we observed threshold switching within six nanocrystal assembly systems and bipolar switching within four nanocrystal assembly systems (Table 1). The transition between bipolar switching to threshold switching can be explained by current induced Joule heating. Except SZO-2.4, all threshold switching current saturated at 10 μA under C-AFM I-V spectroscopy, which is the maximum detection range of Asylum Research ORCA™ dual-gain cantilever holder (Figure 6-3a as an example). It is reported that C-AFM current density at tip-sample junction can be up to 10^9 A/cm^2 since most modern C-AFM is not equipped with current compliance function.[94,260] We estimate that the actual current value in LRS is much higher than 10 μA. In bipolar switching assemblies, besides BZO-5, all the LRS current are all below 10 μA (Figure 6-3b). Several studies have proved that Joule heating will shift nonvolatile bipolar or unipolar switching to volatile threshold switching by I-V cycling at higher temperatures[35], reducing heat dissipation by decreasing metal electrode thickness[34] and increasing current compliance to induce higher amount of Joule heating.[261] Considering threshold switching exhibits much higher LRS current than bipolar switching. We posit that the transformation between bistable bipolar switching and monostable threshold switching is due to unstable conductive filament caused by current induced Joule heating.

Fabricating nanoribbons comprising nanocrystals of varying diameter enables size-dependent studies of the resistive switching operating voltages. Within both BZO and SZO systems, SET voltage is inversely proportional to nanocrystal size. Several studies suggested that the metal oxides nanocrystal, such as CeO_2, $BaTiO_3$ and $PbTiO_3$ lattice parameters will significantly increase as the

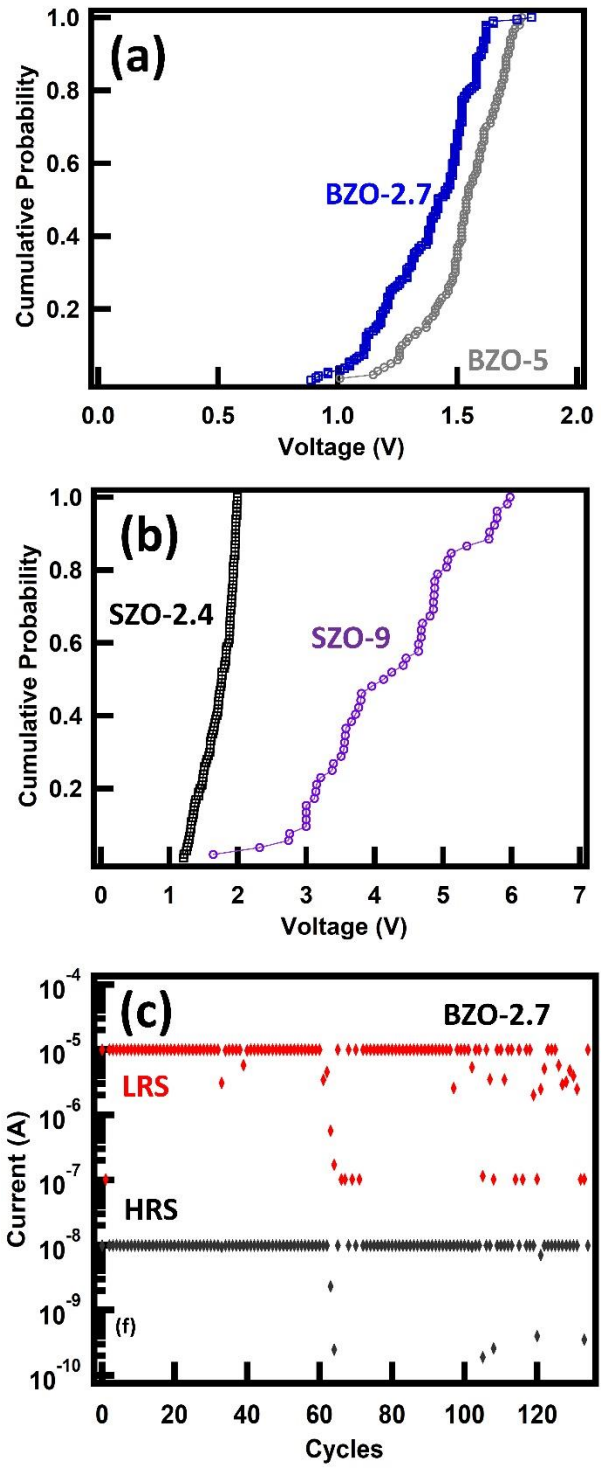

Figure 6-4 (a) and (b) Cumulative probability of BZO-2.7 (blue), BZO-5 (grey) and SZO-2.4 (black) ~ 3.88 eV and SZO-9 (purple) SET voltages. (c) 135 cycles I-V sweeping on BZO-2.7 nanoribbon.

nanoparticle size decreases below a critical diameter of range from 11 to 100 nm.[262–265] The minimum lattice parameter expansion within BZO nanocrystals was observed to be 0.5%.[266] Therefore we posit that smaller BZO and SZO nanocrystals have higher lattice parameters than their larger diameter nanocrystal counterparts. The larger unit cell facilitates more structural fluctuations and hence leads to increased oxygen vacancy diffusion.[267] The highly active oxygen ions (vacancies) enhance the resistive switching process and t hus lower the switching voltage.[268] Figure 6-4 (a) and (b) present the cumulative distribution of SET voltage within BZO and SZO nanocrystal assemblies. Both small nanocrystal assemblies show lower and uniform SET voltages. SZO-9 system shows much higher SET

voltages with a wide fluctuation range from 1.64 V to 5.98 V. Figure 6–4 (c) presents 135 consecutive threshold switching cycles with in one BZO-2.7 nanoribbon. Most if the selectivity remains around 10^3 suggests the stable switching behavior even without the protection of current compliance.

Figure 6-5 (a) and (b) present Tauc plot for BZO and SZO systems where the linear fitting of $(\alpha h\nu)^2$ term on X-axis intercept evaluates the material direct band gap. Both smaller sized nanoparticles display narrower band gaps as compared to the larger nanoparticles possibly due to the presence of oxygen vacancy (V_O).[269] We suspect that these V_O create sub-bandgap energy levels, and the charge transfer transitions involving these impurity level can give rise to this bandgap reduction.[270] This assumption is also further supported by enhanced resistive switching performance such as lower SET voltage and improved switching parameter uniformity. These observations supported the defects-induced resistance behavior of smaller size particles in line with previous literature.[271][272]

Variations in the switching voltages could also be attributed to changes in the packing efficiency for the various diameter constituent nanocrystals within the same nanoribbon geometry. Moreover, polydisperse systems will produce higher packing factors than monodisperse systems.[273]. Since the C-AFM measurements were conducted at an 80 nm equivalent thickness area with a tip radius of 35 nm, we assume the electrical field is confined in a 40 nm in radius and 80 nm high cylindrical space. The packing density for monodisperse and bidisperse spheres in a cylindrical container can be expressed as:[274]

$$D = 0.604 - 0.1812\beta r \qquad (1)$$

$$D_{1,2} = 0.791 - 4.06r_1 - 0.342\frac{r_1}{r_2} - 5.02r_2 \qquad (2)$$

Where β is the cylinder surface to volume ratio, r_1 is small particle radius and r_2 is large particle radius. Interestingly, the resistive switching SET voltage in both BZO and SZO systems decrease with increasing packing density as shown in Figure 6-5 (c) and (d). Under the same relative thickness, a higher nanoparticle packing density reduces the inter-particle distance. It is reasonable to assume the conductive filament is easier to form in more tightly packed nanocrystal assemblies. The switching voltage is reduced since less inter-particle carrier hopping per unit length is required. Varying the nanocrystal size also affects its shape, surface charge distribution, surface trap density and packing density[230,275]. Thus, quantitative correlations between nanocrystal size and resistive switching performance still remains tedious.

The BZO system exhibits a lower operating voltage than the SZO system for the same approximate nanocrystal diameter, suggesting that additional contributions are occurring beyond the size effect. BZO-2.7 displayed an average switching voltage of 1.39 ± 0.19 V while SZO-2.4 displayed an average switching voltage of 1.53 ± 0.16 V, resulting in a significant statistical difference with a calculated p-value less than 0.0001. Site defects/vacancies usually serve as the mobile charge carriers to facilitate conductive filament formation.[276] While both systems possess the ABO_3 perovskite crystal structure, studies show that BZO nanoparticles possess significantly more A-site vacancies as compared to SZO nanoparticles because the lower Ba^{2+} diffusion rate during synthesis results in fewer A-site vacancies being filled.[266,277] We assume that both BZO and SZO

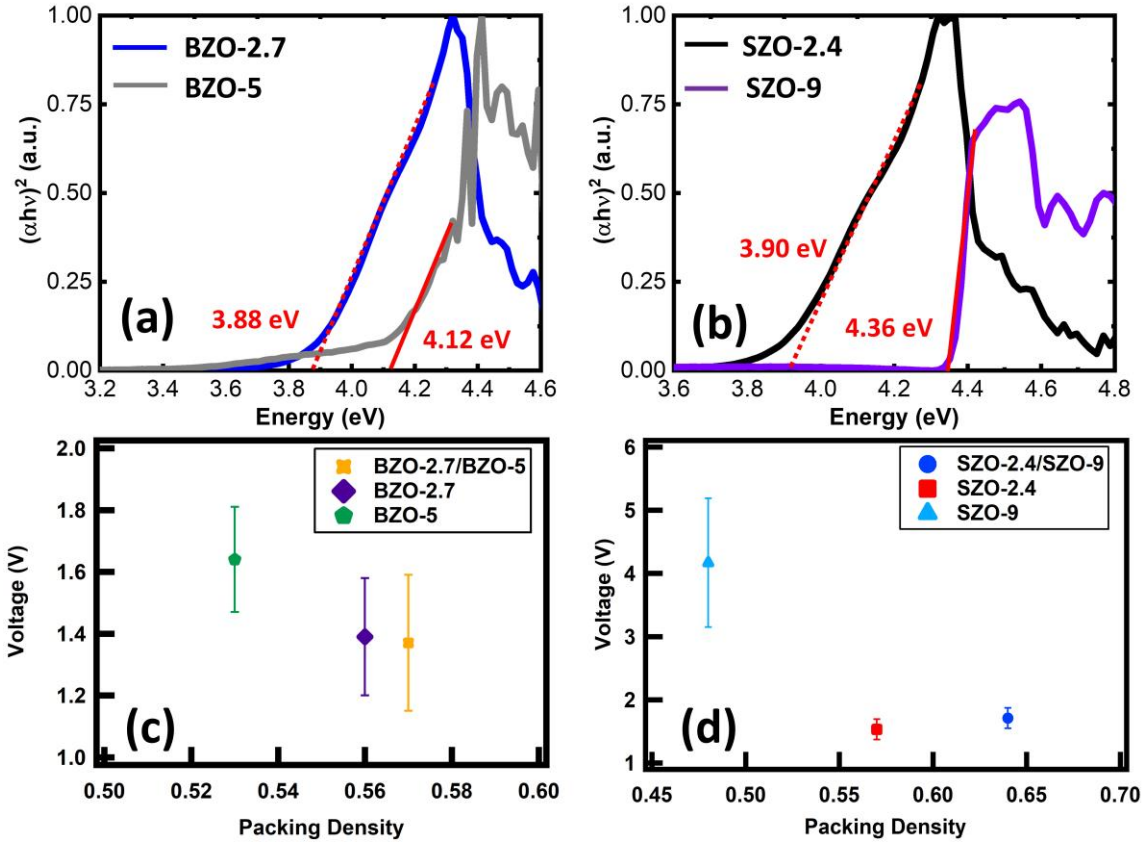

Figure 6-5 (a) and (b) Band gap estimation using Tauc plot. BZO-2.7 (blue) ~ 3.88 eV and BZO-5 (grey) ~ 4.12 eV, SZO-2.4 (black) ~ 3.9 eV and SZO-9 (purple) ~ 4.36 eV. (c) and (d) Relationship between packing density and SET voltage within BZO and SZO systems respectively.

have the same approximate B-site vacancy density as B-site vacancies in perovskite structures are less prevalent for two main reasons:[278] (1) B-site has high charge. B-site defect is not thermodynamically favored because of its high charge and relatively small size. (2) B-site structural stability. Compared to the 12-fold cuboctahedral A-site the B-site cation forms a more stable BO_3 octahedral structure. The lower BZO operating voltage can be therefore be attributed to a higher charge carrier density. Barium also possesses a lower electronegativity than strontium ; subsequently the Ba-O bond (343 kJ/mol) is weaker than Sr-O bond (454 kJ/mol).[279,280] The lower strength of the Ba-O bond enhances the

mobility of oxygen ions which further facilitates and enhances resistive switching.[281]

6.4 Summary

In summary, we introduced a low-cost and versatile flow coating fabrication approach to produce memristive nanoribbons comprising $BaZrO_3$ and $SrZrO_3$ perovskite nanocrystals. We demonstrated the impact of nanocrystal size and polydispersity effects on resistive switching operating voltages by comparing different sizes BZO and SZO nanoparticle assemblies. We also studied A-site substitutional effect by directly comparing resistive switching SET voltages of BZO and SZO nanoribbons comprising same size nanoparticles. The recent advancement of solution processing techniques provides a low-cost and facile synthesis of complex functional nanocrystals with high controllability over particle size, inter-particle distance and material structure. We thus expect this study will motivate the works investigating applications on next-generation flexible electronics toward novel functional nanostructures which involves controlling material size and structural effects. In addition, the use of advanced scanning probe techniques to investigate multifunctional perovskite here also promotes the studies of materials with coupled magnetic, electric and structural order effects such as ferromagnetism, ferroelectricity and ferroelasticity.

CHAPTER 7

CONCLUSIONS AND FUTURE OUTLOOK

7.1 Conclusions

The dissertation topics cover ordered functional nanoporous template with its applications in nanoelectronics and solution-processed memristor. It first thoroughly reviews the state-of-the-art ordered nanoporous functional templates fabrication approaches starting from anodic aluminum oxide (AAO), a highly ordered porous membrane achieved by direct anodization. Individually addressable HfO_2 nanocapacitor arrays with ultrahigh density were fabricated using AAO template. The chapter also shifts the highlight to transitional binary metal oxides templates and their applications, which are fabricated using same anodization method but exhibit more functional in many areas such as emery harvesting, sensors and human implants. The second half of the chapter reviews a series of synthetic approaches using AAO as master template of nanoporous membranes with complex materials including perovskites oxide and nitride, which are extremely difficult to pattern over a large area using conventional lithographic methods. Large area memristive TiO_2 nanoporous template was synthesized utilizing AAO negative replica method.

After the pioneering solution-processed memristor works from our group, HfO_2 nanoribbons with 5 phosphonic acid ligands with different lengths were measured using conductive AFM. Statistical results showed that resistive switching operating voltage scales with ligand length by collecting 40 results from

each type of memristor. Moreover, by conducting switching voltage thickness dependency studies, I also confirmed that different switching voltages were not caused by testing location dielectrics thickness variation.

In the second solution-processed memristor research, two types of perovskites nanoparticles, $BaZrO_3$ and $SrZrO_3$, capped with same phosphonic acid ligand but in two different sizes were chosen. Material substitutional effects and nanoparticle size effects were considered to cause the switching voltage variations. By comparing same size $BaZrO_3$ and $SrZrO_3$ nanoparticles, $BaZrO_3$ showed lower switching voltage due to possibly higher A-site defects concentration which leads to higher oxygen vacancy concentration. Smaller nanoparticles also exhibit lower switching voltage due to surface relaxation resulted higher oxygen vacancy mobility and higher nanoparticle packing densities which reduce overall inter-particle charge carrier hopping energies. For the first time, 50/50 mixture component systems were used in solution-processed memristors to create variations in packing densities to examine the nanoparticle size effects.

7.2 Future Work

While conductive AFM demonstrates its ability to locally testing RRAM device resistive switching property, there is still plenty of room for further improvement of AFM conductive testing. C-AFM is a more practical characterization tool in terms of surface scanning and qualitative determination of conductive region over a specific area. Most commercial C-AFM does not come with current compliance and is able to apply voltage up to 10 V which creates a

huge problem for local resistive switching testing. The effective electron flowing area of a conductive probe, different from actual contact area, depending on a series of parameters such as scanning force, cantilever stiffness, apex radius and relative ambient humidity ranges from 1 to 700 nm^2.[94] Since no commercial C-AFM applies current limitation, current passing through probe apex can cause an ultra-high current density up to 10^9 A cm^{-2} in LRS.[260] This extremely high current is very harmful and likely to result in sample dielectric breakdown, probe apex local anodic oxidation, melting of the metal coating layer or even melting of pure Pt apex due to Joule heating.[282] For this reason, RRAM device endurance measurement, one of the most crucial performance testing of an electronic device, is extremely to carry out utilizing C-AFM. To solve this problem, C-AFM can be conducted in vacuum or dry nitrogen ambient. Local redox reaction can be greatly reduced since probe apex water meniscus at tip/sample surface is eliminated. External source meter with accurate control of current compliance should also be plugged into and override AFM circuit for current limitation purposes.

Utilizing 0D nanoparticles, solution-processed memristors have more degrees of freedom in terms of electrical property tuning by varying nanoparticle size and capping ligand. As described in chapter 4 and chapter 5, the long-debated oxygen vacancy mediated charge carrier transport mechanism can be revealed by creating nanoparticles with different oxygen defects concentrations caused by nanoparticle size effect. The flow-coating fabrication technique is also a convective and low-cost alternative approach of patterning regular nanostructures over a large scale. However, the lack of microstructure control such as film roughness variation, still needs to be addressed since high deposition uniformity is always

required in integrated circuit devices. Besides, considering the revolution in electronic device miniature, it is important to examine the resistive switching uniformity under elevated working temperature since chemical ligands might be modified.

After more than three decades of development, modern atomic force microscope is able to achieve sub-nanometer resolution easily. Other derivatives of AFM have also emerged such as different electrical property measurements, magnetic measurements, thermal measurements and force measurements. Till now, three major draw backs hinder the further application of this technique: (1). operation easiness and scanning speed. Unlike different electron microscopy techniques, depending on different operation modes, AFM requires much a series of pre-scanning preparations such as laser alignment, cantilever frequency tuning and other calibrations. The complicated system calibration sometime even requires using different samples, which often discourages low-level AFM users. (2). Inconsistent scanning results. Atomic force microscope characterization results are highly reliant on user's experience and skill. The micro-machined probe empowers AFM testing in many research fields but also bring in uncertainties. For example, tip-sample contact resistance is a changeable factor relevant to contact force, apex radius and cleanness of the sample. These parameters will also change during measurement due to sample surface roughness variation and tip weariness. A more intelligent AFM controlling software is urgently needed to help users to make decisions. For instance, one AFM manufacturer invented True Non-Contact™ technique which yields same resolution surface image without bringing tip-sample into contact. This approach greatly reduces tip apex weariness issue

which would be difficult to detect using conventional tapping mode AFM. (3) AFM scanning rate. At industrial level, critical dimension scanning electron microscopy (CD-SEM) is one of the most popular tools in semiconductor wafer metrological fields. Although as compared to SEM, AFM is not advantageous in scanning speed, it measures materials without material related properties (conductive and non-conductive) and does not cause sample electron beam damage.[283] As the advancing of technology, latest industrial level AFM is capable of 300 mm wafer automated inspection.[284]

APPENDIX 1

ATOMIC FORCE MICROSCPE MECHANICAL TESTING

Atomic force microscope has been used to investigate nanomaterial mechanical properties for more than three decades. Comparing to conventional nanoindentation and tensile test techniques, AFM has a unique advantage over conventional nanoindentation techniques – micromachined probe. The fine AFM force control and ultra-sharp tip are able to precisely maintain an extremely shallow sample indentation depth during nanoindentation process. This feature enables the mechanical property testing of ultra-thin nanomaterials since conventional nanoindenter (radius ~ um) is not sensitive enough to detect the subtle sample deformation.

I assume the reader is fully aware of basic AFM operation including laser alignment, cantilever tuning and basic tapping mode and contact mode scanning. Here, I will start from the point where laser is correctly aliened (SUM signal normal), cantilever deflection zeroed and is positioned at sample surface. Before every AFM mechanical testing, the most important preparations are to calibrate three properties: 1) deflection sensitivity; 2) spring constant; 3) tip radius/shape.

In Asylum Research AFM system, deflection sensitivity also called InVOLS (Inverse Optical Lever Sensitivity). The unit of deflection sensitivity is nm/V. Deflection sensitivity describes the relationship between the laser movement due to cantilever deflection on photodiode (in volts) and actual cantilever deflection (in nm).[285] This is not a cantilever or photo detector specific property. It is the overall sensitivity of the AFM system including cantilever, photodetector, relative

laser spot and working environment (in air or liquid). Whereas cantilever spring constant is a material property which does not change with different working environments. Asylum Research software has a very convenient, fully automatic deflection sensitivity and spring constant calibration function – Getreal™, as

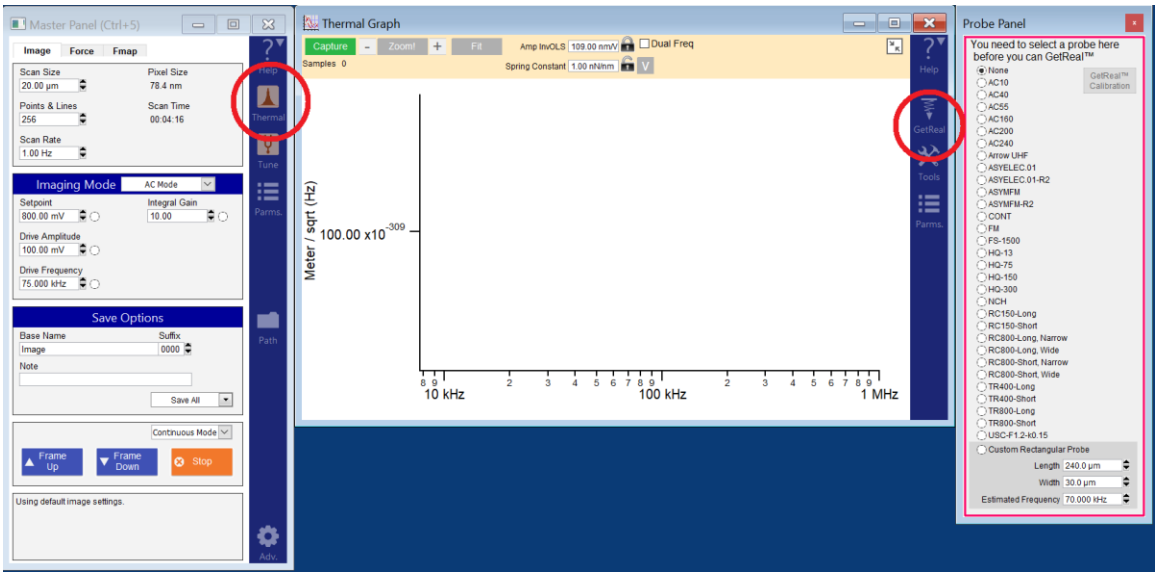

Figure A-1 Asylum Research software thermal tuning tab.

shown in Figure A-1. Click Thermal in the main tab and then click GetReal in thermal graph tab. A probe selection panel will pop out with a list of Asylum branded cantilever. If you do not find your probe on the list, simply choose the last option "custom rectangular probe" and input cantilever specifications from specs sheet on the box. The computer will do a rectangular beam dimensional modelling fitting according to your input. In the main tab -> Force -> Cal. Tab (Figure A-2), three green lights in front of Defl InvOLS, Amp InvOLS and Spring Constant means these three parameters have been properly tuned. However, one can also readjust these parameters in post data analysis process in elastic tab. The most precise way to calibrate tip shape and cone angle would be SEM imaging. But I

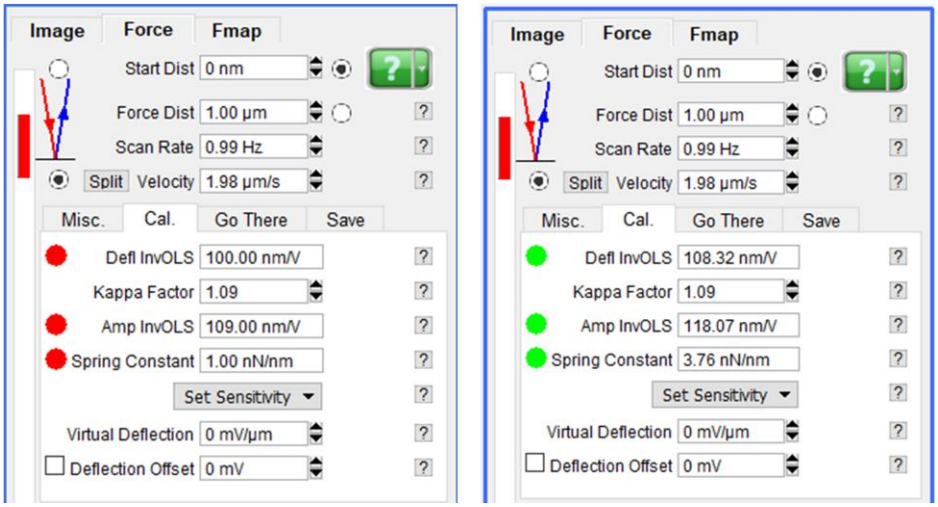

Figure A-2 Asylum Research software force calibration window.

often found that cantilever specs sheet on the box is good enough for nanoindentation.

The main testing parameters for nanoindentation are force distance, scan rate, trigger channel and trigger point. They can be found in force -> Misc tab. Choose all parameters properly and then do a 'single force' to perform one single mechanical testing. After single force, open Master Force Panel in AFM Analysis and go to elastic tab for force curve analysis. Correctly analyzing the force curve is the key to extract sample mechanical property. Figure A-3 shows a standard AFM force curve image. The Y-axis is force. Positive force means the force direction towards sample (press) and negative force means force direction towards tip (adhesive). The X-axis is tip sample separation. Negative value means tip-sample separation and positive value means sample indentation depth. Red curve is approaching curve, blue curve is retracting curve. Brown dashed line is the model fit of tip approaching movement and blue dashed line is the fit of retracting

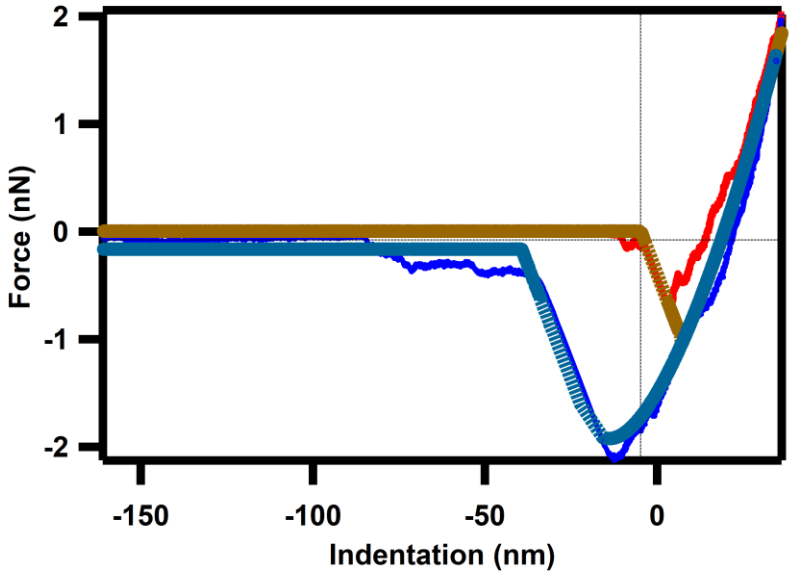

Figure A-3 A typical force curve on an adhesive PDMS sample.

movement. The task here is to adjust contact model parameters to fit the force curves by adjusting contact models (Hertz, DMT, JKR and Oliver-Pharr), tip geometry, fit regions and model assumptions. The fitted results will be shown in the lower right corner of elastic tab.

APPENDIX 2

AFM VISCOELASTIC MAPPING (AM-FM)

AM-FM mode is the combination of amplitude modulation and frequency modulation AFM. In this mode, the cantilever is simultaneously driven by two sources: the first mode is mechanically driven by shake piezo at fundamental frequency like the normal AFM, the second mode is photothermally driven by the secondary blue laser at a much higher frequency.[286] The major advantage of photothermal excitation over conventional shake piezo is it is inducing thermal stress and then causing cantilever oscillation directly on the cantilever beam, instead of shaking cantilever, which also mechanically drives cantilever holder and working ambient (e.g. liquid) simultaneously.[287]

The operation of AM-FM is straightforward but tricky. To start, go to tune tab -> advanced, switch tune drive from piezo to blue drive to turn on the secondary blue laser. Move the blue laser spot position to the bottom part of the cantilever and tune both lasers. The first mode target amplitude is 2V, frequency is cantilever fundamental frequency fo. Second mode target amplitude should be much lower than first mode, typically 25 mV, frequency is one of the higher eigenmode frequencies. It should be noted that Asylum software default setting is second eigendmode ($\sim 6 \times fo$). One should manually adjust the upper and lower bounds of second mode to locate the desired eigenmode resonance frequency.

After first round tuning, move blue laser spot around to maximize the Amplitude 2 on Sum and Deflection panel. You will lose some Amplitude 1 signal so retune both lasers after the process. Then use GetReal function to calibrate

cantilever spring constant and deflection sensitivity. After calibration, you should see two green lights in AMFM panel lever tab. After cantilever pre-engage and approaching, retune the tip again to make sure amplitude 1 is 2V and amplitude 2 is 25 mV. Before scanning, click engage on sum and deflection panel to engage the tip. Make sure phase 1 is somewhere between 40~80° and phase 2 is slightly less than 90°. If phase 2 is hopping (which is quite common, especially on AC240TSA-R3), try to use higher eigenmode. Young's modulus mapping can only be calculated in repulsive 2nd mode region. One plausible for extremely unstable phase 2 is the second eigenmode frequency peak is very close to the integer multiplication of fundamental frequency f_0. In other word, they are in harmonics. Two close enough peak can confuse second lock-in amplifier. So, the secondary cantilever is being driven by first and second mode simultaneously. To solve this problem, simply use third eigenmode, which is 17.5 times fundamental frequency. However, an extra tip-sample stiffness calibration is needed for third eigenmode imaging since the third mode cantilever spring constant is much higher.

APPENDIX 3

ULTRA-THIN AAO TRANSFER

For two-step anodization AAO fabrication and barrier layer removal, read through reference [288]. The ultrathin anodic aluminum oxide (AAO) membrane we bought from TopMembrane, Shenzhen is double-thorough template, reinforced with polystyrene, without aluminum substrate and barrier layer. Open the box, ultrathin AAO looks like a piece of cellophane. Be very cautious here, do not flip AAO membrane. Only the front side (facing up) is coated with polystyrene

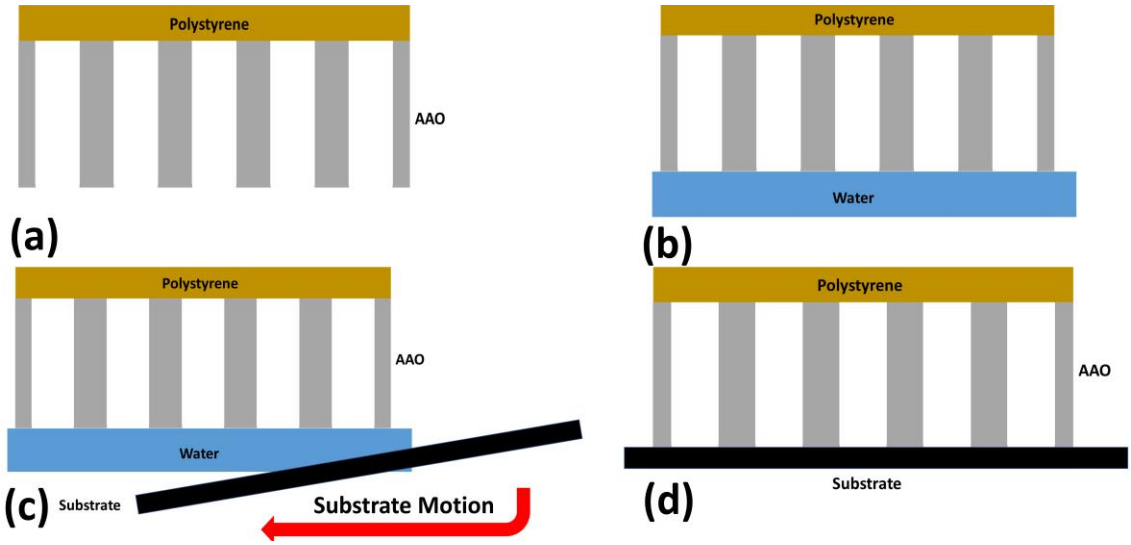

Figure A-1 Schematics of ultrathin AAO transfer.

as shown in Figure A-4(a). Always keep reinforced side up! Cut a small piece of membrane and put it onto water. Keep polystyrene side facing up (Figure A-4c b). Use substrate to take the floating AAO membrane. The motion must be quick or there will be wrinkles (Figure A-4c). You can use flat-head tweezer to gently pull AAO on the size if there is wrinkle. Rinse transferred AAO with chloroform or toluene to remove polystyrene (Figure A-4 d).

BIBLIOGRAPHY

1. Invitation, A.; Field, N.; Feynman, R.P.; Brittanica, E. There's Plenty of Room at the Bottom. *Eng. Sci. Mag.* **1960**, *XXIII*.
2. Schaller, R.R. Moore's Law: past , present , future. *IEEE Spectr.* **1997**, *34*, 52–59.
3. Aggarwal, A.; Alpern, B.; Chandra, A.K.; Snir, M. Model for Hierarchical Memory. *Conf. Proc. Annu. ACM Symp. Theory Comput.* **1987**, 305–314.
4. Wong, H.S.P.; Salahuddin, S. Memory leads the way to better computing. *Nat. Nanotechnol.* **2015**, *10*, 191–194.
5. Meijer, G.I. MATERIALS SCIENCE: Who Wins the Nonvolatile Memory Race? *Science (80-.).* **2008**, *319*, 1625–1626.
6. Yu, S.; Chen, P.-Y. Emerging Memory Technologies: Recent Trends and Prospects. *IEEE Solid-State Circuits Mag.* **2016**, *8*, 43–56.
7. Nakamoto, H.; Yamazaki, D.; Yamamoto, T.; Kurata, H.; Yamada, S.; Mukaida, K.; Ninomiya, T.; Ohkawa, T.; Masui, S.; Gotoh, K. A passive UHF RF identification CMOS tag IC using ferroelectric RAM in 0.35-μm technology. *IEEE J. Solid-State Circuits* **2007**, *42*, 101–109.
8. Eshita, T.; Wang, W.; Nakamura, K.; Mihara, S.; Saito, H.; Hikosaka, Y.; Inoue, K.; Kawashima, S.; Yamaguchi, H.; Nomura, K. Development of ferroelectric RAM (FRAM) for mass production. *2014 Jt. IEEE Int. Symp. Appl. Ferroelectr. Int. Work. Acoust. Transduct. Mater. Devices Work. Piezoresponse Force Microsc. ISAF/IWATMD/PFM 2014* **2014**, 1–3.
9. Zhu, J.-G.; Zheng, Y.; Prinz, G.A. Ultrahigh density vertical magnetoresistive random access memory (invited). *J. Appl. Phys.* **2002**, *87*, 6668–6673.

10. Dong, X.; Wu, X.; Sun, G.; Xie, Y.; Li, H.; Chen, Y. Circuit and microarchitecture evaluation of 3D stacking magnetic RAM (MRAM) as a universal memory replacement. *Proc. - Des. Autom. Conf.* **2008**, 554–559.

11. Horii, H.; Yi, J.H.; Park, J.H.; Ha, Y.H.; Baek, I.G.; Park, S.O.; Hwang, Y.N.; Lee, S.H.; Kim, Y.T.; Lee, K.H.; et al. A novel cell technology using N-doped GeSbTe films for phase change RAM. In Proceedings of the 2003 Symposium on VLSI Technology. Digest of Technical Papers (IEEE Cat. No.03CH37407); Japan Soc. Applied Phys, 2003; Vol. 2003, pp. 177–178.

12. Ha, Y.H.; Yi, J.H.; Horii, H.; Park, J.H.; Joo, S.H.; Park, S.O.; Chung, U.I.; Moon, J.T. An Edge Contact Type Cell for Phase Change RAM Featuring Very Low Power Consumption. *Dig. Tech. Pap. - Symp. VLSI Technol.* **2003**, 175–176.

13. Waser, R.; Dittmann, R.; Staikov, C.; Szot, K. Redox-based resistive switching memories nanoionic mechanisms, prospects, and challenges. *Adv. Mater.* **2009**, *21*, 2632–2663.

14. Wong, H.S.P.; Lee, H.Y.; Yu, S.; Chen, Y.S.; Wu, Y.; Chen, P.S.; Lee, B.; Chen, F.T.; Tsai, M.J. Metal-oxide RRAM. *Proc. IEEE* **2012**, *100*, 1951–1970.

15. Chen, Y.; Jung, G.Y.; Ohlberg, D.A.A.; Li, X.; Stewart, D.R.; Jeppesen, J.O.; Nielsen, K.A.; Stoddart, J.F.; Williams, R.S. Nanoscale molecular-switch crossbar circuits. *Nanotechnology* **2003**, *14*, 462–468.

16. Rueckes, T.; Kim, K.; Joselevich, E.; Tseng, G.Y.; Cheung, C.L.; Lieber, C.M. Carbon nanotube-based nonvolatile random access memory for molecular computing. *Science (80-.).* **2000**, *289*, 94–97.

17. Shin, J.S.; Pierce, N.A. Rewritable memory by controllable nanopatterning of

DNA. *Nano Lett.* **2004**, *4*, 905–909.

18. Scott, J.F. Ferroelectric Memories. **2000**, *246*, 113–115.

19. Müller, G.; Happ, T.; Kund, M.; Lee, G.Y.; Nagel, N.; Sezi, R. Status and outlook of emerging nonvolatile memory technologies. *Tech. Dig. - Int. Electron Devices Meet. IEDM* **2004**, 567–570.

20. Lee, S.H.; Hwang, Y.N.; Lee, S.Y.; Ryoo, K.C.; Ahn, S.J.; Koo, H.C.; Jeong, C.W.; Kim, Y.T.; Koh, G.H.; Jeong, G.T.; et al. Full integration and cell characteristics for 64Mb nonvolatile PRAM. *Dig. Tech. Pap. - Symp. VLSI Technol.* **2004**, 20–21.

21. Chua, L. Memristor-The missing circuit element. *IEEE Trans. Circuit Theory* **1971**, *18*, 507–519.

22. Wang, J.; Sun, B.; Gao, F.; Greenham, N.C. Memristive devices based on solution-processed ZnO nanocrystals. *Phys. Status Solidi Appl. Mater. Sci.* **2010**, *207*, 484–487.

23. Jung, M.; Shalf, J.; Kandemir, M. Design of a large-scale storage-class RRAM system. **2013**, 103.

24. Waser, R.; Aono, M. Nanoionics-based resistive switching memories. *Nat. Mater.* **2007**, *6*, 833–840.

25. Xu, W.; Li, H.; Xu, J.-B.; Wang, L. Recent Advances of Solution-Processed Metal Oxide Thin-Film Transistors. *ACS Appl. Mater. Interfaces* **2018**, acsami.7b16010.

26. Garcia, V.; Fusil, S.; Bouzehouane, K.; Enouz-Vedrenne, S.; Mathur, N.D.; Barthélémy, A.; Bibes, M. Giant tunnel electroresistance for non-destructive readout of ferroelectric states. *Nature* **2009**, *460*, 81–84.

27. Auciello, O.; Scott, J.F. THE PHYSICS OF to save the document on your. **2016**.

28. Jeong, D.S.; Schroeder, H.; Waser, R. Mechanism for bipolar switching in a Pt/ TiO2 /Pt resistive switching cell. *Phys. Rev. B - Condens. Matter Mater. Phys.* **2009**, *79*, 1–10.

29. Jeong, D.S.; Thomas, R.; Katiyar, R.S.; Scott, J.F.; Kohlstedt, H.; Petraru, A.; Hwang, C.S. Emerging memories: Resistive switching mechanisms and current status. *Reports Prog. Phys.* **2012**, *75*.

30. Sawa, A. Resistive switching in transition metal oxides. *Mater. Today* 2008, *11*, 28–36.

31. Linn, E.; Rosezin, R.; Kügeler, C.; Waser, R. Complementary resistive switches for passive nanocrossbar memories. *Nat. Mater.* **2010**, *9*, 403–406.

32. Lee, M.J.; Lee, C.B.; Lee, D.; Lee, S.R.; Chang, M.; Hur, J.H.; Kim, Y.B.; Kim, C.J.; Seo, D.H.; Seo, S.; et al. A fast, high-endurance and scalable non-volatile memory device made from asymmetric Ta2O5-xx/TaO2-xbilayer structures. *Nat. Mater.* **2011**, *10*, 625–630.

33. Ielmini, D.; Zhang, Y. Analytical model for subthreshold conduction and threshold switching in chalcogenide-based memory devices. *J. Appl. Phys.* **2007**, *102*.

34. Chang, S.H.; Chae, S.C.; Lee, S.B.; Liu, C.; Noh, T.W.; Lee, J.S.; Kahng, B.; Jang, J.H.; Kim, M.Y.; Kim, D.W.; et al. Effects of heat dissipation on unipolar resistance switching in PtNiOPt capacitors. *Appl. Phys. Lett.* **2008**, *92*, 28–31.

35. Chang, S.H.; Lee, J.S.; Chae, S.C.; Lee, S.B.; Liu, C.; Kahng, B.; Kim, D.W.; Noh, T.W. Occurrence of both unipolar memory and threshold resistance switching in a NiO film. *Phys. Rev. Lett.* **2009**, *102*, 1–4.

36. Kim, S.; Moon, H.; Gupta, D.; Yoo, S.; Choi, Y.K. Resistive switching characteristics of Sol-Gel Zinc oxide films for flexible memory applications. *IEEE Trans. Electron Devices* **2009**, *56*, 696–699.

37. Walczyk, C.; Wenger, C.; Sohal, R.; Lukosius, M.; Fox, A.; Dbrowski, J.; Wolansky, D.; Tillack, B.; Müssig, H.J.; Schroeder, T. Pulse-induced low-power resistive switching in Hf O2 metal-insulator-metal diodes for nonvolatile memory applications. *J. Appl. Phys.* **2009**, *105*.

38. Strukov, D.B.; Alibart, F.; Stanley Williams, R. Thermophoresis/diffusion as a plausible mechanism for unipolar resistive switching in metal-oxide-metal memristors. *Appl. Phys. A Mater. Sci. Process.* **2012**, *107*, 509–518.

39. Hong, X.L.; Loy, D.J.J.; Dananjaya, P.A.; Tan, F.; Ng, C.M.; Lew, W.S. Oxide-based RRAM materials for neuromorphic computing. *J. Mater. Sci.* **2018**, *53*, 8720–8746.

40. Lin, K.L.; Hou, T.H.; Shieh, J.; Lin, J.H.; Chou, C.T.; Lee, Y.J. Electrode dependence of filament formation in HfO2 resistive-switching memory. *J. Appl. Phys.* **2011**, *109*.

41. Kim, K.M.; Kim, G.H.; Song, S.J.; Seok, J.Y.; Lee, M.H.; Yoon, J.H.; Hwang, C.S. Electrically configurable electroforming and bipolar resistive switching in Pt/TiO 2 /Pt structures . *Nanotechnology* **2010**, *21*, 305203.

42. Kim, K.M.; Choi, B.J.; Lee, M.H.; Kim, G.H.; Song, S.J.; Seok, J.Y.; Yoon, J.H.; Han, S.; Hwang, C.S. A detailed understanding of the electronic bipolar resistance switching behavior in Pt/TiO 2 /Pt structure. *Nanotechnology* **2011**, *22*.

43. Park, Y.A.; Sung, K.D.; Won, C.J.; Jung, J.H.; Hur, N. Bipolar resistance

switching and photocurrent in a BaTiO 3-δ thin film. *J. Appl. Phys.* **2013**, *114*, 1–6.

44. Ma, W.J.; Lin, S.P.; Luo, J.M.; Zhang, X.Y.; Wang, Y.; Li, Z.X.; Wang, B.; Zheng, Y. Highly uniform bipolar resistive switching characteristics in TiO 2/BaTiO3/TiO2 multilayer. *Appl. Phys. Lett.* **2013**, *103*, 1–6.

45. Huang, J.S.; Yen, W.C.; Lin, S.M.; Lee, C.Y.; Wu, J.; Wang, Z.M.; Chin, T.S.; Chueh, Y.L. Amorphous zinc-doped silicon oxide (SZO) resistive switching memory: Manipulated bias control from selector to memristor. *J. Mater. Chem. C* **2014**, *2*, 4401–4405.

46. Lin, C.C.; Tu, B.C.; Lin, C.C.; Lin, C.H.; Tseng, T.Y. Resistive switching mechanisms of V-doped SrZrO3 memory films. *IEEE Electron Device Lett.* **2006**, *27*, 725–727.

47. Ding, Y.; Xu, X.; Bhalla, A.; Yang, X.; Chen, J.; Chen, C. Switchable diode effect in BaZrO3 thin films. *RSC Adv.* **2016**, *6*, 60074–60079.

48. Pickett, M.D.; Stanley Williams, R. Sub-100fJ and sub-nanosecond thermally driven threshold switching in niobium oxide crosspoint nanodevices. *Nanotechnology* **2012**, *23*.

49. Ovshinsky, S.R. Reversible Electrical Switching Phenomena in Disordered Structures. *Phys. Rev. Lett.* **1968**, *21*, 1450–1453.

50. Yuan, X.; Tang, J.; Zeng, H.; Wei, X. Abnormal coexistence of unipolar , bipolar , and threshold resistive switching in an Al / NiO / ITO structure. **2014**, 1–5.

51. Yang, Y.; Sheridan, P.; Lu, W. Complementary resistive switching in tantalum oxide-based resistive memory devices Complementary resistive switching in

tantalum oxide-based resistive memory devices. **2013**, *203112*, 2012–2014.

52. Yan, Z.B.; Liu, J.M. Resistance switching memory in perovskite oxides. *Ann. Phys. (N. Y).* **2015**, *358*, 206–224.

53. Kim, K.M.; Jeong, D.S.; Hwang, C.S. Nanofilamentary resistive switching in binary oxide system; A review on the present status and outlook. *Nanotechnology* **2011**, *22*.

54. Pan, F.; Gao, S.; Chen, C.; Song, C.; Zeng, F. Recent progress in resistive random access memories: Materials, switching mechanisms, and performance. *Mater. Sci. Eng. R Reports* **2014**, *83*, 1–59.

55. Chen, J.Y.; Huang, C.W.; Chiu, C.H.; Huang, Y.T.; Wu, W.W. Switching Kinetic of VCM-Based Memristor: Evolution and Positioning of Nanofilament. *Adv. Mater.* **2015**, *27*, 5028–5033.

56. Lin, Y.S.; Zeng, F.; Tang, S.G.; Liu, H.Y.; Chen, C.; Gao, S.; Wang, Y.G.; Pan, F. Resistive switching mechanisms relating to oxygen vacancies migration in both interfaces in Ti/HfOx/Pt memory devices. *J. Appl. Phys.* **2013**, *113*.

57. Chen, C.; Song, C.; Yang, J.; Zeng, F.; Pan, F. Oxygen migration induced resistive switching effect and its thermal stability in W/TaO x/Pt structure. *Appl. Phys. Lett.* **2012**, *100*.

58. Kim, S.; Choi, S.; Lu, W. Comprehensive physical model of dynamic resistive switching in an oxide memristor. *ACS Nano* **2014**, *8*, 2369–2376.

59. Heo, Y.; Kan, D.; Shimakawa, Y.; Seidel, J. Resistive switching properties of epitaxial BaTiO3-δthin films tuned by after-growth oxygen cooling pressure. *Phys. Chem. Chem. Phys.* **2016**, *18*, 197–204.

60. Kim, H.D.; An, H.M.; Kim, T.G. Ultrafast resistive-switching phenomena observed in NiN-based ReRAM cells. *IEEE Trans. Electron Devices* **2012**, *59*, 2302–2307.

61. Lee, C.B.; Kang, B.S.; Benayad, A.; Lee, M.J.; Ahn, S.E.; Kim, K.H.; Stefanovich, G.; Park, Y.; Yoo, I.K. Effects of metal electrodes on the resistive memory switching property of NiO thin films. *Appl. Phys. Lett.* **2008**, *93*.

62. Schindler, C.; Thermadam, S.C.P.; Waser, R.; Kozicki, M.N. Bipolar and unipolar resistive switching in cu-doped SiO2. *IEEE Trans. Electron Devices* **2007**, *54*, 2762–2768.

63. Kund, M.; Beitel, G.; Pinnow, C.U.; Röhr, T.; Schumann, J.; Symanczyk, R.; Ufert, K.D.; Müller, G. Conductive bridging RAM (CBRAM): An emerging non-volatile memory technology scalable to sub 20nm. *Tech. Dig. - Int. Electron Devices Meet. IEDM* **2005**, *2005*, 754–757.

64. Gao, S.; Zeng, F.; Chen, C.; Tang, G.; Lin, Y.; Zheng, Z.; Song, C.; Pan, F. Conductance quantization in a Ag filament-based polymer resistive memory. *Nanotechnology* **2013**, *24*.

65. Pearson, C.; Bowen, L.; Lee, M.W.; Fisher, A.L.; Linton, K.E.; Bryce, M.R.; Petty, M.C. Focused ion beam and field-emission microscopy of metallic filaments in memory devices based on thin films of an ambipolar organic compound consisting of oxadiazole, carbazole, and fluorene units. *Appl. Phys. Lett.* **2013**, *102*.

66. Peng, P.; Xie, D.; Yang, Y.; Zang, Y.; Gao, X.; Zhou, C.; Feng, T.; Tian, H.; Ren, T.; Zhang, X. Resistive switching behavior in diamond-like carbon films grown by

pulsed laser deposition for resistance switching random access memory application. *J. Appl. Phys.* **2012**, *111*.

67. Wang, Z.; Griffin, P.B.; McVittie, J.; Wong, S.; McIntyre, P.C.; Nishi, Y. Resistive Switching Mechanism in <formula formulatype="inline"><tex>$\hbox{Zn}_{x}\hbox{Cd}_{1 - x}\hbox{S}$</tex></formula> Nonvolatile Memory Devices. *IEEE Electron Device Lett.* **2007**, *28*, 14–16.

68. Razi, P.M.; Gangineni, R.B. Compliance current and film thickness influence upon multi-level threshold resistive switching of amorphous BaTiO3 (am-BTO) films in Ag/am-BTO/Ag cross point structures. *Thin Solid Film -submitted* **2019**, *685*, 59–65.

69. Presented, A.D.; Wang, J. PROBING LOCAL VACANCY-DRIVEN RESISTIVE SWITCHING IN METAL OXIDE NANOSTRUCTURES. **2018**.

70. Torrezan, A.C.; Strachan, J.P.; Medeiros-Ribeiro, G.; Williams, R.S. Sub-nanosecond switching of a tantalum oxide memristor. *Nanotechnology* **2011**, *22*.

71. Govoreanu, B.; Kar, G.S.; Chen, Y.Y.; Paraschiv, V.; Kubicek, S.; Fantini, A.; Radu, I.P.; Goux, L.; Clima, S.; Degraeve, R.; et al. 10×10nm 2 Hf/HfO x crossbar resistive RAM with excellent performance, reliability and low-energy operation. *Tech. Dig. - Int. Electron Devices Meet. IEDM* **2011**, 31.6.1-31.6.4.

72. Presented, A.D.; Wang, J. PROBING LOCAL VACANCY-DRIVEN RESISTIVE SWITCHING IN METAL OXIDE NANOSTRUCTURES. **2018**.

73. Huang, Y.; Luo, Y.; Shen, Z.; Yuan, G.; Zeng, H. Unipolar resistive switching of ZnO-single-wire memristors. *Nanoscale Res. Lett.* **2014**, *9*, 1–5.

74. Akinaga, H.; Shima, H. Resistive random access memory (ReRAM) based on metal oxides. *Proc. IEEE* **2010**, *98*, 2237–2251.

75. Yan, Z.B.; Li, S.Z.; Wang, K.F.; Liu, J.M. Unipolar resistive switching effect in YMn1-δ O 3 thin films. *Appl. Phys. Lett.* **2010**, *96*, 1–4.

76. Wang, J.; Li, L.; Huyan, H.; Pan, X.; Nonnenmann, S.S. Highly Uniform Resistive Switching in HfO2 Films Embedded with Ordered Metal Nanoisland Arrays. *Adv. Funct. Mater.* **2019**, *29*, 1–11.

77. Kwon, D.-H.; Kim, K.M.; Jang, J.H.; Jeon, J.M.; Lee, M.H.; Kim, G.H.; Li, X.-S.; Park, G.-S.; Lee, B.; Han, S.; et al. Atomic structure of conducting nanofilaments in TiO2 resistive switching memory. *Nat. Nanotechnol.* **2010**, *5*, 148–53.

78. Privitera, S.; Bersuker, G.; Butcher, B.; Kalantarian, A.; Lombardo, S.; Bongiorno, C.; Geer, R.; Gilmer, D.C.; Kirsch, P.D. Microscopy study of the conductive filament in HfO2 resistive switching memory devices. *Microelectron. Eng.* **2013**, *109*, 75–78.

79. Jalili, N.; Laxminarayana, K. A review of atomic force microscopy imaging systems: Application to molecular metrology and biological sciences. *Mechatronics* **2004**, *14*, 907–945.

80. Magonov, S.N.; Elings, V.; Whangbo, M.H. Phase imaging and stiffness in tapping-mode atomic force microscopy. *Surf. Sci.* 1997, *375*.

81. Abelmann, L. Magnetic Force Microscopy. *Encycl. Spectrosc. Spectrom.* **2016**, 675–684.

82. Kolewe, K.W.; Zhu, J.; Mako, N.R.; Nonnenmann, S.S.; Schiffman, J.D. Bacterial Adhesion Is Affected by the Thickness and Stiffness of Poly(ethylene glycol)

Hydrogels. *ACS Appl. Mater. Interfaces* **2018**, *10*, 2275–2281.

83. Westra, K.L.; Thomson, D.J. The microstructure of thin films observed using atomic force microscopy. *Thin Solid Films* **1995**, *257*, 15–21.

84. Zhu, J.; Lee, J.W.; Lee, H.; Xie, L.; Pan, X.; De Souza, R.A.; Eom, C.B.; Nonnenmann, S.S. Probing vacancy behavior across complex oxide heterointerfaces. *Sci. Adv.* **2019**, *5*, 1–10.

85. Hensling, F.V.E.; Keeble, D.J.; Zhu, J.; Brose, S.; Xu, C.; Gunkel, F.; Danylyuk, S.; Nonnenmann, S.S.; Egger, W.; Dittmann, R. UV radiation enhanced oxygen vacancy formation caused by the PLD plasma plume. *Sci. Rep.* **2018**, *8*, 4–10.

86. Nonnenmann, S.S.; Kungas, R.; Vohs, J.; Bonnell, D.A. Direct in situ probe of electrochemical processes in operating fuel cells. *ACS Nano* **2013**, *7*, 6330–6336.

87. Kalinin, S. V.; Bonnell, D.A. Screening phenomena on oxide surfaces and its implications for local electrostatic and transport measurements. *Nano Lett.* **2004**, *4*, 555–560.

88. Eom, C.-B.; Wu, D.; Gruverman, A.; Lu, H.; Folkman, C.M.; Zhuravlev, M.Y.; Tsymbal, E.Y.; Jang, H.W.; Felker, D.; Wang, Y.; et al. Tunneling Electroresistance Effect in Ferroelectric Tunnel Junctions at the Nanoscale. *Nano Lett.* **2009**, *9*, 3539–3543.

89. Jang, H.W.; Ortiz, D.; Baek, S.H.; Folkman, C.M.; Das, R.R.; Shafer, P.; Chen, Y.; Nelson, C.T.; Pan, X.; Ramesh, R.; et al. Domain engineering for enhanced ferroelectric properties of epitaxial (001) BiFeO thin films. *Adv. Mater.* **2009**, *21*, 817–823.

90. Zhu, J. Quantitative Probing of Vacancies and Ions Dynamics in. **2019**.

91. Wang, J.; Nonnenmann, S.S. Area-dependent electroforming and switching polarity reversal across TiO2/Nb:SrTiO3 oxide interfaces. *J. Mater. Sci.* **2017**, *52*, 6469–6475.

92. Walker, D.J.F.; Martz, E.; Holmes, D.E.; Zhou, Z.; Nonnenmann, S.S.; Lovley, D.R. The Archaellum of Methanospirillum hungatei Is Electrically Conductive . *MBio* **2019**, *10*, 1–6.

93. Hou, J.; Rouxel, B.; Qin, W.; Nonnenmann, S.S.; Bonnell, D.A. Tip loading effects on AFM-based transport measurements of metal-oxide interfaces. *Nanotechnology* **2013**, *24*.

94. Lanza, M.; Wong, H.S.P.; Pop, E.; Ielmini, D.; Strukov, D.; Regan, B.C.; Larcher, L.; Villena, M.A.; Yang, J.J.; Goux, L.; et al. Recommended Methods to Study Resistive Switching Devices. *Adv. Electron. Mater.* **2019**, *5*, 1–28.

95. Tsuchiya, H.; Schmuki, P. Self-organized high aspect ratio porous hafnium oxide prepared by electrochemical anodization. *Electrochem. commun.* **2005**, *7*, 49–52.

96. Sieber, I. V; Schmuki, P. Porous Tantalum Oxide Prepared by Electrochemical Anodic Oxidation. *J. Electrochem. Soc.* **2005**, *152*, C639--C644.

97. Su, Z.; Zhou, W. Formation mechanism of porous anodic aluminium and titanium oxides. *Adv. Mater.* **2008**, *20*, 3663–3667.

98. Wu, C.-G.; Bein, T. Conducting Carbon Wires in Ordered, Nanometer-Sized Channels. *Science (80-.).* **1994**, *266*, 1013–1015.

99. Weitkamp, J. Zeolites and catalysis. *Solid State Ionics* **2000**, *131*, 175–188.

100. Deng, G.; Qiang, Z.; Lecorchick, W.; Cavicchi, K.A.; Vogt, B.D. Nanoporous nonwoven fibril-like morphology by cooperative self-assembly of poly(ethylene

oxide)- block -poly(ethyl acrylate)- block -polystyrene and phenolic resin. *Langmuir* **2014**, *30*, 2530–2540.

101. Yang, H.; Guo, L.; Wang, Z.; Yan, N.; Wang, Y. Nanoporous Films with Superior Resistance to Protein Adsorption by Selective Swelling of Polystyrene-block-poly(ethylene oxide). *Ind. Eng. Chem. Res.* **2016**, *55*, 8133–8140.

102. Tonucci, R.J.; Justus, B.L.; Campillo, a J.; Ford, C.E. Nanochannel array glass. *Science (80-.).* **1992**, *258*, 783–785.

103. Keller, F.; Hunter, M.S.; Robinson, D.L. Structural Features of Oxide Coatings on Aluminum. *J. Electrochem. Soc.* **1953**, *100*, 411.

104. Masuda, H.; Fukuda, K. Ordered metal nanohole arrays made by a two-step replication of honeycomb str ... *Science (80-.).* **1995**, *268*, 1466–1468.

105. Qiu, X.; Howe, J.Y.; Meyer, H.M.; Tuncer, E.; Paranthaman, M.P. Thermal stability of HfO2nanotube arrays. *Appl. Surf. Sci.* **2011**, *257*, 4075–4081.

106. Wang, N.; Li, H.; Wang, J.; Chen, S.; Ma, Y.; Zhang, Z. Study on the anticorrosion, biocompatibility, and osteoinductivity of tantalum decorated with tantalum oxide nanotube array films. *ACS Appl. Mater. Interfaces* **2012**, *4*, 4516–4523.

107. Wei, W.; Macak, J.M.; Schmuki, P. High aspect ratio ordered nanoporous Ta2O5 films by anodization of Ta. *Electrochem. commun.* **2008**, *10*, 428–432.

108. Su, Z.; Grigorescu, S.; Wang, L.; Lee, K.; Schmuki, P. Fast fabrication of Ta2O5 nanotube arrays and their conversion to Ta3N5for efficient solar driven water splitting. *Electrochem. commun.* **2015**, *50*, 15–19.

109. Gonçalves, R. V.; Migowski, P.; Wender, H.; Eberhardt, D.; Weibel, D.E.;

Sonaglio, F.C.; Zapata, M.J.M.; Dupont, J.; Feil, A.F.; Teixeira, S.R. Ta 2O 5 nanotubes obtained by anodization: Effect of thermal treatment on the photocatalytic activity for hydrogen production. *J. Phys. Chem. C* **2012**, *116*, 14022–14030.

110. Paulose, M.; Varghese, O.K.; Mor, G.K.; Grimes, C.A.; Ong, K.G. Unprecedented ultra-high hydrogen gas sensitivity in undoped titania nanotubes. *Nanotechnology* **2006**, *17*, 398–402.

111. Macák, J.M.; Tsuchiya, H.; Schmuki, P. High-aspect-ratio TiO2 nanotubes by anodization of titanium. *Angew. Chemie - Int. Ed.* **2005**, *44*, 2100–2102.

112. Macák, J.M.; Tsuchiya, H.; Ghicov, A.; Schmuki, P. Dye-sensitized anodic TiO2nanotubes. *Electrochem. commun.* **2005**, *7*, 1133–1137.

113. Stępniowski, W.J.; Salerno, M. Fabrication of nanowires and nanotubes by anodic alumina template-assisted electrodeposition. In *Manufacturing nanostructures*; 2014; pp. 321–357 ISBN 9781910086070.

114. Jaafar, M.; Navas, D.; Hernández-Vélez, M.; Baldonedo, J.L.; Vázquez, M.; Asenjo, A. Nanoporous alumina membrane prepared by nanoindentation and anodic oxidation. *Surf. Sci.* **2009**, *603*, 3155–3159.

115. Liu, C.Y.; Datta, A.; Wang, Y.L. Ordered anodic alumina nanochannels on focused-ion-beam-prepatterned aluminum surfaces. *Appl. Phys. Lett.* **2001**, *78*, 120–122.

116. Martín, J.; Manzano, C. V.; Martín-González, M. In-depth study of self-ordered porous alumina in the 140-400 nm pore diameter range. *Microporous Mesoporous Mater.* **2012**, *151*, 311–316.

117. Nielsch, K.; Choi, J.; Schwirn, K.; Wehrspohn, R.B.; Gösele, U. Self-ordering Regimes of Porous Alumina: The 10 Porosity Rule. *Nano Lett.* **2002**, *2*, 677–680.

118. Zhang, J.; Kielbasa, J.E.; Carroll, D.L. Controllable fabrication of porous alumina templates for nanostructures synthesis. *Mater. Chem. Phys.* **2010**, *122*, 295–300.

119. Wang, X.; Han, G.-R. Fabrication and characterization of anodic aluminum oxide template. *Microelectron. Eng.* **2003**, *66*, 166–170.

120. Hu, G.; Zhang, H.; Di, W.; Zhao, T. Study on Wet Etching of AAO Template. *Carbon Nanotub.* **2004**, *1*, 78–82.

121. Lyu, S.-H.; Lee, J.-S. Highly scalable resistive switching memory cells using pore-size-controlled nanoporous alumina templates. *J. Mater. Chem.* **2012**, *22*, 1852–1861.

122. Xiong, G.; Elam, J.W.; Feng, H.; Han, C.Y.; Wang, H.-H.; Iton, L.E.; Curtiss, L.A.; Pellin, M.J.; Kung, M.; Kung, H.; et al. Effect of atomic layer deposition coatings on the surface structure of anodic aluminum oxide membranes. *J. Phys. Chem. B* **2005**, *109*, 14059–14063.

123. Ritala, M.; Kukli, K.; Rahtu, A.; Raisanen, P.I.; Leskela, M.; Sajavaara, T.; Keinonen, J.; Schulz, M.; Packan, P.A.; Muller, D.A.; et al. Atomic layer deposition of oxide thin films with metal alkoxides as oxygen sources. *Science* **2000**, *288*, 319–21.

124. Pellin, M.J.; Stair, P.C.; Xiong, G.; Elam, J.W.; Birrell, J.; Curtiss, L.; George, S.M.; Han, C.Y.; Iton, L.; Kung, H.; et al. Mesoporous catalytic membranes: Synthetic control of pore size and wall composition. *Catal. Letters* **2005**, *102*, 127–130.

125. Sulka, G.D.; Zaraska, L.; Stępniowski, W.J. Anodic porous alumina as a template for nanofabrication. *Encycl. Nanosci. Nanotechnol.* **2011**, *11*, 261–349.

126. Lee, W.; Park, S.-J. Porous Anodic Aluminum Oxide: Anodization and Templated Synthesis of Functional Nanostructures. *Chem. Rev.* **2014**, *114*, 7487–7556.

127. Poinern, G.E.J.; Ali, N.; Fawcett, D. *Progress in nano-engineered anodic aluminum oxide membrane development*; 2010; Vol. 4; ISBN 6189360289.

128. Santos, A.; Kumeria, T.; Losic, D. Nanoporous anodic aluminum oxide for chemical sensing and biosensors. *TrAC - Trends Anal. Chem.* **2013**, *44*, 25–38.

129. Masuda, H.; Satoh, M. Fabrication of gold nanodot array using anodic porous alumina as an evaporation mask. *Japanese J. Appl. Physics, Part 2 Lett.* **1996**, *35*.

130. Liang, J.; Chik, H.; Yin, A.; Xu, J. Two-dimensional lateral superlattices of nanostructures: Nonlithographic formation by anodic membrane template. *J. Appl. Phys.* **2002**, *91*, 2544–2546.

131. Lei, Y.; Chim, W.K. Shape and size control of regularly arrayed nanodots fabricated using ultrathin alumina masks. *Chem. Mater.* **2005**, *17*, 580–585.

132. Malinovskis, U.; Poplausks, R.; Apsite, I.; Meija, R.; Prikulis, J.; Lombardi, F.; Erts, D. Ultrathin anodic aluminum oxide membranes for production of dense sub-20 nm nanoparticle arrays. *J. Phys. Chem. C* **2014**, *118*, 8685–8690.

133. Li, Z.; Wang, Y.; Tian, G.; Li, P.; Zhao, L.; Zhang, F.; Yao, J.; Fan, H.; Song, X.; Chen, D.; et al. High-density array of ferroelectric nanodots with robust and reversibly switchable topological domain states. *Sci. Adv.* **2017**, *3*, e1700919.

134. Wang, Z.J.; Bai, Y. Resistive Switching Behavior in Ferroelectric Heterostructures. *Small* **2019**, *15*, 1–13.

135. Lee, W.; Han, H.; Lotnyk, A.; Schubert, M.A.; Senz, S.; Alexe, M.; Hesse, D.; Baik, S.; Gösele, U. Individually addressable epitaxial ferroelectric nanocapacitor arrays with near Tb inch-2 density. *Nat. Nanotechnol.* **2008**, *3*, 402–407.

136. Gao, X.; Liu, L.; Birajdar, B.; Ziese, M.; Lee, W.; Alexe, M.; Hesse, D. High-density periodically ordered magnetic cobalt ferrite nanodot arrays by template-assisted pulsed laser deposition. *Adv. Funct. Mater.* **2009**, *19*, 3450–3455.

137. Nielsch, K.; Wehrspohn, R.B.; Barthel, J.; Kirschner, J.; G??sele, U.; Fischer, S.F.; Kronm??ller, H. Hexagonally ordered 100 nm period nickel nanowire arrays. *Appl. Phys. Lett.* **2001**, *79*, 1360–1362.

138. Perre, E.; Nyholm, L.; Gustafsson, T.; Taberna, P.L.; Simon, P.; Edström, K. Direct electrodeposition of aluminium nano-rods. *Electrochem. commun.* **2008**, *10*, 1467–1470.

139. Cheah, S.K.; Perre, E.; Rooth, M.; Fondell, M.; Hårsta, A.; Nyholm, L.; Boman, M.; Gustafsson, T.; Lu, J.; Simon, P.; et al. Self-Supported three-dimensional nanoelectrodes for microbattery applications. *Nano Lett.* **2009**, *9*, 3230–3233.

140. Zhang, Z.; Sun, X.; Dresselhaus, M.S.; Ying, J.; Heremans, J. Electronic transport properties of single-crystal bismuth nanowire arrays. *Phys. Rev. B* **2000**, *61*, 4850–4861.

141. Wu, Y.; Gu, Q.; Ding, G.; Tong, F.; Hu, Z.; Jonas, A.M. Confinement induced preferential orientation of crystals and enhancement of properties in ferroelectric polymer nanowires. *ACS Macro Lett.* **2013**, *2*, 535–538.

142. Dubois, J.-C. Ferroelectric polymers: Chemistry, physics, and applications. Edited by Hari Singh Nalwa, Marcel Dekker, New York 1995, XII, 895 pp., hardcover,

$225.00, ISBN 0-8247-9468-0. *Adv. Mater.* **1996**, *8*, 542–542.

143. Steinhart, M.; Jia, Z.; Schaper, A.K.; Wehrspohn, R.B.; Gösele, U.; Wendorff, J.H. Palladium nanotubes with tailored wall morphologies. *Adv. Mater.* **2003**, *15*, 706–709.

144. Favier, F.; Walter, E.C.; Zach, M.P.; Benter, T.; Penner, R.M. Hydrogen sensors and switches from electrodeposited palladium mesowire arrays. *Science* **2001**, *293*, 2227–2231.

145. Niwa, S. -i. A One-Step Conversion of Benzene to Phenol with a Palladium Membrane. *Science (80-.).* **2002**, *295*, 105–107.

146. Md Jani, A.M.; Losic, D.; Voelcker, N.H. Nanoporous anodic aluminium oxide: Advances in surface engineering and emerging applications. *Prog. Mater. Sci.* **2013**, *58*, 636–704.

147. La Flamme, K.E.; Popat, K.C.; Leoni, L.; Markiewicz, E.; La Tempa, T.J.; Roman, B.B.; Grimes, C.A.; Desai, T.A. Biocompatibility of nanoporous alumina membranes for immunoisolation. *Biomaterials* **2007**, *28*, 2638–2645.

148. Popat, K.C.; Leary Swan, E.E.; Mukhatyar, V.; Chatvanichkul, K.I.; Mor, G.K.; Grimes, C.A.; Desai, T.A. Influence of nanoporous alumina membranes on long-term osteoblast response. *Biomaterials* **2005**, *26*, 4516–4522.

149. Simovic, S.; Losic, D.; Vasilev, K. Controlled drug release from porous materials by plasma polymer deposition. *Chem. Commun. (Camb).* **2010**, *46*, 1317–9.

150. Lu, H.F.; Li, F.; Liu, G.; Chen, Z.-G.; Wang, D.-W.; Fang, H.-T.; Lu, G.Q.; Jiang, Z.H.; Cheng, H.-M. Amorphous TiO_2 nanotube arrays for low-temperature oxygen sensors. *Nanotechnology* **2008**, *19*, 405504.

151. Yip, C.T.; Huang, H.; Zhou, L.; Xie, K.; Wang, Y.; Feng, T.; Li, J.; Tam, W.Y. Direct and seamless coupling of TiO2nanotube photonic crystal to dye-sensitized solar cell: A single-step approach. *Adv. Mater.* **2011**, *23*, 5624–5628.

152. Cui, H.; Zhu, G.; Xie, Y.; Zhao, W.; Yang, C.; Lin, T.; Gu, H.; Huang, F. Black nanostructured Nb_2O_5 with improved solar absorption and enhanced photoelectrochemical water splitting. *J. Mater. Chem. A* **2015**, *3*, 11830–11837.

153. Baik, J.-S.; Yun, G.; Balamurugan, M.; Lee, S.K.; Kim, J.-H.; Ahn, K.-S.; Kang, S.H. Hydrogen Treated Niobium Oxide Nanotube Arrays for Photoelectrochemical Water Oxidation. *J. Electrochem. Soc.* **2016**, *163*, H1165–H1170.

154. Zwilling, V.; Aucouturier, M.; Darque-Ceretti, E. Anodic oxidation of titanium and TA6V alloy in chromic media. An electrochemical approach. *Electrochim. Acta* **1999**, *45*, 921–929.

155. Tang, H.; Prasad, K.; Sanjinès, R.; Schmid, P.E.; Lévy, F. Electrical and optical properties of TiO_2 anatase thin films. *J. Appl. Phys.* **1994**, *75*, 2042–2047.

156. Shankar, K.; Mor, G.K.; Prakasam, H.E.; Yoriya, S.; Paulose, M.; Varghese, O.K.; Grimes, C.A. Highly-ordered TiO2 nanotube arrays up to 220 μm in length: Use in water photoelectrolysis and dye-sensitized solar cells. *Nanotechnology* **2007**, *18*.

157. O'Regan, B.; Gratzel, M. A Low-Cost, High-Efficiency Solar-Cell Based on Dye-Sensitized Colloidal TiO_2 Films. *Nature* **1991**, *353*, 737–740.

158. Ito, S.; Ha, N.L.C.; Rothenberger, G.; Liska, P.; Comte, P.; Zakeeruddin, S.M.; P??chy, P.; Nazeeruddin, M.K.; Gr??tzel, M. High-efficiency (7.2%) flexible dye-sensitized solar cells with Ti-metal substrate for nanocrystalline-TiO2 photoanode. *Chem. Commun.* **2006**, 4004–4006.

159. Ye, M.; Gong, J.; Lai, Y.; Lin, C.; Lin, Z. High-efficiency photoelectrocatalytic hydrogen generation enabled by palladium quantum dots-sensitized TiO 2 nanotube arrays. *J. Am. Chem. Soc.* **2012**, *134*, 15720–15723.

160. Yang, J.J.; Pickett, M.D.; Li, X.; Ohlberg, D.A.A.; Stewart, D.R.; Williams, R.S. Memristive switching mechanism for metal/oxide/metal nanodevices. *Nat. Nanotechnol.* **2008**, *3*, 429–433.

161. Gergel-hackett, N.; Hamadani, B.; Dunlap, B.; Suehle, J.; Member, S.; Richter, C.; Member, S.; Hacker, C.; Gundlach, D.; Abstract, A. A Flexible Solution-Processed Memristor. *IEEE Electron Device Lett.* **2009**, *30*, 706–708.

162. Gale, E. TiO2-based memristors and ReRAM: Materials, mechanisms and models (a review). *Semicond. Sci. Technol.* 2014, *29*.

163. Chaneliere, C.; Autran, J.L.; Devine, R.A.B.; Balland, B. Tantalum pentoxide (Ta2O5) thin films for advanced dielectric applications. *Mater. Sci. Eng. R Reports* **1998**, *22*, 269–322.

164. Takahara, Y.; Kondo, J.N.; Takata, T.; Lu, D.; Domen, K. Mesoporous tantalum oxide. 1. Characterization and photocatalytic activity for the overall water decomposition. *Chem. Mater.* **2001**, *13*, 1194–1199.

165. Kim, Y.B.; Lee, S.R.; Lee, D.; Lee, C.B.; Chang, M.; Hur, J.H.; Lee, M.J.; Park, G.S.; Kim, C.J.; Chung, U.I.; et al. Bi-layered RRAM with unlimited endurance and extremely uniform switching. *Dig. Tech. Pap. - Symp. VLSI Technol.* **2011**, 52–53.

166. Kim, K.M.; Lee, S.R.; Kim, S.; Chang, M.; Hwang, C.S. Self-Limited switching in Ta2 O5 /TaOx memristors exhibiting uniform multilevel changes in resistance.

Adv. Funct. Mater. **2015**, *25*, 1527–1534.

167. Matsuno, H.; Yokoyama, A.; Watari, F.; Uo, M.; Kawasaki, T. Biocompatibility and osteogenesis of refractory metal implants, titanium, hafnium, niobium, tantalum and rhenium. *Biomaterials* **2001**, *22*, 1253–1262.

168. Niinomi, M. Mechanical properties of biomedical titanium alloys. *Mater. Sci. Eng. A243* **1998**, *243*, 231–236.

169. Minagar, S.; Berndt, C.C.; Wang, J.; Ivanova, E.; Wen, C. A review of the application of anodization for the fabrication of nanotubes on metal implant surfaces. *Acta Biomater.* **2012**, *8*, 2875–2888.

170. Yasuda, K.; Schmuki, P.; Yasuda, B.K. Formation of Self-Organized Zirconium Titanate Nanotube Layers by Alloy Anodization. *Adv. Mater.* **2007**, *19*, 1757–1760.

171. Yasuda, K.; Schmuki, P. Electrochemical formation of self-organized zirconium titanate nanotube multilayers. *Electrochem. commun.* **2007**, *9*, 615–619.

172. Tsuchiya, H.; MacAk, J.M.; Taveira, L.; Schmuki, P. Fabrication and characterization of smooth high aspect ratio zirconia nanotubes. *Chem. Phys. Lett.* **2005**, *410*, 188–191.

173. Tsuchiya, H.; Macak, J.M.; Ghlcov, A.; Schmuki, P. Self-organization of anodic nanotubes on two size scales. *Small* **2006**, *2*, 888–891.

174. Rahman, M.T.; Shams, N.N.; Lai, C.H.; Fidler, J.; Suess, D. Co/Pt perpendicular antidot arrays with engineered feature size and magnetic properties fabricated on anodic aluminum oxide templates. *Phys. Rev. B - Condens. Matter Mater. Phys.* **2010**, *81*, 1–7.

175. Rahman, M.T.; Liu, X.; Morisako, A. TbFeCo perpendicular magnetic recording media deposited on nanohole arrays of porous alumina layer. *J. Appl. Phys.* **2006**, *99*.

176. Xiao, Z.L.; Han, C.Y.; Welp, U.; Wang, H.H.; Vlasko-Vlasov, V.K.; Kwok, W.K.; Miller, D.J.; Hiller, J.M.; Cook, R.E.; Willing, G.A.; et al. Nickel antidot arrays on anodic alumina substrates. *Appl. Phys. Lett.* **2002**, *81*, 2869–2871.

177. Diefeng Gu, Helmut Baumgart, T.M.A.-F. and G.N. Synthesis of Nested Coaxial Multiple- Walled Nanotubes by Atomic Layer. *ACS Nano* **2010**, *4*, 753–758.

178. Chuang, V.P.; Jung, W.; Ross, C.A.; Cheng, J.Y.; Park, O.H.; Kim, H.C. Multilayer magnetic antidot arrays from block copolymer templates. *J. Appl. Phys.* **2008**, *103*.

179. Wang, C.C.; Adeyeye, A.O.; Singh, N. Magnetic and transport properties of multilayer nanoscale antidot arrays. *Appl. Phys. Lett.* **2006**, *88*, 2004–2007.

180. Castaño, F.J.; Nielsch, K.; Ross, C.A.; Robinson, J.W.A.; Krishnan, R. Anisotropy and magnetotransport in ordered magnetic antidot arrays. *Appl. Phys. Lett.* **2004**, *85*, 2872–2874.

181. Cowburn, R.P.; Adeyeye, A.O.; Bland, J.A.C. Magnetic switching and uniaxial anisotropy in lithographically defined anti-dot Permalloy arrays. *J. Magn. Magn. Mater.* **1997**, *173*, 193–201.

182. Adeyeye, A.O.; Bland, J.A.C.; Daboo, C. Magnetic properties of arrays of “holes” in Ni80Fe20films. *Appl. Phys. Lett.* **1997**, *70*, 3164–3166.

183. Rahman, M.T.; Shams, N.N.; Lai, C.H. A large-area mesoporous array of magnetic nanostructure with perpendicular anisotropy integrated on Si wafers.

Nanotechnology **2008**, *19*.

184. Zang, K.Y.; Wang, Y.D.; Wang, L.S.; Tripathy, S.; Chua, S.J.; Thompson, C. V. Nanoheteroepitaxy of GaN on a nanopore array of Si(111) surface. *Thin Solid Films* **2007**, *515*, 4505–4508.

185. Cheng, G.; Moskovits, M. A highly regular two-dimensional array of Au quantum dots deposited in a periodically nanoporous GaAs epitaxial layer. *Adv. Mater.* **2002**, *14*, 1567–1570.

186. Tian, G.; Zhao, L.; Lu, Z.; Yao, J.; Fan, H.; Fan, Z.; Li, Z.; Li, P.; Chen, D.; Zhang, X.; et al. Fabrication of high-density BiFeO 3 nanodot and anti-nanodot arrays by anodic alumina template-assisted ion beam etching. *Nanotechnology* **2016**, *27*, 485302.

187. Nakao, M.; Oku, S.; Tanaka, H.; Shibata, Y.; Yokoo, A.; Tamamura, T.; Masuda, H. Fabrication of GaAs hole array as a 2D-photonic crystal and their application to photonic bandgap waveguide. *Opt. Quantum Electron.* **2002**, *34*, 183–193.

188. Masuda, H.; Watanabe, M.; Yasui, K.; Tryk, D.; Rao, T.; Fujishima, A. Fabrication of a Nanostructured Diamond Honeycomb Film. *Adv. Mater.* **2000**, *12*, 444–447.

189. Shingubara, S.; Okino, O.; Murakami, Y.; Sakaue, H.; Takahagi, T. Fabrication of nanohole array on Si using self-organized porous alumina mask. *J. Vac. Sci. Technol. B Microelectron. Nanom. Struct.* **2001**, *19*, 1901.

190. Wang, Y.D.; Chua, S.J.; Sander, M.S.; Chen, P.; Tripathy, S.; Fonstad, C.G. Fabrication and properties of nanoporous GaN films. *Appl. Phys. Lett.* **2004**, *85*, 816–818.

191. Nakao, M.; Oku, S.; Tamamura, T.; Yasui, K.; Masuda, H. GaAs and InP Nanohole Arrays Fabricated by Reactive Beam Etching Using Highly Ordered Alumina Membranes. *Japanese J. Appied Phys.* **1999**, *38*, 1052–1055.

192. Honda, K.; Rao, T.N.; Tryk, D.A.; Fujishima, A.; Watanabe, M.; Yasui, K.; Masuda, H. Impedance Characteristics of the Nanoporous Honeycomb Diamond Electrodes for Electrical Double-Layer Capacitor Applications. *J. Electrochem. Soc.* **2001**, *148*, A668.

193. Tian, L.; Ram, K.B.; Ahmad, I.; Menon, L.; Holtz, M. Optical properties of a nanoporous array in silicon. *J. Appl. Phys.* **2005**, *97*.

194. Kanamori, Y.; Hane, K.; Sai, H.; Yugami, H. 100 Nm Period Silicon Antireflection Structures Fabricated Using a Porous Alumina Membrane Mask. *Appl. Phys. Lett.* **2001**, *78*, 142–143.

195. Yanagishita, T.; Nishio, K.; Masuda, H. Fabrication of metal nanohole arrays with high aspect ratios using two-step replication of anodic porous alumina. *Adv. Mater.* **2005**, *17*, 2241–2243.

196. Yanagishita, T.; Nishio, K.; Masuda, H. Polymer through-hole membrane fabricated by nanoimprinting using metal molds with high aspect ratios. *J. Vac. Sci. Technol. B Microelectron. Nanom. Struct.* **2007**, *25*, L35.

197. Yanagishita, T.; Nishio, K.; Masuda, H. Nanoimprinting using Ni molds prepared from highly ordered anodic porous alumina templates. *Japanese J. Appl. Physics, Part 2 Lett.* **2006**, *45*.

198. Haberkorn, N.; Gutmann, J.S.; Theato, P. Template-Assisted Fabrication of Free-Triphenylamine Derivative : Toward Ordered Bulk-Heterojunction Solar Cells.

ACS Nano **2009**, *3*, 1415–1422.

199. Martín, J.; Martín-González, M.; del Campo, A.; Reinosa, J.J.; Fernández, J.F. Ordered arrays of polymeric nanopores by using inverse nanostructured PTFE surfaces. *Nanotechnology* **2012**, *23*, 385305.

200. Grimm, S.; Giesa, R.; Sklarek, K.; Langner, A. Nondestructive Replication of Self-Ordered Nanoporous Alumina Membranes via Cross-Linked Polyacrylate Nanofiber Arrays 2008. **2008**.

201. Zhuo, V.Y.Q.; Jiang, Y.; Li, M.H.; Chua, E.K.; Zhang, Z.; Pan, J.S.; Zhao, R.; Shi, L.P.; Chong, T.C.; Robertson, J. Band alignment between Ta2O5and metals for resistive random access memory electrodes engineering. *Appl. Phys. Lett.* **2013**, *102*, 1–6.

202. Kim, H.D.; An, H.M.; Lee, E.B.; Kim, T.G. Stable bipolar resistive switching characteristics and resistive switching mechanisms observed in aluminum nitride-based ReRAM devices. *IEEE Trans. Electron Devices* **2011**, *58*, 3566–3573.

203. Wang, C.; Jin, K.J.; Xu, Z.T.; Wang, L.; Ge, C.; Lu, H. Bin; Guo, H.Z.; He, M.; Yang, G.Z. Switchable diode effect and ferroelectric resistive switching in epitaxial BiFeO3 thin films. *Appl. Phys. Lett.* **2011**, *98*.

204. Nagashima, K.; Yanagida, T.; Oka, K.; Taniguchi, M.; Kawai, T.; Kim, J.S.; Park, B.H. Resistive switching multistate nonvolatile memory effects in a single cobalt oxide nanowire. *Nano Lett.* **2010**, *10*, 1359–1363.

205. Yang, Y.; Zhang, X.; Gao, M.; Zeng, F.; Zhou, W.; Xie, S.; Pan, F. Nonvolatile resistive switching in single crystalline ZnO nanowires. *Nanoscale* **2011**, *3*, 1917–1921.

206. Nonnenmann, S.S.; Gallo, E.M.; Spanier, J.E. Redox-based resistive switching in ferroelectric perovskite nanotubes. *Appl. Phys. Lett.* **2010**, *97*, 1–4.

207. Ageev, O.A.; Blinov, Y.F.; Il'in, O.I.; Konoplev, B.G.; Rubashkina, M. V.; Smirnov, V.A.; Fedotov, A.A. Study of the resistive switching of vertically aligned carbon nanotubes by scanning tunneling microscopy. *Phys. Solid State* **2015**, *57*, 825–831.

208. Choi, B.J.; Jeong, D.S.; Kim, S.K.; Rohde, C.; Choi, S.; Oh, J.H.; Kim, H.J.; Hwang, C.S.; Szot, K.; Waser, R.; et al. Resistive switching mechanism of TiO 2 thin films grown by atomic-layer deposition. *J. Appl. Phys.* **2005**, *98*.

209. Muenstermann, R.; Menke, T.; Dittmann, R.; Waser, R. Coexistence of filamentary and homogeneous resistive switching in Fe-doped SrTiO3 thin-film memristive devices. *Adv. Mater.* **2010**, *22*, 4819–4822.

210. Guan, W.; Long, S.; Jia, R.; Liu, M. Nonvolatile resistive switching memory utilizing gold nanocrystals embedded in zirconium oxide. *Appl. Phys. Lett.* **2007**, *91*.

211. Chang, W.Y.; Cheng, K.J.; Tsai, J.M.; Chen, H.J.; Chen, F.; Tsai, M.J.; Wu, T.B. Improvement of resistive switching characteristics in TiO2 thin films with embedded Pt nanocrystals. *Appl. Phys. Lett.* **2009**, *95*.

212. Chen, L.; Gou, H.Y.; Sun, Q.Q.; Zhou, P.; Lu, H.L.; Wang, P.F.; Ding, S.J.; Zhang, D. Enhancement of resistive switching characteristics in Al2O 3-Based RRAM with embedded ruthenium nanocrystals. *IEEE Electron Device Lett.* **2011**, *32*, 794–796.

213. Jang, J.; Pan, F.; Braam, K.; Subramanian, V. Resistance switching characteristics

of solid electrolyte chalcogenide Ag2Se nanoparticles for flexible nonvolatile memory applications. *Adv. Mater.* **2012**, *24*, 3573–3576.

214. Schmidt, D.O.; Hoffmann-Eifert, S.; Zhang, H.; La Torre, C.; Besmehn, A.; Noyong, M.; Waser, R.; Simon, U. Resistive Switching of Individual, Chemically Synthesized TiO2 Nanoparticles. *Small* **2015**, *11*, 6444–6456.

215. Yin, S.; Fujishiro, Y.; Wu, J.; Aki, M.; Sato, T. Synthesis and photocatalytic properties of fibrous titania by solvothermal reactions. *J. Mater. Process. Technol.* **2003**, *137*, 45–48.

216. Kang, M. Synthesis of Fe/TiO2 photocatalyst with nanometer size by solvothermal method and the effect of H2O addition on structural stability and photodecomposition of methanol. *J. Mol. Catal. A Chem.* **2003**, *197*, 173–183.

217. Kim, C.S.; Moon, B.K.; Park, J.H.; Chung, S.T.; Son, S.M. Synthesis of nanocrystalline TiO2 in toluene by a solvothermal route. *J. Cryst. Growth* **2003**, *254*, 405–410.

218. Charinpanitkul, T.; Faungnawakij, K.; Tanthapanichakoon, W. Review of Recent Research on Nanoparticle Production in Thailand. *Adv. Powder Technol.* **2008**, *19*, 443–457.

219. Gupta, S.M.; Tripathi, M. A review on the synthesis of TiO 2 nanoparticles by solution route. *Cent. Eur. J. Chem.* **2012**, *10*, 279–294.

220. Shin, Y.S.; Son, J.Y.; Jo, M.H.; Shin, Y.H.; Jang, H.M. High-mobility graphene nanoribbons prepared using polystyrene dip-pen nanolithography. *J. Am. Chem. Soc.* **2011**, *133*, 5623–5625.

221. Piner, R.D.; Zhu, J.; Xu, F.; Hong, S.; Mirkin, C.A. “Dip-Pen” Nanolithography.

Science (80-.). **1999**, *283*, 661–663.

222. Hu, Q.; Jung, S.M.; Lee, H.H.; Kim, Y.S.; Choi, Y.J.; Kang, D.H.; Kim, K.B.; Yoon, T.S. Resistive switching characteristics of maghemite nanoparticle assembly. *J. Phys. D. Appl. Phys.* **2011**, *44*.

223. Klajn, R.; Fialkowski, M.; Bensemann, I.T.; Bitner, A.; Campbell, C.J.; Bishop, K.; Smoukov, S.; Grzybowski, B.A. Multicolour micropatterning of thin films of dry gels. *Nat. Mater.* **2004**, *3*, 729–735.

224. Hall, D.B.; Underhill, P.; Torkelson, J.M. Spin coating of thin and ultrathin polymer films. *Polym. Eng. Sci.* **1998**, *38*, 2039–2045.

225. De Roo, J.; Zhou, Z.; Wang, J.; Deblock, L.; Crosby, A.J.; Owen, J.S.; Nonnenmann, S.S. Synthesis of Phosphonic Acid Ligands for Nanocrystal Surface Functionalization and Solution Processed Memristors. *Chem. Mater.* **2018**, *30*, 8034–8039.

226. Wang, J.; Choudhary, S.; De Roo, J.; De Keukeleere, K.; Van Driessche, I.; Crosby, A.J.; Nonnenmann, S.S. How Ligands Affect Resistive Switching in Solution-Processed HfO 2 Nanoparticle Assemblies. *ACS Appl. Mater. Interfaces* **2018**, acsami.7b17376.

227. Wang, J.; Choudhary, S.; Harrigan, W.L.; Crosby, A.J.; Kittilstved, K.R.; Nonnenmann, S.S. Transferable Memristive Nanoribbons Comprising Solution-Processed Strontium Titanate Nanocubes. *ACS Appl. Mater. Interfaces* **2017**, *9*, 10847–10854.

228. Kim, H.S.; Lee, C.H.; Sudeep, P.K.; Emrick, T.; Crosby, A.J. Nanoparticle stripes, grids, and ribbons produced by flow coating. *Adv. Mater.* **2010**, *22*, 4600–4604.

229. Yu, S.; Guan, X.; Wong, H.S.P. Conduction mechanism of TiNHfO xPt resistive switching memory: A trap-assisted-tunneling model. *Appl. Phys. Lett.* **2011**, *99*, 16–19.

230. Liu, Y.; Gibbs, M.; Puthussery, J.; Gaik, S.; Ihly, R.; Hillhouse, H.W.; Law, M. Dependence of carrier mobility on nanocrystal size and ligand length in pbse nanocrystal solids. *Nano Lett.* **2010**, *10*, 1960–1969.

231. Gao, Y.; Aerts, M.; Sandeep, C.S.S.; Talgorn, E.; Savenije, T.J.; Kinge, S.; Siebbeles, L.D.A.; Houtepen, A.J. Photoconductivity of PbSe quantum-dot solids: Dependence on ligand anchor group and length. *ACS Nano* **2012**, *6*, 9606–9614.

232. Sanehira, E.M.; Marshall, A.R.; Christians, J.A.; Harvey, S.P.; Ciesielski, P.N.; Wheeler, L.M.; Schulz, P.; Lin, L.Y.; Beard, M.C.; Luther, J.M. Enhanced mobility CsPbI3 quantum dot arrays for record-efficiency, high-voltage photovoltaic cells. *Sci. Adv.* **2017**, *3*.

233. Lan, X.; Voznyy, O.; García De Arquer, F.P.; Liu, M.; Xu, J.; Proppe, A.H.; Walters, G.; Fan, F.; Tan, H.; Liu, M.; et al. 10.6% Certified Colloidal Quantum Dot Solar Cells Via Solvent-Polarity-Engineered Halide Passivation. *Nano Lett.* **2016**, *16*, 4630–4634.

234. Ibáñez, M.; Luo, Z.; Genç, A.; Piveteau, L.; Ortega, S.; Cadavid, D.; Dobrozhan, O.; Liu, Y.; Nachtegaal, M.; Zebarjadi, M.; et al. High-performance thermoelectric nanocomposites from nanocrystal building blocks. *Nat. Commun.* **2016**, *7*, 1–7.

235. Wang, Y.; Fedin, I.; Zhang, H.; Talapin, D. V. Direct optical lithography of functional inorganic nanomaterials. *Science (80-.).* **2017**, *357*, 385–388.

236. Llordés, A.; Garcia, G.; Gazquez, J.; Milliron, D.J. Tunable near-infrared and

visible-light transmittance in nanocrystal-in-glass composites. *Nature* **2013**, *500*, 323–326.

237. Rijckaert, H.; Pollefeyt, G.; Sieger, M.; Hänisch, J.; Bennewitz, J.; De Keukeleere, K.; De Roo, J.; Hühne, R.; Bäcker, M.; Paturi, P.; et al. Optimizing Nanocomposites through Nanocrystal Surface Chemistry: Superconducting YBa2Cu3O7 Thin Films via Low-Fluorine Metal Organic Deposition and Preformed Metal Oxide Nanocrystals. *Chem. Mater.* **2017**, *29*, 6104–6113.

238. De Keukeleere, K.; Cayado, P.; Meledin, A.; Vallès, F.; De Roo, J.; Rijckaert, H.; Pollefeyt, G.; Bruneel, E.; Palau, A.; Coll, M.; et al. Superconducting YBa2Cu3O7–δ Nanocomposites Using Preformed ZrO2 Nanocrystals: Growth Mechanisms and Vortex Pinning Properties. *Adv. Electron. Mater.* **2016**, *2*, 1–9.

239. De Roo, J.; Van Driessche, I.; Martins, J.C.; Hens, Z. Colloidal metal oxide nanocrystal catalysis by sustained chemically driven ligand displacement. *Nat. Mater.* **2016**, *15*, 517–521.

240. Maan, A.K.; Jayadevi, D.A.; James, A.P. A survey of memristive threshold logic circuits. *IEEE Trans. Neural Networks Learn. Syst.* **2017**, *28*, 1734–1746.

241. Slesazeck, S.; Mähne, H.; Wylezich, H.; Wachowiak, A.; Radhakrishnan, J.; Ascoli, A.; Tetzlaff, R.; Mikolajick, T. Physical model of threshold switching in NbO_2 based memristors. *RSC Adv.* **2015**, *5*, 102318–102322.

242. Robertson, J. High dielectric constant oxides. *Eur. Phys. J. Appl. Phys.* **2004**, *28*, 265–291.

243. Beiu, V.; Quintana, J.M.; Avedillo, M.J. VLSI implementations of threshold logic-a comprehensive survey. *IEEE Trans. Neural Netw.* **2003**, *14*, 1217–43.

244. Midya, R.; Wang, Z.; Zhang, J.; Savel'ev, S.E.; Li, C.; Rao, M.; Jang, M.H.; Joshi, S.; Jiang, H.; Lin, P.; et al. Anatomy of Ag/Hafnia-Based Selectors with 1010Nonlinearity. *Adv. Mater.* **2017**, *29*, 1–8.

245. Fortunato, E.; Barquinha, P.; Martins, R. Oxide semiconductor thin-film transistors: A review of recent advances. *Adv. Mater.* **2012**, *24*, 2945–2986.

246. Owen, J.S.; Park, J.; Trudeau, P.E.; Alivisatos, A.P. Reaction chemistry and ligand exchange at cadmium-selenide nanocrystal surfaces. *J. Am. Chem. Soc.* **2008**, *130*, 12279–12281.

247. Rechberger, F.; Heiligtag, F.J.; Süess, M.J.; Niederberger, M. Assembly of BaTiO3nanocrystals into macroscopic aerogel monoliths with high surface area. *Angew. Chemie - Int. Ed.* **2014**, *53*, 6823–6826.

248. Wei, H.; Insin, N.; Lee, J.; Han, H.S.; Cordero, J.M.; Liu, W.; Bawendi, M.G. Compact zwitterion-coated iron oxide nanoparticles for biological applications. *Nano Lett.* **2012**, *12*, 22–25.

249. Pujari, S.P.; Scheres, L.; Marcelis, A.T.M.; Zuilhof, H. Covalent surface modification of oxide surfaces. *Angew. Chemie - Int. Ed.* **2014**, *53*, 6322–6356.

250. De Roo, J.; Van Den Broeck, F.; De Keukeleere, K.; Martins, J.C.; Van Driessche, I.; Hens, Z. Unravelling the surface chemistry of metal oxide nanocrystals, the role of acids and bases. *J. Am. Chem. Soc.* **2014**, *136*, 9650–9657.

251. Nonnenmann, S.S.; Gallo, E.M.; Spanier, J.E. Redox-based resistive switching in ferroelectric perovskite nanotubes. *Appl. Phys. Lett.* **2010**, *97*, 1–3.

252. Dongale, T.D.; Shinde, S.S.; Kamat, R.K.; Rajpure, K.Y. Nanostructured TiO2 thin film memristor using hydrothermal process. *J. Alloys Compd.* **2014**, *593*, 267–

270.

253. Gilson, M.K.; Given, J.A.; Bush, B.L.; McCammon, J.A. The statistical-thermodynamic basis for computation of binding affinities: A critical review. *Biophys. J.* **1997**, *72*, 1047–1069.

254. Lin, M.H.; Wu, M.C.; Huang, C.Y.; Lin, C.H.; Tseng, T.Y. High-speed and localized resistive switching characteristics of double-layer SrZrO3 memory devices. *J. Phys. D. Appl. Phys.* **2010**, *43*.

255. Guo, Z.; Zhu, L.; Zhou, J.; Sun, Z. Design principles of tuning oxygen vacancy diffusion in SrZrO3 for resistance random access memory. *J. Mater. Chem. C* **2015**, *3*, 4081–4085.

256. Beck, A.; Bednorz, J.G.; Gerber, C.; Rossel, C.; Widmer, D. Reproducible switching effect in thin oxide films for memory applications. *Appl. Phys. Lett.* **2000**, *77*, 139–141.

257. Jo, Y.; Jung, K.; Kim, J.; Woo, H.; Han, J.; Kim, H.; Hong, J.; Lee, J.K.; Im, H. Resistance switching mode transformation in SrRuO 3 /Cr-doped SrZrO 3 /Pt frameworks via a thermally activated Ti out-diffusion process. *Sci. Rep.* **2014**, *4*, 1–7.

258. Kumar, H.P.; Vijayakumar, C.; George, C.N.; Solomon, S.; Jose, R.; Thomas, J.K.; Koshy, J. Characterization and sintering of BaZrO3 nanoparticles synthesized through a single-step combustion process. *J. Alloys Compd.* **2008**, *458*, 528–531.

259. Hasegawa, S.; Sugimoto, T.; Hashimoto, T. Investigation of structural phase transition behavior of SrZrO3 by thermal analyses and high-temperature X-ray diffraction. *Solid State Ionics* **2010**, *181*, 1091–1097.

260. Lanza, M.; Reguant, M.; Zou, G.; Lv, P.; Li, H.; Chin, R.; Liang, H.; Yu, D.; Zhang, Y.; Liu, Z.; et al. High-Performance Piezoelectric Nanogenerators Using Two-Dimensional Flexible Top Electrodes. *Adv. Mater. Interfaces* **2014**, *1*, 1–7.

261. Yang, Y.C.; Pan, F.; Zeng, F. Bipolar resistance switching in high-performance Cu/ZnO : MMn/Pt nonvolatile memories: Active region and influence of Joule heating. *New J. Phys.* **2010**, *12*.

262. Hailstone, R.K.; DiFrancesco, A.G.; Leong, J.G.; Allston, T.D.; Reed, K.J. A study of lattice expansion in CeO2 Nanoparticles by Transmission Electron Microscopy. *J. Phys. Chem. C* **2009**, *113*, 15155–15159.

263. Ishikawa, K.; Uemori, T. Surface relaxation in ferroelectric perovskites. *Phys. Rev. B - Condens. Matter Mater. Phys.* **1999**, *60*, 11841–11845.

264. Jiang, B.; Peng, J.L.; Bursill, L.A. Surface structures and dielectric response of ultrafine BaTiO 3 particles. *Ferroelectrics* **1998**, *207*, 445–463.

265. Cisneros-Morales, M.C.; Aita, C.R. The effect of nanocrystallite size in monoclinic HfO2 films on lattice expansion and near-edge optical absorption. *Appl. Phys. Lett.* **2010**, *96*, 2008–2011.

266. Yoko, A.; Wang, J.; Umezawa, N.; Ohno, T.; Oshima, Y. A-Site Cation Bulk and Surface Diffusion in A-Site-Deficient BaZrO3 and SrZrO3 Perovskites. *J. Phys. Chem. C* **2017**, *121*, 12220–12229.

267. McCauley, D.; Newnham, R.E.; Randall, C.A. Intrinsic Size Effects in a Barium Titanate Glass-Ceramic. *J. Am. Ceram. Soc.* **2005**, *81*, 979–987.

268. Nian, Y.B.; Strozier, J.; Wu, N.J.; Chen, X.; Ignatiev, A. Evidence for an oxygen diffusion model for the electric pulse induced resistance change effect in

transition-metal oxides. *Phys. Rev. Lett.* **2007**, *98*, 3–6.

269. Choudhury, B.; Choudhury, A. Oxygen defect dependent variation of band gap, Urbach energy and luminescence property of anatase, anatase-rutile mixed phase and of rutile phases of TiO2 nanoparticles. *Phys. E Low-Dimensional Syst. Nanostructures* **2014**, *56*, 364–371.

270. Harrigan, W.L.; Michaud, S.E.; Lehuta, K.A.; Kittilstved, K.R. Tunable Electronic Structure and Surface Defects in Chromium-Doped Colloidal SrTiO3-δNanocrystals. *Chem. Mater.* **2016**, *28*, 430–433.

271. He, S.; Hao, A.; Qin, N.; Bao, D. Narrowing the band gap to enhance the resistive switching properties of Pr3+-doped ZnO thin films by Cd-ion doping. *RSC Adv.* **2017**, *7*, 38757–38764.

272. Rowtu, S.; Sangani, L.D.V.; Krishna, M.G. The Role of Work Function and Band Gap in Resistive Switching Behaviour of ZnTe Thin Films. *J. Electron. Mater.* **2018**, *47*, 1620–1629.

273. Desmond, K.W.; Weeks, E.R. Influence of particle size distribution on random close packing of spheres. *Phys. Rev. E - Stat. Nonlinear, Soft Matter Phys.* **2014**, *90*, 1–6.

274. Yamada, S.; Kanno, J.; Miyauchi, M. Multi-sized Sphere Packing in Containers: Optimization Formula for Obtaining the Highest Density with Two Different Sized Spheres. *IPSJ Online Trans.* **2011**, *4*, 126–133.

275. Mulvaney, P.; Lees, E.E.; Nice, E.C.; Nguyen, T.-L.; Clayton, A.H.A.; Rothacker, J.; Gunzburg, M.J.; Howlett, G.J. Experimental Determination of Quantum Dot Size Distributions, Ligand Packing Densities, and Bioconjugation Using

Analytical Ultracentrifugation. *Nano Lett.* **2008**, *8*, 2883–2890.

276. PAN, F.; CHEN, C.; WANG, Z.; YANG, Y.; YANG, J.; ZENG, F. Nonvolatile resistive switching memories-characteristics, mechanisms and challenges. *Prog. Nat. Sci. Mater. Int.* **2012**, *20*, 1–15.

277. Yoko, A.; Akizuki, M.; Oshima, Y. Formation mechanism of barium zirconate nanoparticles under supercritical hydrothermal synthesis. *J. Nanoparticle Res.* **2014**, *16*, 1–9.

278. Peña, M.A.; Fierro, J.L.G. Chemical structures and performance of perovskite oxides. *Chem. Rev.* **2001**, *101*, 1981–2017.

279. Terki, R.; Feraoun, H.; Bertrand, G.; Aourag, H. Full potential calculation of structural, elastic and electronic properties of BaZrO3 and SrZrO3. *Phys. Status Solidi Basic Res.* **2005**, *242*, 1054–1062.

280. Luo, Y.R. *Comprehensive handbook of chemical bond energies*; CRC Press, 2007; ISBN 9781420007282.

281. Yang, F.; Zhang, H.; Li, L.; Reaney, I.M.; Sinclair, D.C. High Ionic Conductivity with Low Degradation in A-Site Strontium-Doped Nonstoichiometric Sodium Bismuth Titanate Perovskite. *Chem. Mater.* **2016**, *28*, 5269–5273.

282. Garcia, R.; Martinez, R. V.; Martinez, J. Nano-chemistry and scanning probe nanolithographies. *Chem. Soc. Rev.* **2006**, *35*, 29–38.

283. Miller, K. atomic force metrology applications for alternating aperture phase-shift masks; Todd, B. Automated atomic force metrology applications for alternating aperture phase-shift masks. *20th Annu. BACUS Symp. Photomask Technol.* **2001**, *4186*, 681.

284. Zandiatashbar, A.; Kim, B.; Yoo, Y.; Lee, K.; Jo, A.; Lee, J.S.; Cho, S.-J.; Park, S. High-throughput automatic defect review for 300mm blank wafers with atomic force microscope. *Metrol. Insp. Process Control Microlithogr. XXIX* **2015**, *9424*, 94241X.

285. D'Costa, N.P.; Hoh, J.H. Calibration of optical lever sensitivity for atomic force microscopy. *Rev. Sci. Instrum.* **1995**, *66*, 5096–5097.

286. Labuda, A.; Cleveland, J.; Geisse, N.; Kocun, M.; Ohler, B.; Proksch, R.; Viani, M.; Walters, D. Photothermal excitation for improved cantilever drive performance in tapping mode atomic force microscopy. *Microsc. Anal.* **2014**, *28*, 23–27.

287. Labuda, A.; Hohlbauch, S.; Kocun, M.; Limpoco, F.T.; Kirchhofer, N.; Ohler, B.; Hurley, D. Tapping Mode AFM Imaging in Liquids with blueDrive Photothermal Excitation. *Micros. Today* **2018**, *26*, 12–17.

288. Robatjazi, H.; Bahauddin, S.M.; Macfarlan, L.H.; Fu, S.; Thomann, I. Ultrathin AAO Membrane as a Generic Template for Sub-100 nm Nanostructure Fabrication. *Chem. Mater.* **2016**, *28*, 4546–4553.